1984

An analytical and numerical analysis of the radiation from a slotted conducting cylinder with axial columns

Ahmad Ghaffarian Toosy Sany
Iowa State University

INFORMATION TO USERS

This reproduction was made from a copy of a document sent to us for microfilming. While the most advanced technology has been used to photograph and reproduce this document, the quality of the reproduction is heavily dependent upon the quality of the material submitted.

The following explanation of techniques is provided to help clarify markings or notations which may appear on this reproduction.

1. The sign or "target" for pages apparently lacking from the document photographed is "Missing Page(s)". If it was possible to obtain the missing page(s) or section, they are spliced into the film along with adjacent pages. This may have necessitated cutting through an image and duplicating adjacent pages to assure complete continuity.

2. When an image on the film is obliterated with a round black mark, it is an indication of either blurred copy because of movement during exposure, duplicate copy, or copyrighted materials that should not have been filmed. For blurred pages, a good image of the page can be found in the adjacent frame. If copyrighted materials were deleted, a target note will appear listing the pages in the adjacent frame.

3. When a map, drawing or chart, etc., is part of the material being photographed, a definite method of "sectioning" the material has been followed. It is customary to begin filming at the upper left hand corner of a large sheet and to continue from left to right in equal sections with small overlaps. If necessary, sectioning is continued again—beginning below the first row and continuing on until complete.

4. For illustrations that cannot be satisfactorily reproduced by xerographic means, photographic prints can be purchased at additional cost and inserted into your xerographic copy. These prints are available upon request from the Dissertations Customer Services Department.

5. Some pages in any document may have indistinct print. In all cases the best available copy has been filmed.

University Microfilms International
300 N. Zeeb Road
Ann Arbor, MI 48106

Ghaffarian Toosy Sany, Ahmad

AN ANALYTICAL AND NUMERICAL ANALYSIS OF THE RADIATION FROM A SLOTTED CONDUCTING CYLINDER WITH AXIAL COLUMNS

Iowa State University PH.D. 1984

An analytical and numerical analysis of the radiation from a slotted conducting cylinder with axial columns

by

Ahmad Ghaffarian Toosy Sany

A Dissertation Submitted to the
Graduate Faculty in Partial Fulfillment of the
Requirements for the Degree of

DOCTOR OF PHILOSOPHY

Department: Electrical Engineering and Computer Engineering
Major: Electrical Engineering (Electromagnetics)

Approved:

Signature was redacted for privacy.

In Charge of Major Work

Signature was redacted for privacy.

For the Major Department

Signature was redacted for privacy.

For the Graduate College

Iowa State University
Ames, Iowa
1984

TABLE OF CONTENTS

I. INTRODUCTION

A. The Problem and the Scope of the Study

An array of microstrip antenna panels was designed in 1978 for use on a 500-pound satellite which is called a "Plasma Diagnostics Package" (PDP). The satellite, designed by the department of Physics and Astronomy at the University of Iowa, is used to determine the interaction between the space shuttle and its environment 250 miles above the earth. Radio telemetry from the PDP to the shuttle vehicle utilizes a narrow band (0.2 MHz) UHF link at 400.6 MHz. The antenna design work was subcontracted to Iowa State University. An eight element surface-mounted array composed of quarter-wavelength microstrip antenna panels was chosen. The design was done experimentally (21) and it met the design specifications. Workable positions of the microstrip antennas on the surface of the PDP were determined experimentally as well.

Fig. 1-1 shows the geometry of the PDP. Two antenna elements are mounted between each pair of support columns. These columns are 90° apart, they have square cross-sectional areas of $5.08cm^2$, and they serve as mounting points for the fiberglass booms. The 1.75 m booms hold probes and contain electrical cables. The radiation patterns were found to be quite sensitive to the position of the antenna elements with respect to the columns. We desired to find a way to analyze this effect. The purpose of this study is not only to determine the effect of these obstacles on the radiation patterns of the conducting cylinder with

the microstrip antennas, but also to study the sensitivity of the pattern to the circumferential spacing between the antenna panels and the obstacles.

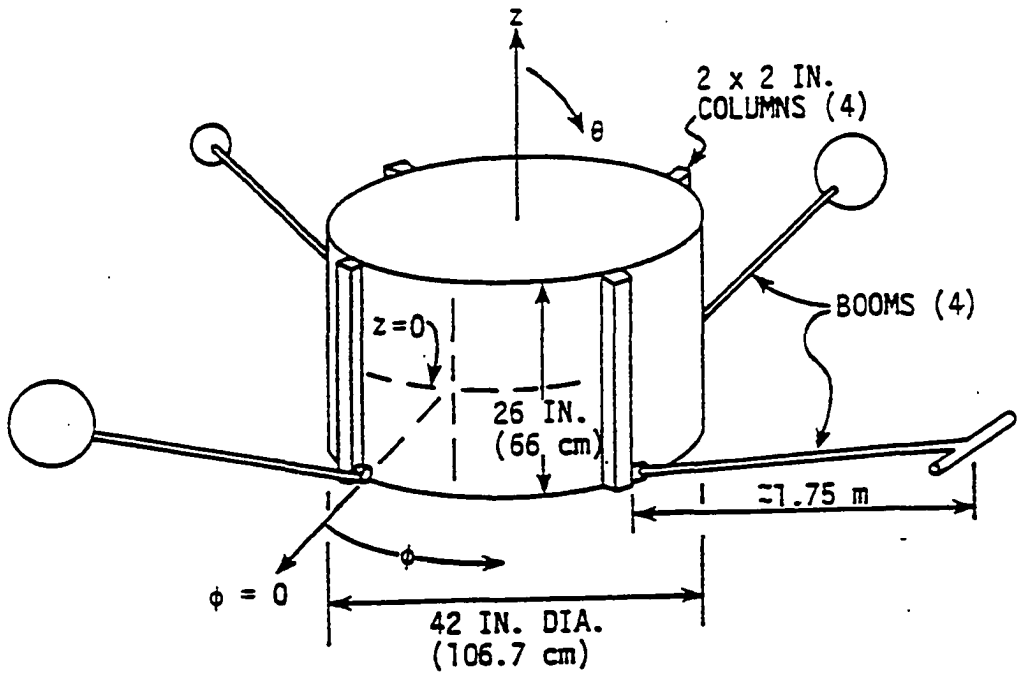

Fig. 1-1. The instrumented space probe satellite (PDP)

B. Survey of Relevant Literature

Microstrip antennas were considered as one of the main subjects for literature study. Special consideration was given to aperture antennas on the surface of a conducting cylinder (2, 3, 8, 19, 20, 22). Radiation

fields from a smooth slotted cylinder were also given special attention (10).

Moment methods have recently emerged as one of the most important tools for the numerical evaluation of integral equations and boundary value problems in electromagnetic fields. This method has been studied extensively by Harrington (9). In connection with this method, wire-grid modeling and surface patch modeling were reviewed and investigated for their applicablility to the present project (17, 24).

The Geometrical Theory of Diffraction (GTD) (1, 3, 11, 15), the Uniform Theory of Diffraction (UTD) (17, 20), and the Hybrid Technique (5, 7, 27) have been studied and evaluated for this project. The hybrid technique was found to be the only other possible method which could be used to investigate this problem.

C. Scope of the Present Work

A numerical analysis method based on the method of moments has been developed at the Lawrence Livermore Laboratory with the name of "Numerical Electromagnetic Code (NEC)-Method of Moments" (4). This program is built around the numerical solution of integral equations for currents induced on the structure by sources or incident fields. The excitation may be either voltage sources on the structure or an incident plane wave of linear or elliptical polarization. A copy of this program was received from Lawrence Livermore Labs. Several problems were encountered in using the program. First, it had to be translated from a

CDC machine format to an IBM computer format. Next, the original NEC program was modified to accept an aperture antenna as an excitation.

The last problem was insurmountable: namely, this program only handles objects which are smaller than a wavelength. When implementing either the wire-grid or surface-patch models the user must limit the dimensions relative to the operating wavelength. Modifying the program to handle larger objects requiring a greater number of modeling segments or patches led to large matrices in the program; the resulting program became too expensive to run.

As a result, attention was shifted to developing an analytical approach to the problem of aperture radiators on a cylinder, for comparison with the NEC results and the experimental results, and to include the effect of the obstacles. The initial analysis was done for a slot in a large flat conducting plane with an obstacle close to the slot. The obstacle, which simulates one of the columns, is an infinitely long low fence perpendicular to the ground plane. The far-field with and without the obstacle was analyzed, in order to develop an order-of-magnitude feeling for the effect of the fence in a simplified geometry. The resulting predicted effect of the fence was much less than that suggested by the earlier pattern measurements on the cylindrical PDP model with columns (21).

We saw that the analytical approach must therefore deal with a microstrip antenna mounted on the surface of a conducting cylinder with columns on it. A computer program was developed to obtain the radiation pattern of a slotted cylinder antenna without columns (10, 25, 26). To

simulate the entire pattern with columns present, an analytical expression and a program were developed to find the near-fields at the cylinder surface, so that their interaction with columns could be determined (6, 10, 21).

A new series of radiation pattern measurements was then made to verify the analytical results.

Finally, the problem was modeled by the NEC program. In order to do this, it was necessary to sacrifice some accuracy in order to model the PDP, with columns, within the allowable matrix sizes.

II. MODIFICATION OF NEC AND ITS APPLICATION

A. Method of Moments

The PDP with its microstrip antennas can be considered as a closed conducting body except over the antenna apertures. The tangential components of the E-field are then zero everywhere but over the aperture. Knowing the tangential components of either the H-field or the E-field is sufficient to determine the external fields by using the method of moments.

Let S be a closed surface consisting of both the conductor and aperture, and $\bar{J}_s$ be the distribution of surface current on S. To find $\bar{J}_s$ for a wide variety of practical radiating and scattering objects, the method of moments has become a widely-used numerical technique (9). A knowledge of $\bar{J}_s$, in turn, permits us to compute radiation patterns, scattering cross-section, impedance, etc.

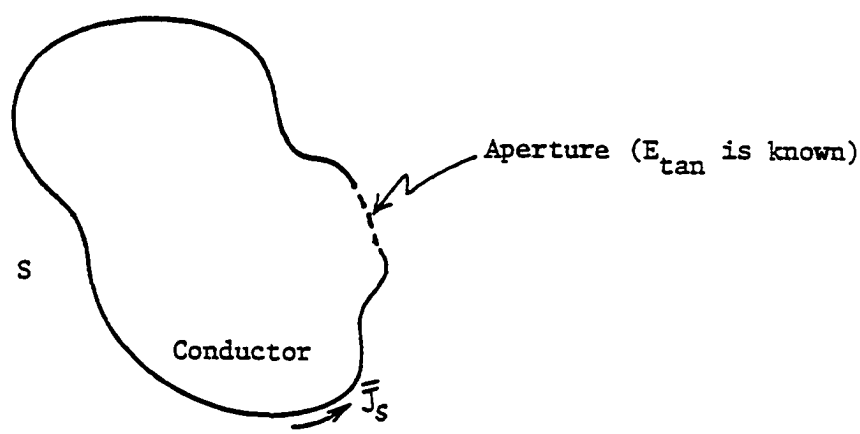

Fig. 2-1. A closed surface conducting body with aperture on it

$$\text{Let} \quad L(J_s) = -E_{tan} = E_s \tag{2-1}$$

where L is the operator (for this problem it is an integral operator)

E_{tan} = the known incident field on S.

E_s = the scattered field, and

J_s = unknown function.

These are all understood to be vector quantities. To solve equation (2-1) for J, the following steps should be done.

$$J_s = \sum_n I_n J_n, \tag{2-2}$$

where I_n are complex coefficients, and J_n are basis functions. Substituting (2-2) into (2-1) and using the linearity of L we get

$$\sum_n I_n L(J_n) = -E_{tan}. \tag{2-3}$$

To use the method of moments, the conducting surface is subdivided into m patches, with a testing function W_i associated with each patch. Given this set of testing functions W_1, W_2, W_3, W_4, $\cdots$ W_m, which are tangential vectors on the surface, the method of moments requires that (2-3) be valid for the inner product with each W_m, as shown below.

$$\sum_n I_n \langle W_m, L(J_n) \rangle = \langle W_m, -E_{tan} \rangle , \tag{2-4}$$

$$\text{Let } V_m = - \langle W_m, E_{tax} \rangle = - \iint_{\text{aperture}} E \cdot W_m \, ds' , \tag{2-5}$$

or

$$[V_m] = - \begin{bmatrix} \langle W_1, E_{tan} \rangle \\ \langle W_2, E_{tax} \rangle \\ \langle W_3, E_{tan} \rangle \\ \vdots \\ \langle W_m, E_{tan} \rangle \end{bmatrix} , \tag{2-6}$$

and

$$[I_n] = \begin{bmatrix} I_1 \\ I_2 \\ I_3 \\ I_4 \\ \vdots \\ I_n \end{bmatrix} . \tag{2-7}$$

Then using the relation,

$$[Z_{mn}]\ [I_n] = [V_m], \tag{2-8}$$

the impedance matrix is:

$$[Z_{mn}] = \begin{bmatrix} \langle W_1, LJ_1\rangle & \langle W_1, LJ_2\rangle & \cdots\cdots & \cdots & \langle W_1, LJ_n\rangle \\ \langle W_2, LJ_1\rangle & \langle W_2, LJ_2\rangle & \cdots\cdots & \cdots & \langle W_2, LJ_n\rangle \\ \vdots & \vdots & \vdots & \vdots & \vdots \\ \langle W_m, LJ_1\rangle & \langle W_m, LJ_2\rangle & \cdots\cdots & \cdots & \langle W_m, LJ_n\rangle \end{bmatrix} \tag{2-9}$$

If the matrix $[Z_{mn}]$ is nonsingular, its inverse $[Z_{mn}]^{-1}$ exists. The, excitation matrix $[V_m]$ may be calculated from the following equation (4):

$$V_m = -\bar{i} \cdot [(\bar{E}_m)] \qquad (2\text{-}10)$$

where V_m = the excitation matrix

$\bar{i}$ = the orientation of segment i

$\bar{E}_m$ = the total complex E-field at segment/patch m,

which are known.

Therefore, the I_n are then given by,

$$[I_n] = [Z_{mn}]^{-1} [V_m] \qquad (2\text{-}11)$$

Finally, knowing I_n, $\bar{J}$ will be given by equation (2-2). Thus the integral equation for $\bar{J}$ in equation (2-1) has been solved.

B. The Development of Formulas

The Numerical Electromagnetic Code (NEC) is a user-oriented computer code using the method of moments for analysis of the electromagnetic

response of antennas. It is built around the numerical solution of integral equations for the currents induced on the structure, by voltage sources on the structure, or for an incident plane wave of linear or elliptical polarization. This computer code, however, could not accept an aperture antenna on the structure as an exciter. Therefore, the program needed to be modified so that the excitation matrix could represent an aperture antenna. A subroutine was developed and incorporated in the NEC program to make it usable for aperture antennas so that it could be used for this study.

The microstrip antenna on the conducting surface can be modeled as a slot on the surface, Fig. 2-2.

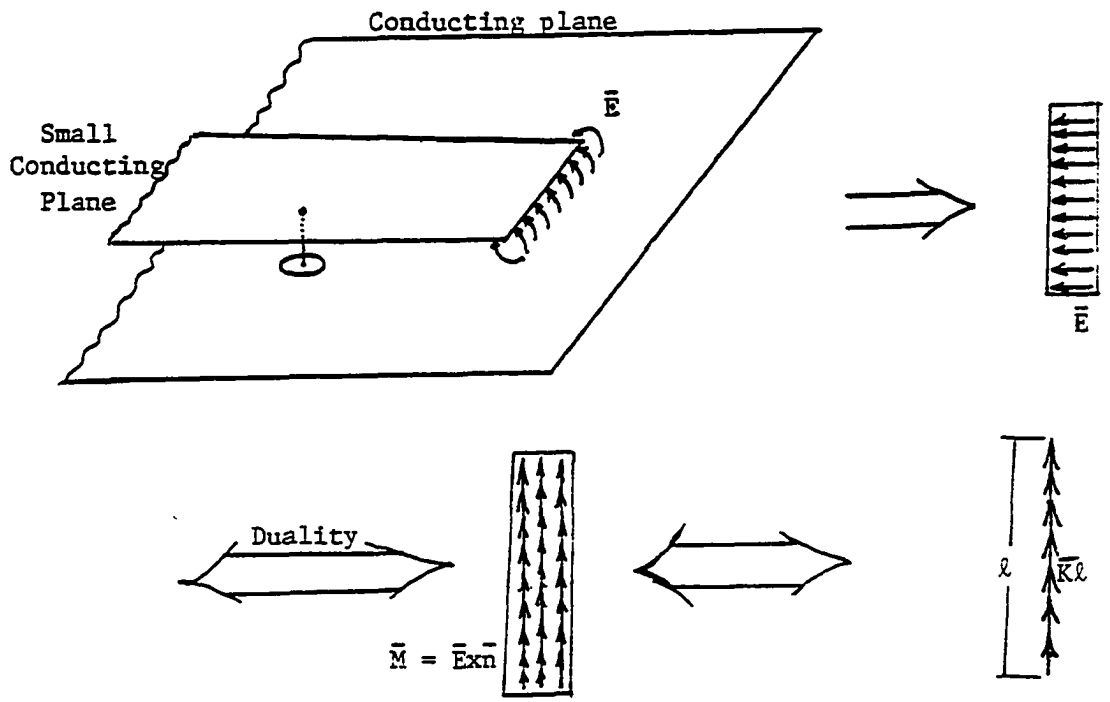

Fig. 2-2. Transformation of aperture antenna to Magnetic Current Source

where $\bar{E}$ = electric field across the slot

$\bar{M}$ = magnetic current density over the slot

$\bar{n}$ = unit vector normal outward from the cylinder

If slot is narrow and short then, $\bar{M}$ can be treated as a magnetic current element. To develop an appropriate formula, duality can be applied to the electric current element equations (10).

Assume $\overline{I\ell}$ is a z-directed electric current element at the coordinate origin in Fig. 2-3. The field expressions due to this current element are:

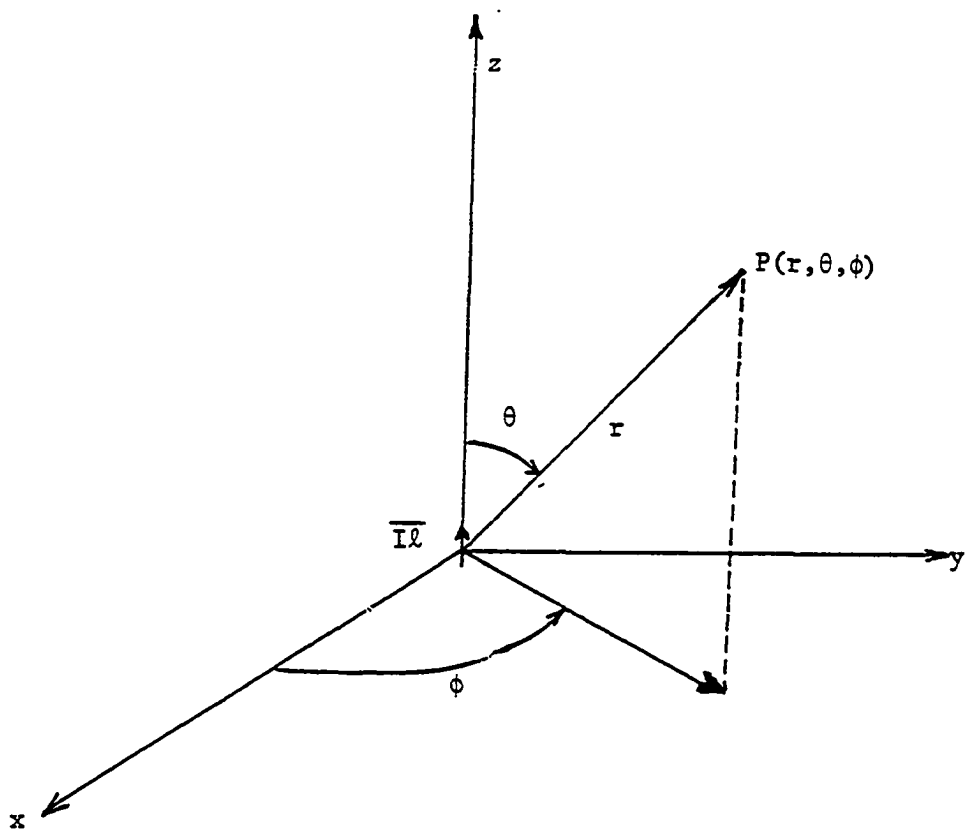

Fig. 2-3. Z-directed current element at the coordinate origin

$$E_r = \frac{I\ell}{2\pi} e^{-jkr} \left(\frac{\eta}{r^2} + \frac{1}{j\omega\varepsilon r^3}\right) \cos\theta, \qquad (2\text{-}12)$$

$$E_\theta = \frac{I\ell}{4\pi} e^{-jkr} \left(\frac{j\omega\mu}{r} + \frac{\eta}{r^2} + \frac{1}{j\omega\varepsilon r^3}\right) \sin\theta, \qquad (2\text{-}13)$$

$$H_\phi = \frac{I\ell}{4\pi} e^{-jkr} \left(\frac{jk}{r} + \frac{1}{r^2}\right) \sin\theta, \qquad (2\text{-}14)$$

where E_r, E_θ and H_ϕ are electric and magnetic fields in spherical coordinates, and where

k = wave number = $\frac{2\pi}{\lambda}$

λ = wave length

η = intrinsic impedance

ω = angular velocity = $2\pi f$

f = frequency

μ = permeability of the medium

ε = permittivity of the medium

Using the duality principle with the equations of (2-12)-(2-14), the fields radiated by the magnetic current element will be:

$$H_r = \frac{|K\ell|}{2\pi} e^{-jkr} \left(\frac{1}{\eta r^2} + \frac{1}{j\omega\mu r^3}\right) \cos\theta, \qquad (2\text{-}15)$$

$$H_\theta = \frac{|K\ell|}{4\pi} e^{-jkr}\left(\frac{j\omega\varepsilon}{r} + \frac{1}{\eta r^2} + \frac{1}{j\omega\mu r^3}\right) \mathrm{Sin}\theta, \qquad (2\text{-}16)$$

$$E_\phi = -\frac{|K\ell|}{4\pi} e^{-jkr}\left(\frac{jk}{r} + \frac{1}{r^2}\right) \mathrm{Sin}\theta, \qquad (2\text{-}17)$$

where $|K\ell|$ = magnitude of a z-directed magnetic current element (Fig. 2-2). For computer programming, it is more convenient to work in the cartesian coordinate system.

$$H_x = \frac{x|K\ell|}{2\pi D} e^{-jkD}\left(\frac{1}{\eta D^2} + \frac{1}{j\omega\mu D^3}\right) \mathrm{Cos}\theta + \frac{xz|K\ell|}{4\pi D\sqrt{x^2+y^2}} e^{-jkD}\left(\frac{j\omega\varepsilon}{D} + \frac{1}{\eta D^2} + \frac{1}{j\omega\mu D^3}\right) \mathrm{Sin}\theta \qquad (2\text{-}18)$$

$$H_y = \frac{y|K\ell|}{2\pi D} e^{-jkD}\left(\frac{1}{\eta D^2} + \frac{1}{j\omega\mu D^3}\right) \mathrm{Cos}\theta + \frac{yz|K\ell|}{4\pi D\sqrt{x^2+y^2}} e^{-jkD}\left(\frac{j\omega\varepsilon}{D} + \frac{1}{\eta D^2} + \frac{1}{j\omega\mu D^3}\right) \mathrm{Sin}\theta \qquad (2\text{-}19)$$

$$H_z = \frac{z|K\ell|}{2\pi D} e^{-jkD}\left(\frac{1}{\eta D^2} + \frac{1}{j\omega\mu D^3}\right) \mathrm{Cos}\theta - \frac{\sqrt{x^2+y^2}\,|K\ell|}{4\pi D} e^{-jkD}\left(\frac{j\omega\varepsilon}{D} + \frac{1}{\eta D^2} + \frac{1}{j\omega\mu D^3}\right) \mathrm{Sin}\theta \qquad (2\text{-}20)$$

and

$$E_x = \frac{y|K\ell|}{4\pi\sqrt{x^2+y^2}} e^{-jkD} \left(\frac{jk}{D} + \frac{1}{D^2}\right) \text{Sin}\theta \qquad (2\text{-}21)$$

$$E_y = -\frac{x|K\ell|}{4\pi\sqrt{x^2+y^2}} e^{-jkD} \left(\frac{jk}{D} + \frac{1}{D^2}\right) \text{Sin}\theta \qquad (2\text{-}22)$$

$$E_z = 0 \qquad (2\text{-}23)$$

where H_x, H_y, H_z, E_x, E_y, and E_z are magnetic and electric fields in the x, y, and z directions at the observation point (x, y, z).

$$D = \sqrt{x^2+y^2+z^2}, \quad \text{and} \quad \theta = \text{Cos}^{-1} \frac{z}{\sqrt{x^2+y^2+z^2}}$$

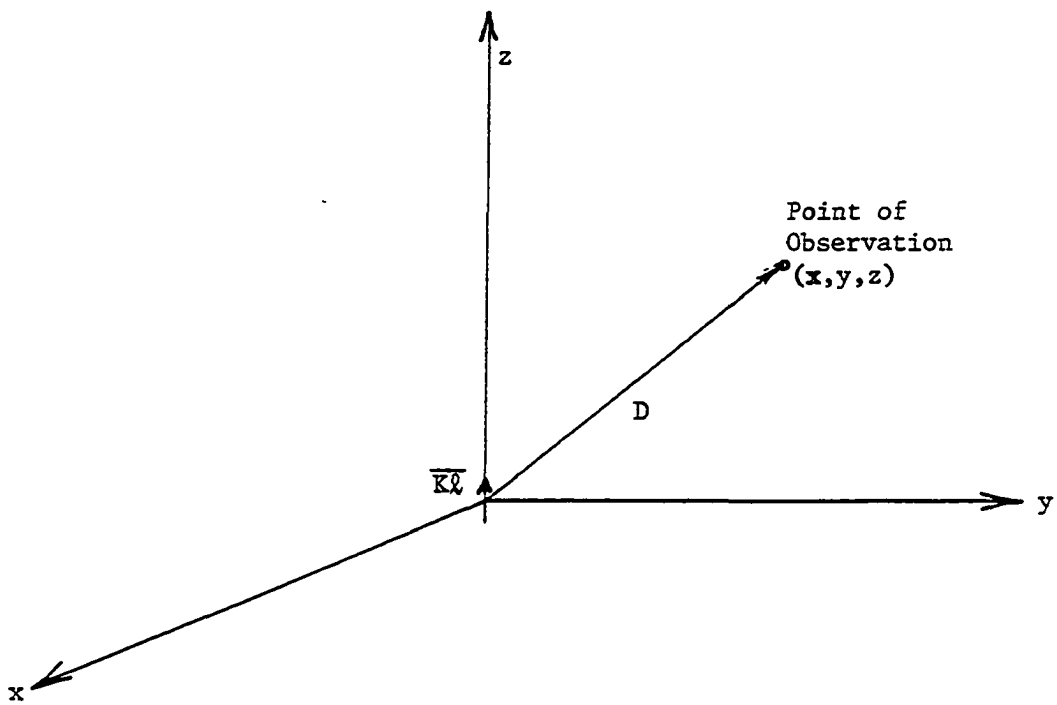

Fig. 2-4. A z-directed magnetic current element at coordinate origin

A computer program was written based on equations (2-18) through (2-23) which is able to calculate electric and magnetic fields at any point of observation (x, y, z). The program can also handle an extended source distribution (x', y', z') as shown in Fig. 2-5. Then by using superposition the fields at any point of observation will result.

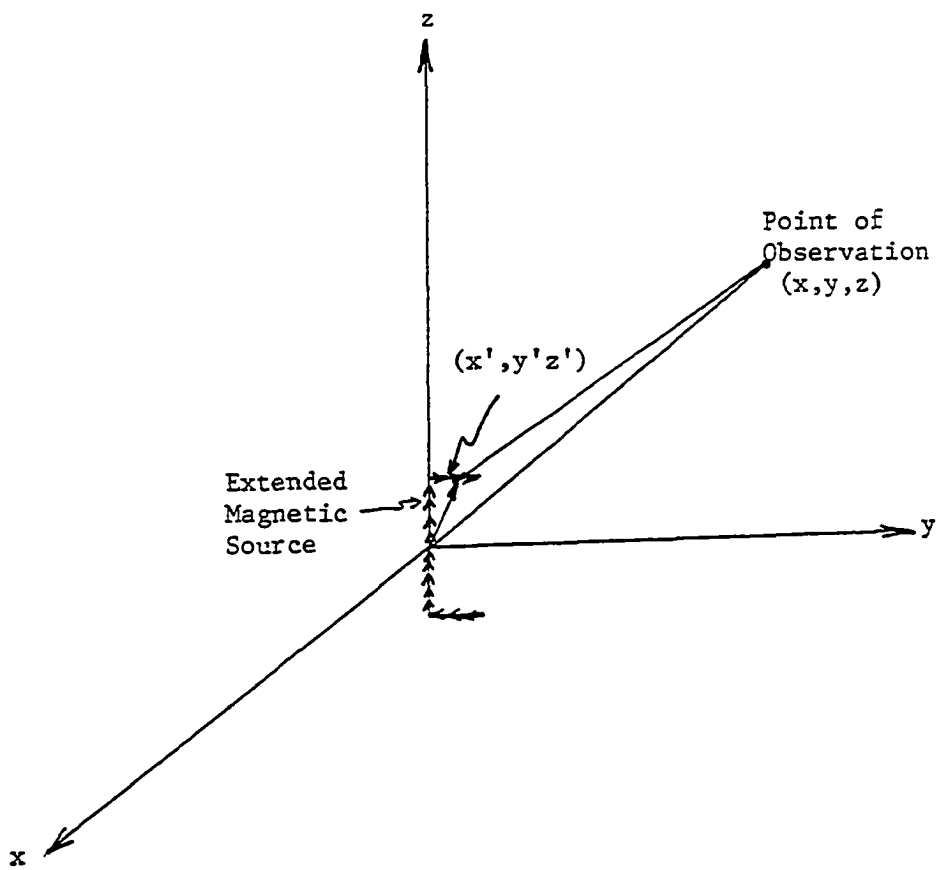

Fig. 2-5. An extended magnetic source (x', y', z')

When a distribution of the kind shown in Figure 2-5 is used to represent a quarter-wavelength the microstrip antenna panel, the magnitude of the magnetic current in the z direction is uniform, but the currents in the y-directed arms follow a cosine amplitude varying from maximum value at the corners to zero at the endpoints.

Knowing the electric and magnetic field at any arbitrary point due to the source, we can fill the excitation matrix and then apply the method of moments to solve for the surface current distribution on the object. This method requires that the surface be divided into many small segments or patches, each of which has an excitation current associated with it. When modeling large surfaces, this results in a large number of segments, and the computer program will be required to handle large matrices. Thus, the size of the object being modeled directly influences the cost of running the program, and it must be considered when doing this computer work.

Because the PDP requires a large number of patches or segments, the NEC program is tested to its limits, and to ensure accurate predictions, an analytical model was also developed for comparative purposes. Chapter IV contains the results of this comparison.

III. ANALYTICAL MODEL: A SIMPLIFIED APPROACH

The original experimental design and study of the PDP (21) showed that the radiation pattern of the PDP, with support columns (as is Figure 1-1) and with either one or eight microstrip antenna panels, was quite sensitive to the position of the panels relative to the columns. A major question which the present work was designed to answer was whether this effect was due to scattering from the columns in the presence of a standing wave set up around the cylinder by the antenna panel apertures, or whether it was caused by some other effect, e.g., near-field perturbation by the antenna panels themselves on the outside of the cylinder.

To study this effect with the numerical model of NEC would be very expensive, because of the large number of computer runs needed to characterize the object with parameters being varied over wide ranges. It would also be of questionable accuracy, because the size of the PDP is at the upper limit of what can be modeled accurately with the size of matrices allowed in the NEC program.

For these reasons, we desired to generate an analytical model to yield radiation patterns which could be used to corroborate those obtained from NEC. This model, to account for the effect of the columns, would have to use the near-fields over the cylindrical surface.

The procedure for calculating these near-fields is presented in the literature, and its application to the present study is presented in Chapter IV. But a cylindrical geometry is a difficult one in which to work with solutions of wave equations. Therefore, we desired to do an

initial analysis in a simpler geometry in order to try to develop a feeling for whether the scattering from the columns was being modeled satisfactorily. The geometry chosen for this analysis was a radiating aperture slot in an infinitely large, flat ground plane with a zero-thickness, low conducting "fence" near the slot. Fig. 3-1 illustrates this model, in which the scattering from the fence is to be superimposed on the radiation from the slot itself.

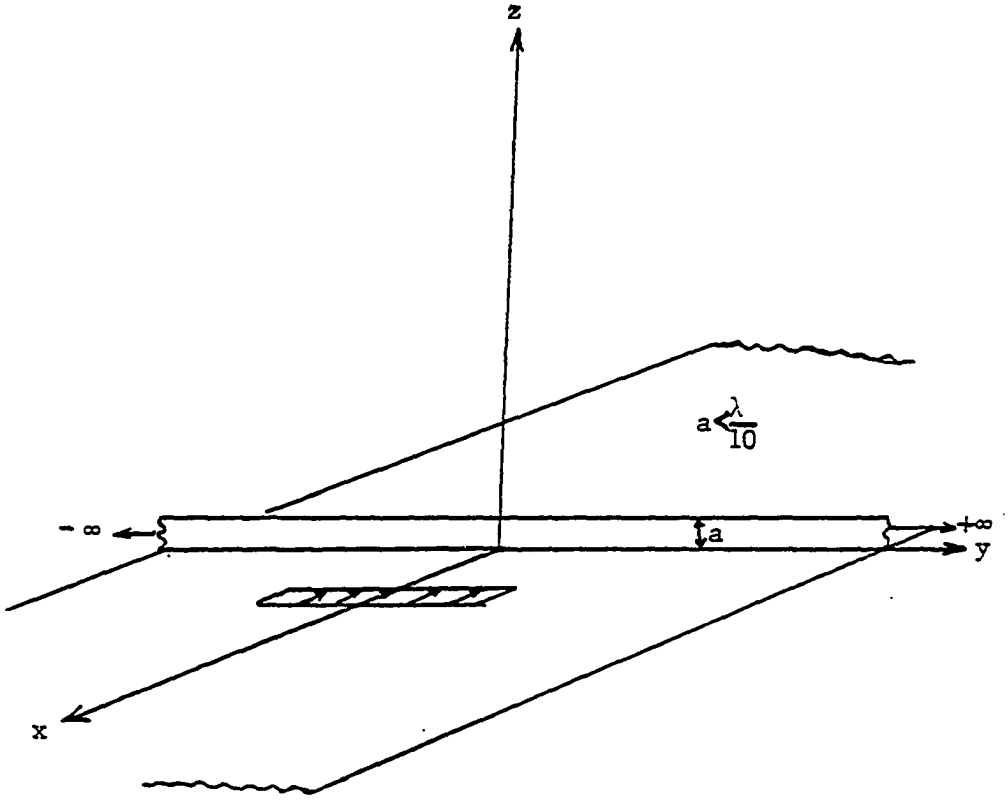

Fig. 3-1. A large flat conducting plane with a slot aperture and conducting fence

A. Radiation Due to the Slot Only

The duality theorem was used to get the pattern of the radiation of the slot on the flat conducting plane as shown below.

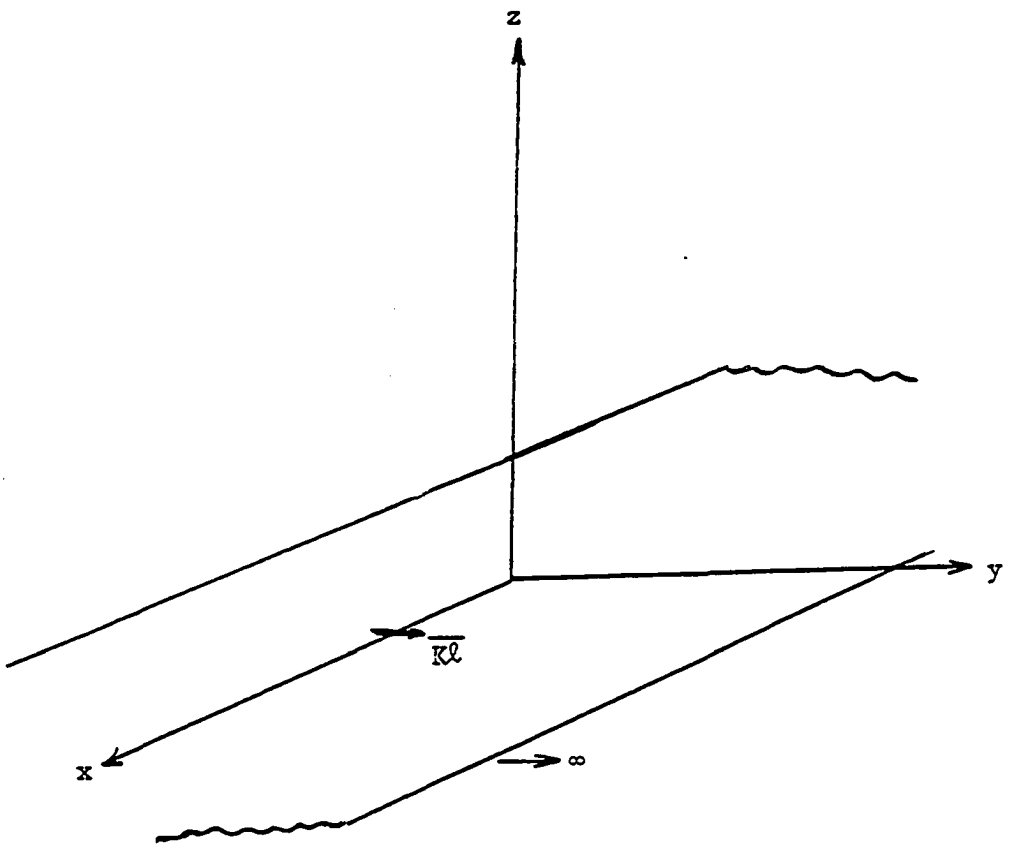

Fig. 3-2. A y-directed magnetic current element on the flat conducting plane

Equations (2-7) to (2-12) may be used to determine the fields at any point due to a z-directed magnetic current element. The same formulas can be modified for a slot oriented in the y-direction. This modification is done according to the Table 3-1.

Table 3-1. Conversion of E-field and coordinates from z-directed Magnetic current Element to a y-directed Magnetic Current Element

Old (z-directed) E-field	New (y-directed) E-field	Old (z-directed) coordinates	New (y-directed) coordinates
E_z	E_y	z	y
E_x	E_x	x	x
$-E_y$	E_z	-y	z

The modified formulas for a magnetic current element at the origin, as Fig. 3-3, are:

$$E_x = \frac{-z|K\ell|}{4\pi\sqrt{x^2+z^2}} e^{-jkD} \left(\frac{jk}{D} + \frac{1}{D^2}\right) \sin\alpha \qquad (3\text{-}1)$$

$$E_y = 0 \tag{3-2}$$

$$E_z = \frac{x1K\ell 1}{4\pi\sqrt{x^2+z^2}} e^{-jkD} \left(\frac{jk}{D} + \frac{1}{D^2}\right) \text{Sin}\alpha \tag{3-3}$$

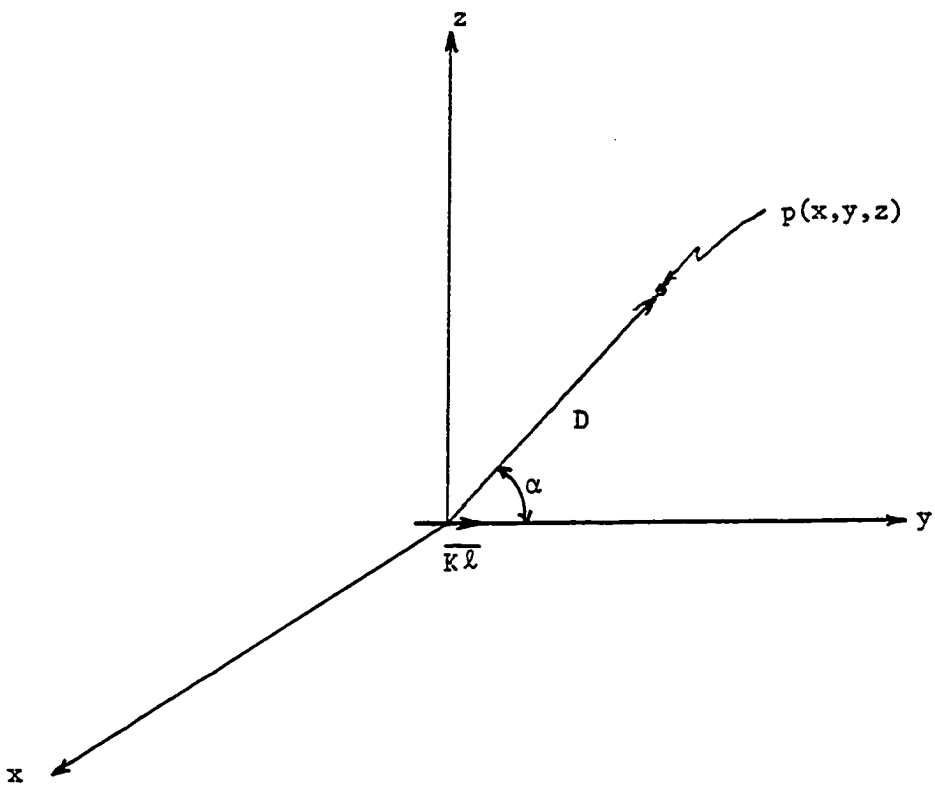

Fig. 3-3. A y-directed magnetic current element at the coordinate origin

and

$$H_x = \frac{x|K\ell|}{2\pi D} e^{-jkD} \left(\frac{1}{\eta D^2} + \frac{1}{j\omega\mu D^3}\right) \text{Cos}\alpha \; + \tag{3-4}$$

$$\frac{xy|K\ell|}{4\pi D\sqrt{x^2+y^2}} e^{-jkD} \left(\frac{j\omega\varepsilon}{D} + \frac{1}{\eta D^2} + \frac{1}{j\omega\mu D^3}\right) \text{Sin}\alpha$$

$$H_y = -\frac{y|K\ell|}{2\pi D} e^{-jkD} \left(\frac{1}{\eta D^2} + \frac{1}{j\omega\mu D^3}\right) \text{Cos}\alpha \; - \tag{3-5}$$

$$\frac{\sqrt{x^2+z^2}|K\ell|}{4\pi D} e^{-jkD} \left(\frac{j\omega\varepsilon}{D} + \frac{1}{\eta D^2} + \frac{1}{j\omega\alpha D^3}\right) \text{Sin}\alpha$$

$$H_z = \frac{z|K\ell|}{2\pi D} e^{-jkD} \left(\frac{1}{\eta D^2} + \frac{1}{j\omega\mu D^3}\right) \text{Cox}\alpha \; + \tag{3-6}$$

$$-\frac{zy|K\ell|}{4\pi D\sqrt{x^2+y^2}} e^{-jkD} \left(\frac{j\omega\varepsilon}{D} + \frac{1}{\eta D^2} + \frac{1}{j\omega\mu D^3}\right) \text{Sin}\alpha$$

Since it is easier to keep the fence at the origin, the magnetic source will be shifted along the x-axis a distance d from the origin, Fig. 3-4.

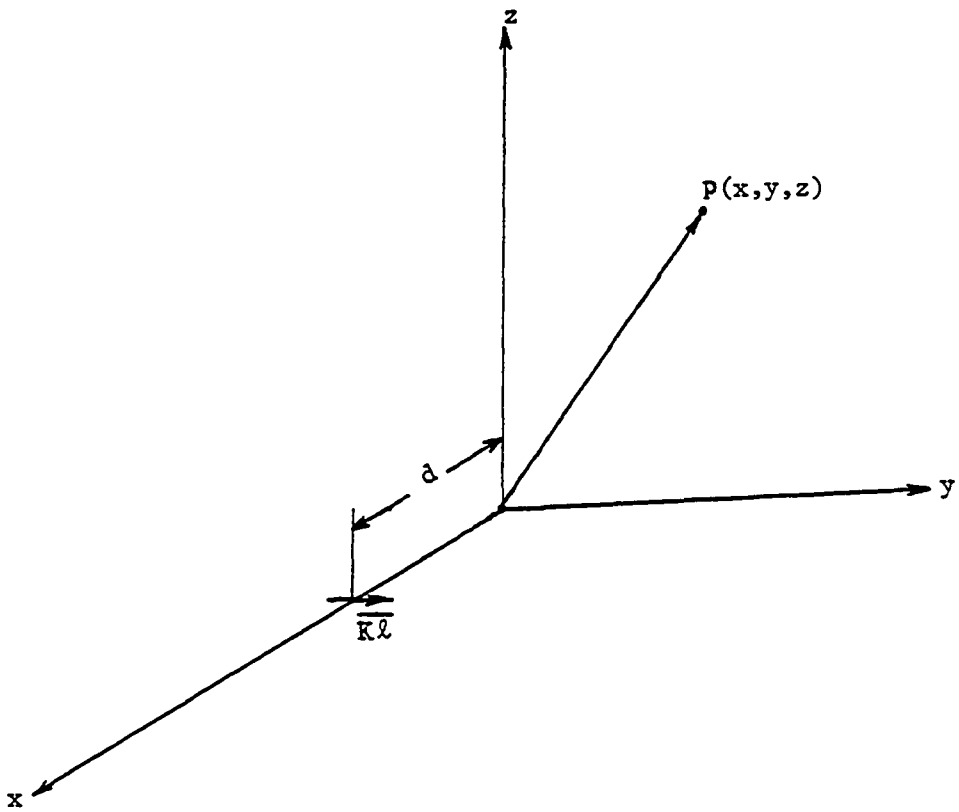

Fig. 3-4. A shifted y-directed magnetic current element

A computer program was developed based on the above expressions and superposition to calculate the E-field and H-field at any observation point due to a extended magnetic source.

B. Radiation Due to Currents on the Fence

Assuming no thickness for the fence, the fence could be represented as a continuous current distribution lying in a plane. Consider a sheet of electric current lying in the yz-plane and flowing in the z-direction (14) as shown in Fig. 3-5. The height of the fence is small compared to a wavelength ($a<\lambda/10$). And, since the fence current is induced by radiation from a slot or magnetic current element as in Fig. 3-1, the only important component of $\overline{J}$ is J_z .

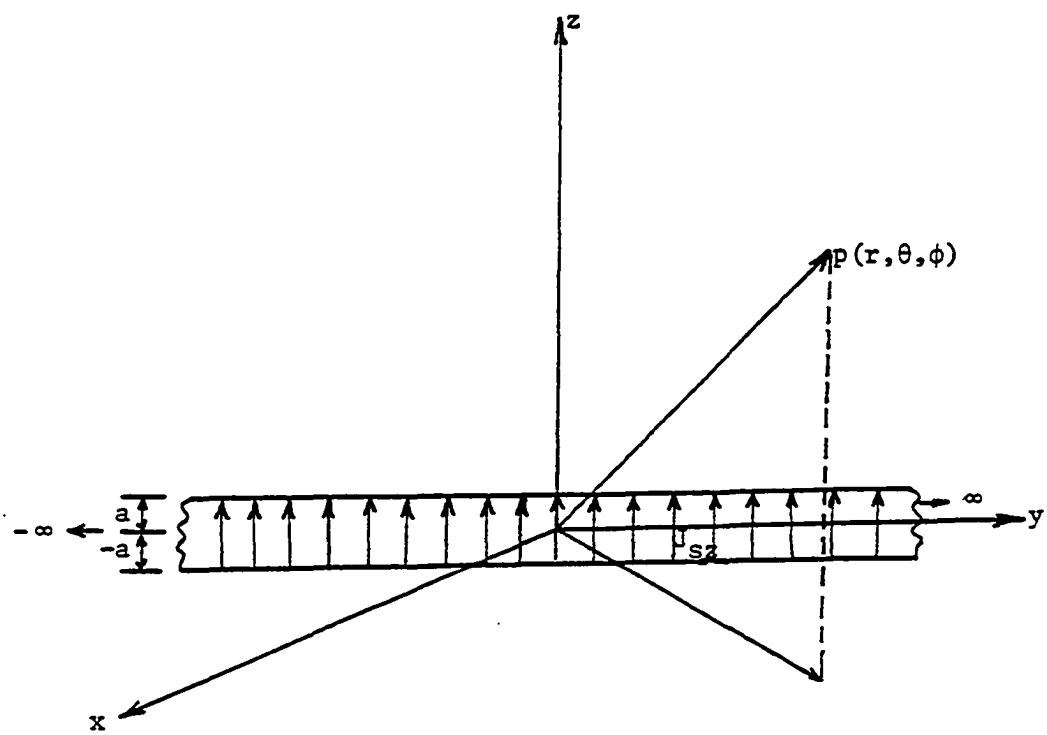

Fig. 3-5. Continuous distribution of electric current density J_{sz} lying in the yz-plane

The far-field expression is defined as:

$$E_{\theta f}(\theta) = \frac{-jk\eta e^{-jkr}}{4\pi r} f_{\theta}(\theta,\phi), \tag{3-7}$$

in which

$$f_{\theta}(\theta,\phi) = - \text{Sin}\theta \; f_{z}, \tag{3-8}$$

and

$$f_{z} = \int_{\text{all space}} J_{z}(r') \, e^{jk\bar{r}\cdot r'} dv', \tag{3-9}$$

where $\bar{r}$ is in spherical coordinates for the observation point, and the source point r' is in rectangular coordinates. The dot product in the volume integral is given by,

$$\begin{aligned} r' &= x' \, \bar{i}_x + y' \, \bar{i}_y + z' \, \bar{i}_z, \\ \bar{r} &= \text{Sin}\,\theta \, \text{Cos}\,\phi \, \bar{i}_x + \text{Sin}\,\phi \, \text{Sin}\,\theta \, \bar{i}_y + \text{Cos}\,\theta \, \bar{i}_z, \\ \bar{r}\cdot r' &= x' \, \text{Sin}\,\theta \, \text{Cos}\,\phi + y' \, \text{Sin}\,\theta \, \text{Sin}\,\phi + z' \, \text{Cos}\theta, \end{aligned} \tag{3-10}$$

For current lying in the yz-plane, x'=0 and ϕ=0. Equation (3-10) becomes:

$$\bar{r}\cdot r' = z' \text{ Cos } \theta \ , \qquad (3\text{-}11)$$

and equation (3-7) may be expressed as:

$$E_{\theta f}(\theta) = \frac{jkne^{-jkr}}{4\pi r} \text{Sin}\theta \int_{-\infty}^{\infty}\int_{-\infty}^{\infty} J_{sz}(y',z') \, e^{jk(z' \text{ Cos}\theta)} dy'dz'. \qquad (3\text{-}12)$$

The surface current density $J_{sz}(y',z')$ is assumed to be separable, i.e., it may be written in the form,

$$J_{sz}(y',z') = J_a(y') \, J_b(z') \qquad (3\text{-}13)$$

so that equation (3-12) becomes,

$$E_{\theta f}(\theta) = \frac{jkne^{-jkr}}{4\pi r} \text{Sin } \theta \int_{-\infty}^{\infty} J_a(y') \, dy' \int_{-\infty}^{\infty} J_b(z')e^{jkz' \text{ Cos}\theta} dz'. \qquad (3\text{-}14)$$

Since the height of the fence is much smaller than wavelength ($a<\frac{\lambda}{10}$), and it is located on a perfectly conducting plane, z' in equation (3-14) varies from -a to a (Image Theory in free-space). Let us define,

$$I(y') = \int_{-\infty}^{\infty} J_a(y') \, dy' \quad \text{and} \quad I(z') = \int_{-\infty}^{\infty} J_b(z')e^{jkz' \text{ Cos}\theta} \, dz',$$

Again because $a<\lambda/10$, $e^{jkz' \text{ Cos}\theta} \approx 1$ can be assumed.

Then I(z') becomes,

$$I(z') = \int_{-\infty}^{\infty} J_b(z') \, dz' \qquad (3\text{-}15)$$

The value of $J_b(z')$ is maximum at the intersection of the fence and conducting plane, and for a zero-thickness fence it would gradually go to zero at $z' = \pm a$ (see Fig. 3-6a). But since the fence is actually a simple model of a thick column, currents could flow into the outer faces of the columns and not go to zero; thus, in this case, $J_b(z')$ is assumed to be uniform with a value of unity for $z' = \pm a$ as in Fig. 3-6b.

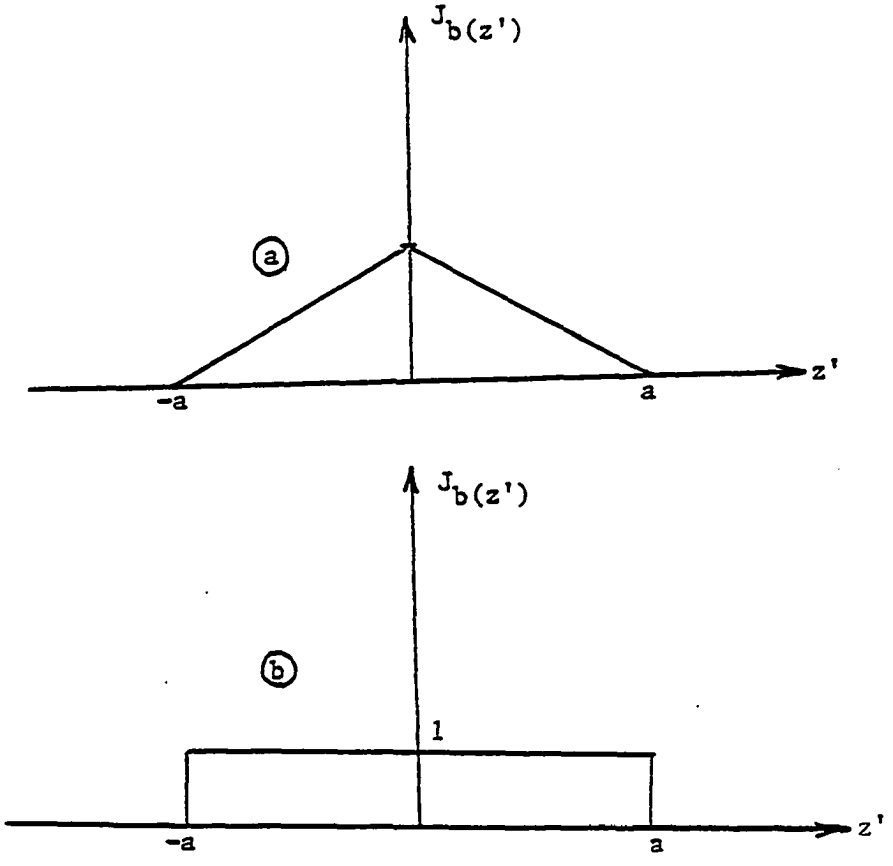

Fig. 3-6. a) Actual value of $J_b(z')$ on a thin fence,

Fig. 3-6. b) Assumed value of $J_b(z')$ on a "thick fence" representing a column

The value of $J_a(y')$ is primarily dependent upon $H_y(y')$. To determine the value of $J_a(y')$ in this simplified model we use the same approach as in the case of a plane wave incident upon a large conducting plane; namely, that tangential electric field at the conducting fence is zero and tangential magnetic field is doubled. Thus,

$$J_{sz}(y',z') = J_a(y')J_b(z') = (1)\ 2H(y') \ ,$$

$$J_b(z') \simeq 1 \ ,$$

So $J_a(y') \simeq 2H_y(y')$ Amperes/meters

where $H_y(y')$ is the magnetic field due to the y-directed magnetic current line which is located near the fence on the conducting plane.
Therefore equation (3-15) becomes,

$$J(z') = \int_{-a}^{a} J_b(z')\ e^{jkz'\mathrm{Cos}\theta}\ dz' \simeq 2a \ ,$$

and equation (3-14) may be written in the form,

$$E_{\theta f}(\theta) = \frac{jk\eta e^{-jkr}}{4\pi r}\ \mathrm{Sin}\theta\ (2a)\ I\ (y') \ , \qquad (3\text{-}16)$$

where

$$I(y') = \int_{-\infty}^{\infty} 2\bar{H}_y(y')dy' .$$

To evaluate equation (3-16) the integral I(y') must be evaluated. From equation (3-5), an expression for $\bar{H}_y(y')$ can be obtained as given in equation (3-17). I(y') can only be evaluated by numerical integration. Fig. 3-7 shows a y-directed extended magnetic source with the presence of the fence.

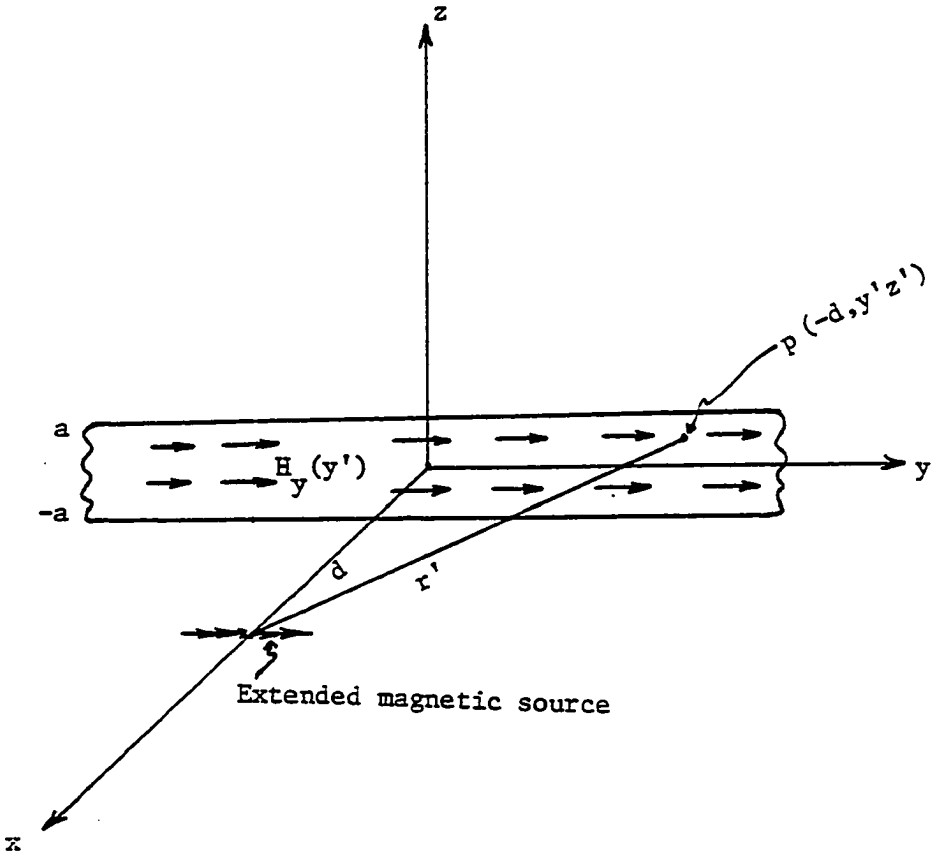

Fig. 3-7. Configuration of magnetic line with presence of the fence

$$H_y(y') = \frac{y'|K\ell|e^{-jkr'}}{4\pi r'}\left(\frac{1}{\eta r'^2} + \frac{1}{j\omega\mu r'^3}\right)\cos\alpha$$

$$+ \frac{y'z'|K\ell|}{4\pi r'\sqrt{x'^2+y'^2}}\left(\frac{j\omega\varepsilon}{r'} + \frac{1}{\eta r'^2} + \frac{1}{j\omega r'^3}\right)\sin\alpha \; . \qquad (3\text{-}17)$$

A computer program was developed to calculate $H_y(y')$ at any position on the fence due to the extended magnetic current source by means of superposition. The inverse relation of $H_y(y')$ in equation (3-17) with r' makes $H_y(y')$ weaker as distance along y' increases. Although the fence is infinitely long, there is no need to find values for $H_y(y')$ very far away from the magnetic current source.

From the numerical result obtained, the $H_y(y')$ was found to be less than 10% of its maximum beyond $y' = \pm 0.6$ meters, for f = 400.6 MHz, total $|k\ell| = 10.0$, and d = 0.22 meters. Knowing the values of $H_y(y')$ at this region on the fence was sufficient to evaluate the integral I(y'). A numerical method must be used to evaluate this integral. Equation (3-17) shows expression for integrand of I(y'). A simpler expression for this integrand was obtained as follows:

A group of data was fed to a curve-fitting routine from the I.S.U. Computation Center Library. This routine determines the coefficients of a fourth degree polynomial equations to fit a curve to the data. These equations were then used to evaluate the integral. Figs. 3-8 and 3-9

show the fitted curves and the corresponding data which were supplied for the real and imaginary parts of $H_y(y')$.

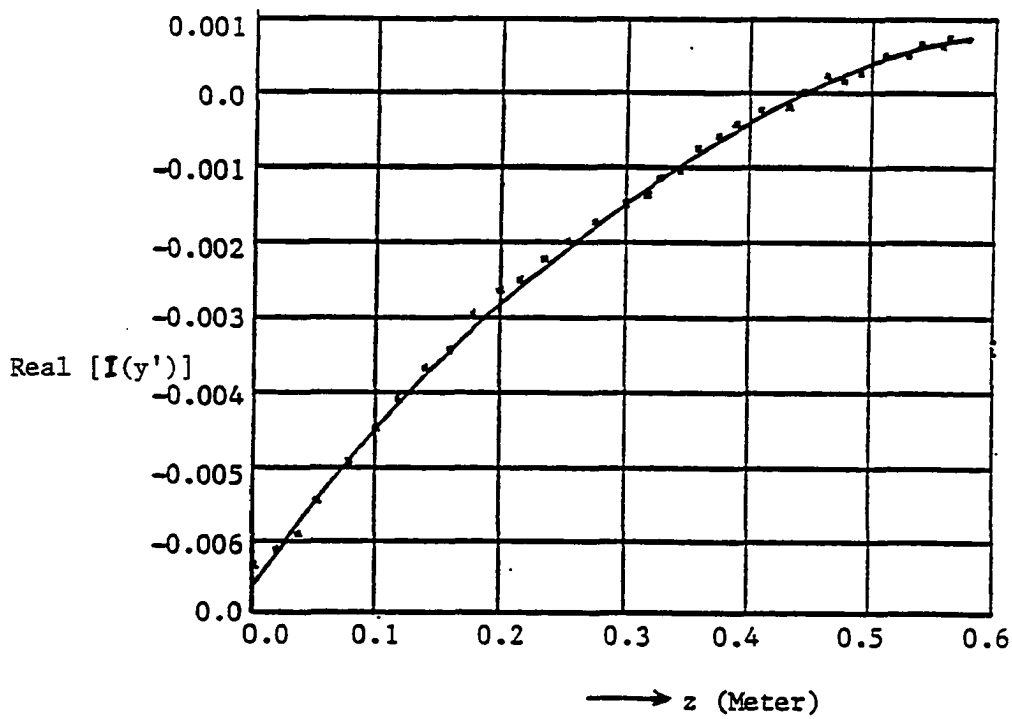

Fig. 3-8. Fitting Curve for real part of integrand of I(y')

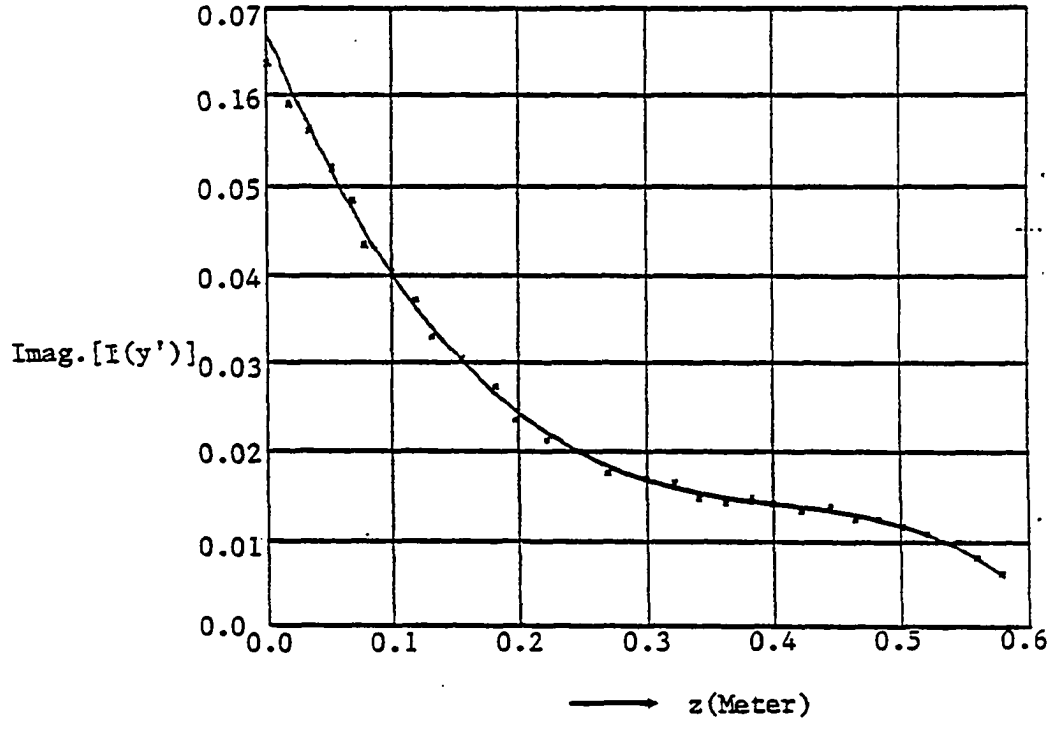

Fig. 3-9. Fitting curve for imaginary part of integrand of I(y')

The resulting fourth degree polynomials are:

Real part of $[H_y(y')] = -0.46\ y'^4 + 0.59\ y'^3 - 0.4\ y'^2 + 0.25\ y' - 0.066.$

Imaginary part of $[H_y(y')] = -0.407\ y'^4 - 0.2\ y'^3 + 0.65\ y'^2 - 0.33\ y' - 0.67.$

Then I(y') can be evaluated as follows:

$$I(y') = 2\left[\int_0^{0.6} \text{Real}\ [H_y(y')]\ dy' + j\int_0^{0.6} \text{Imag}\ [H_y(y')]\ dy'\right],$$

$$\text{Real}\ [H_y(y')] = \int_0^{0.6} -0.46y'^4 dy' + \int_0^{0.6} 0.59\ y'^3 dy' + \int_0^{0.6} -0.4y'^2 dy'$$

$$+ \int_0^{0.6} 0.25y'dy' - \int_0^{0.6} 0.066\ dy' = -0.011456,$$

$$\text{Imag}\ [H_y(y')] = \int_0^{0.6} -0.407y'^4 dy' + \int_0^{0.6} -0.2y'^3 dy' + \int_0^{0.6} 0.65\ y'^2 dy'$$

$$+ \int_0^{0.6} -0.33y'dy' + \int_0^{0.6} -0.67dy' = -0.7572$$

Finally,

$$I(y') = 2\left[-0.011456 - j0.7572\right] . \qquad (3\text{-}18)$$

Substituting (3-18) into (3-16)

$$E_{\theta f}(\theta) = \frac{jk\eta\, e^{-jkr}}{4\pi r} \mathrm{Sin}\theta\ (2a)\ (2)\ (-0.1145 - j0.7572) ,$$

$$E_{\theta f}(\theta) = \frac{4jk\ a\ \eta\ e^{-jkr}}{4\pi r} \mathrm{Sin}\theta\ \left(0.757287\ e^{-j1.586}\right) ,$$

$$E_{\theta f}(\theta) = 3.03\ \frac{jka\eta}{4\pi r} \mathrm{Sin}\theta\ e^{-j(kr + 1.586)} . \qquad (3\text{-}19)$$

Equation (3-19) gives the radiation pattern in the θ-direction due to the fence only. This has been called $E_{\theta f}(\theta)$ to distinguish it from $E_{\theta m}(\theta)$ which gives the radiation pattern in the θ-direction due to the magnetic extended source.

C. The Total Far-Field Pattern

The total field at any observation point can now be calculated using the superposition of the fence and magnetic current source. Fig. 3-10 shows the geometry for this superposition.

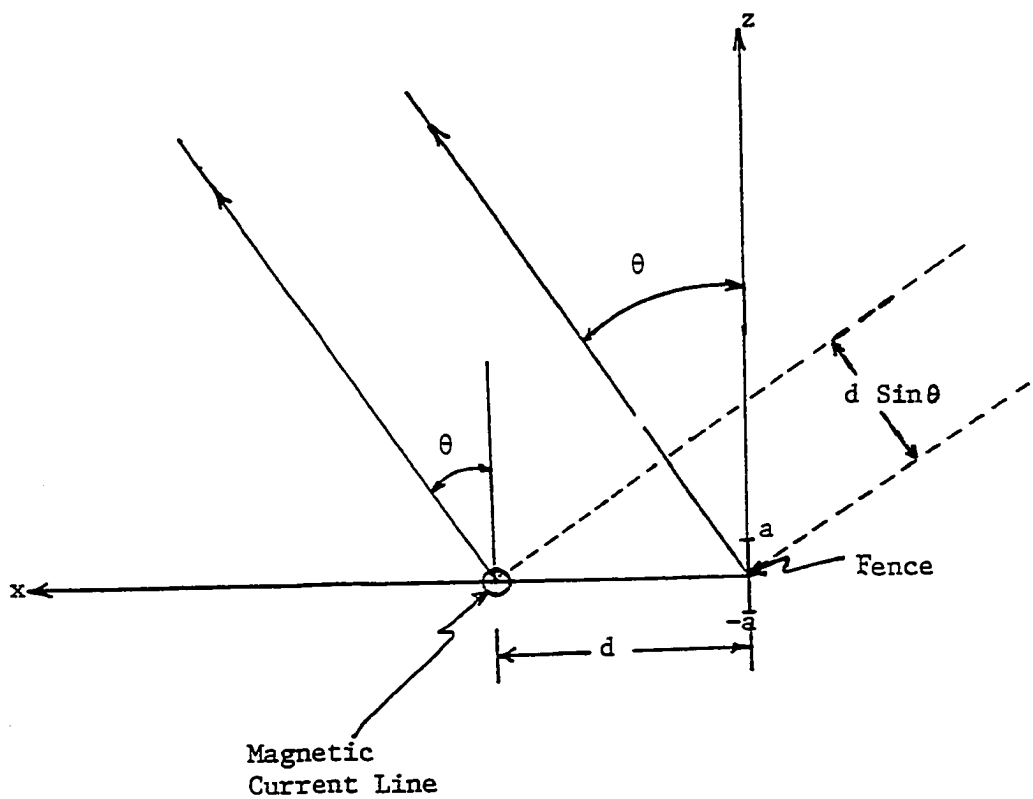

Fig. 3-10. A two element array with spacing of d

At every point in space, $E_{\theta m}(\theta)$ can be converted from rectangular to the cylindrical coordinates.

$$E_{\theta m}(\theta) = E_x \, \mathrm{Cos}\theta \, \mathrm{Cos}\phi + E_y \, \mathrm{Cos}\theta \, \mathrm{Sin}\phi - E_z \, \mathrm{Sin}\theta,$$

and for $\phi = 0$ the above equation becomes,

$$E_{\theta m}(\theta) = E_x \, \mathrm{Cos}\theta - E_z \, \mathrm{Sin}\theta. \qquad (3\text{-}20)$$

Substituting equations (3-1) and (3-3) into equation (3-20), we write

$$E_{\theta m}(\theta) = \frac{-z|k\ell|}{4\pi\sqrt{x^2+z^2}} e^{jkr}\left(\frac{jk}{r} + \frac{1}{r^2}\right) \mathrm{Cos}\theta \, \mathrm{Sin}\alpha$$

$$- \frac{x|k\ell|}{4\pi\sqrt{x^2 + z^2}} e^{jkr} \left(\frac{jk}{r} + \frac{1}{r^2}\right) \mathrm{Sin}\,\theta \, \mathrm{Sin}\alpha,$$

Where $\mathrm{Cos}\,\theta = \dfrac{z}{\sqrt{x^2+ z^2}}$, and $\mathrm{Sin}\theta = \dfrac{x}{\sqrt{x^2 + z^2}}$

$$E_{\theta m}(\theta) = \frac{-|K\ell|}{4\pi} e^{jkr} \left(\frac{jk}{r}\right) \mathrm{Cos}^2\theta \, \mathrm{Sin}\alpha - \frac{K\ell}{4\pi} e^{jkr} \left(\frac{jk}{r}\right) \mathrm{Sin}^2\theta \, \mathrm{Sin}\alpha,$$

$$E_{\theta m}(\theta) = -\frac{jk|K\ell|}{4\pi r} e^{jkr} \sin\alpha \left(\cos^2\theta + \sin^2\theta\right)$$

$$= -\frac{jk|K\ell|}{4\pi r} e^{jkr} \sin\alpha \cdot \qquad (3\text{-}21)$$

Since the pattern in the xz-plane or θ-plane is considered, then

$\alpha = 90^0$ and equation (3-21) becomes:

$$E_{\theta m}(\theta) = \frac{-jk|K\ell|}{4\pi r} e^{jkr}. \qquad (3\text{-}22)$$

And the expression for the total far-field is,

$$E_\theta(\theta) = E_{\theta f}(\theta) + E_{\theta m}(\theta)\ e^{jkd \sin\theta},$$

$$E_\theta(\theta) = \begin{cases} \frac{jk}{4\pi r} e^{-jkr} \left[3.03a\eta e^{-j1.586 \sin\theta} - |K\ell|\ e^{jkd \sin\theta}\right], & \text{for } \theta > 0^0 \\ \\ \frac{jk}{4\pi r} e^{-jkr} \left[3.03a\eta e^{-j1.586 \sin\theta} + |K\ell| e^{jkd \sin\theta}\right], & \text{for } \theta < 0^0 \end{cases} \qquad (3\text{-}23)$$

Equation (3-23) is the expression for the far-field due to the fence and the magnetic current source. This pattern is illustrated in Fig. 3-12 for the following dimensions:

The height of the fence = ±0.0508 meters

The length of the fence = ±0.66 "

The length of the extended source = ±0.1785 "

The distance between slot and fence = 0.22 "

The distance of total radiation from the origin = 10 meters

The total radiation is plotted as a function of θ, where θ varies from -90° to +90° (See Fig. 3-11).

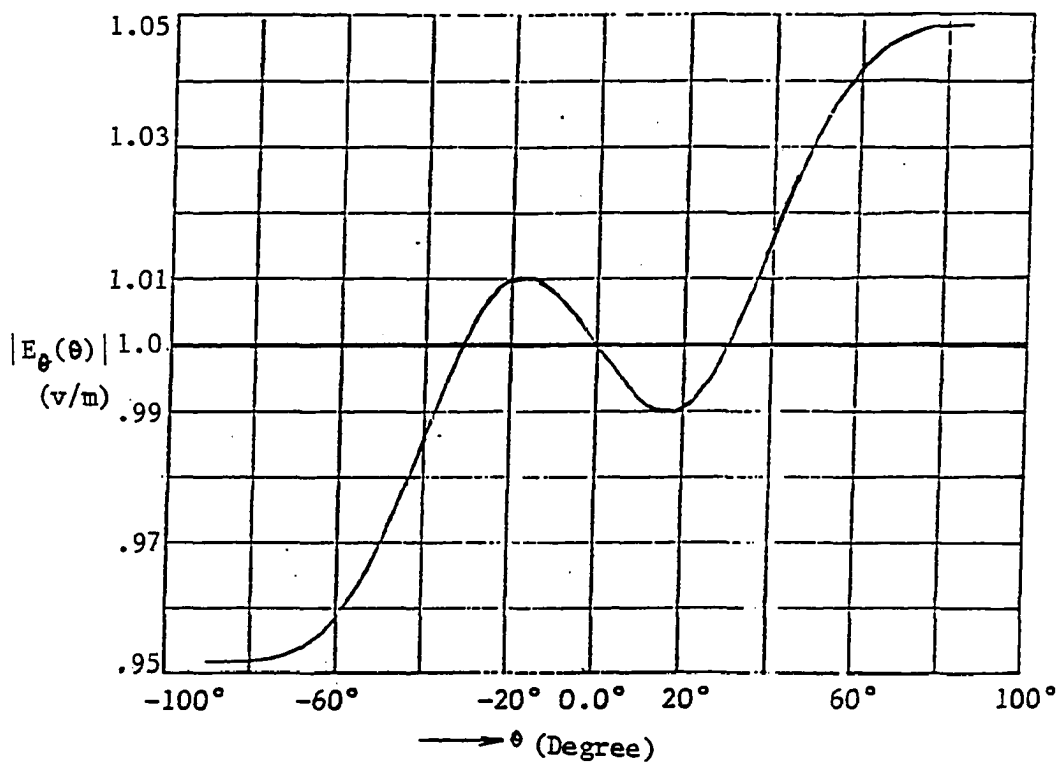

Fig. 3-11. The total radiation pattern of the fence and Magnetic Current Line

D. Investigation of Total Far-Field Pattern Using NEC

The modified NEC was used to determine the total far-field pattern of the fence in the presence of the extended magnetic source. This was done to develop confidence in the program, and to check the validity of assuming a surface current $|\bar{J}_s| = 2|\bar{H}_{tan}|$ in the analytical method. Two different ways are available to model the objects, wire-grid and surface patch models. The length of segments in the wire-grid model should not be greater than $\frac{\lambda}{10}$, and the area of patches in the surface patch model should not be greater than $\frac{\lambda^2}{25}$ for reasonable accuracy. The wire-grid model can be used on open and/or closed bodies, but the surface patch model can be used only on closed bodies (4).

Since the fence is an open surface, the wire-grid model was chosen for use in calculating the far-field pattern of the fence in the presence of the extended magnetic source. A total of 88 segments was used to cover the entire fence within the limitations.

For programming convenience, the fence was located in the yz-plane centered on the origin, and the z-directed extended magnetic source was symmetrically positioned meters away along the x-axis. Fig. 3-12 shows this configuration. The radiation pattern was then taken in the xy-plane (z=0) as a function of ϕ.

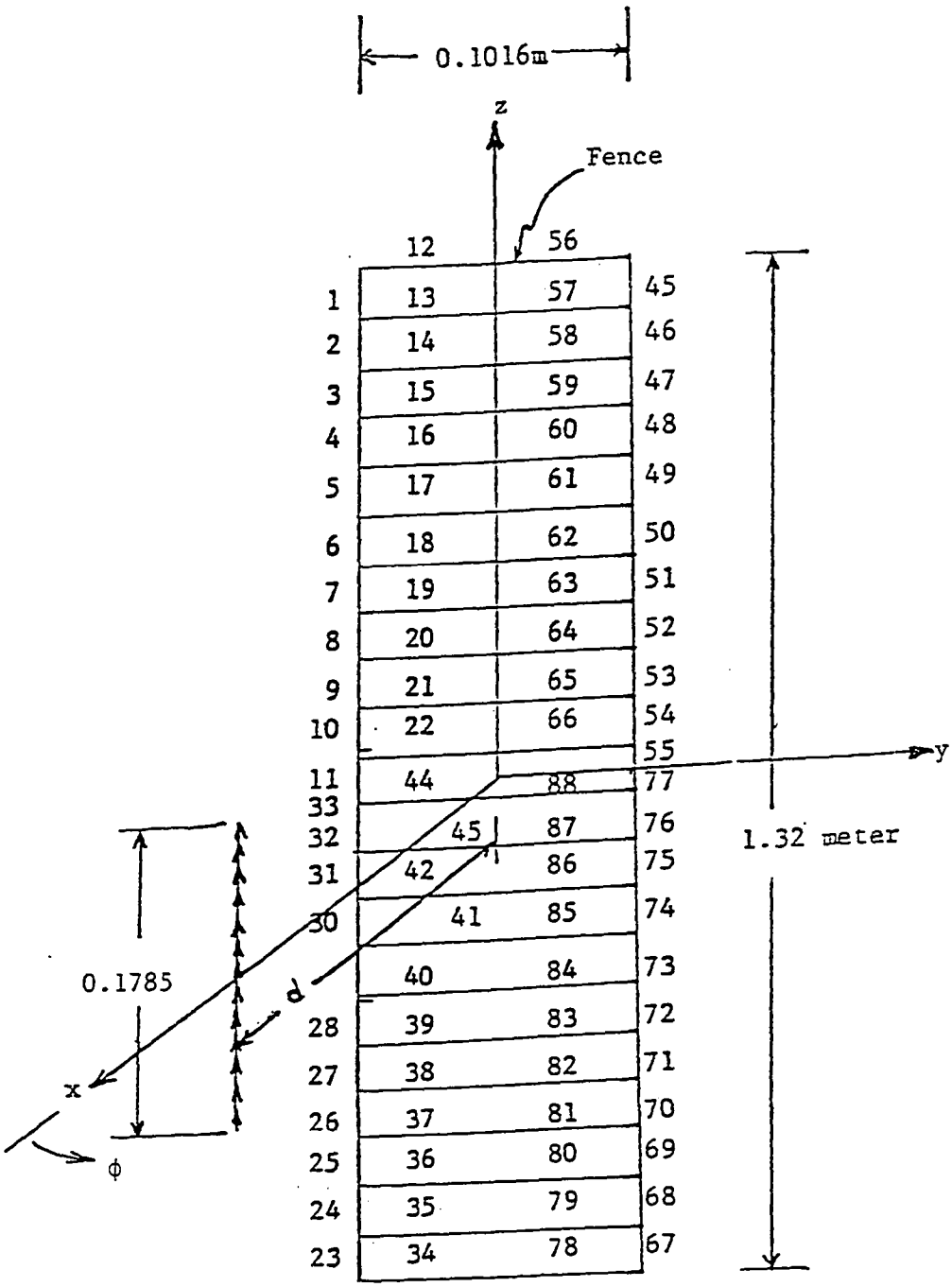

Fig. 3-12. Model of the fence in terms of the segments with the presence of the extended magnetic source

E. Discussion of the Results

In the planar analysis, considered here, the pattern due to the extended magnetic current is omidirectional (in Fig. 3-11, it would be a constant 1 v/m). But the presence of the fence causes a variation in the pattern of about ±5%, as seen in Fig. 3-11.

Results from NEC have been analyzed in the same manner as above. The presence of the fence caused a variation of about ±4%, which compares probably with that obtained by the analytical approach. This difference is probably attributable to the analytical assumption that has been made for the current distribution on the fence (J_{sz}).

The interference due to the fence predicted by both of these methods was small compared to the apparent effect of the columns on the cylindrical object as measured earlier on the experimental model. This discrepancy was important in determining the direction of further research.

From a consideration of the cylindrical configuration of the PDP, it would be expected that a standing wave pattern would be set up by wave propagating in opposite directions around a slotted smooth cylinder. This standing wave phenomenon does not exist in the planar analysis (both theoretical and NEC methods).

As a result of the above-mentioned discrepancy between the planar-analysis predictions and empirical measurements, as well as the failure of the planar techniques to account for standing wave behavior, it was decided that the planar configuration was not an adequate model for the

PDP problem. Therefore, no further study of the planar model was made. Instead, the analytical approach was extended to the actual cylindrical configuration of a cylinder with axial columns (fences) attached to it, with the microstrip antenna panels represented by axially-positioned slots or magnetic current elements on the surface of the cylinder.

IV. EXTENSION OF THE ANALYTICAL METHOD TO THE CYLINDRICAL CONFIGURATION

Consider an infinetly long smooth cylinder with an axial slot as in Fig. 4-1. The field radiates waves from the slot which propagate around the cylinder in either direction with equal amplitude and 180° phase shift, as in Fig. 4-2.

Therefore, depending on the radius of the cylinder, and the amount by which the wave amplitudes are attenuated by radiation, different standing waves could result. The amount of scattering from an axial fence or column should depend upon where that fence is located relative to the standing wave on the smooth cylinder. Experimentally, the perturbation of the far-field radiation pattern was found to be dependent on the column position relative to the radiating slot. This is the effect for which we are looking in the analytical model.

To obtain the total radiation pattern, the superposition theorem will be used, i.e., by summing the complex radiated fields due to the slotted cylinder only, and the fields due to the currents induced on the fences in the presence of the cylinder.

Harrington (10) derives the near-field expressions for E_z and E_ϕ, but the expressions for E_ρ and H_z (which are the main concern in the near field) are not included. The expressions for E_ρ and H_z are derived in the Appendix.

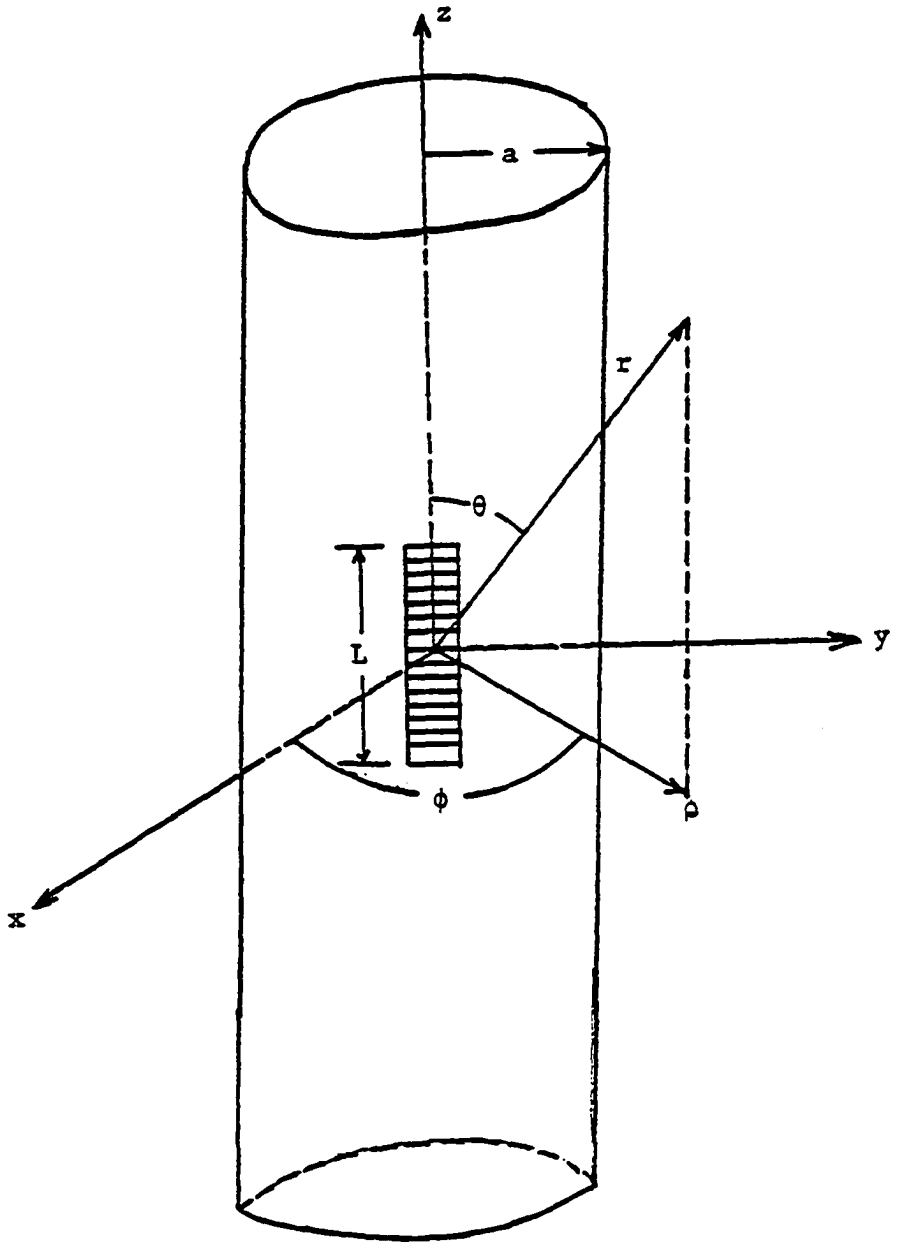

Fig. 4-1. An infinitely long conducting cylinder with an axial slot

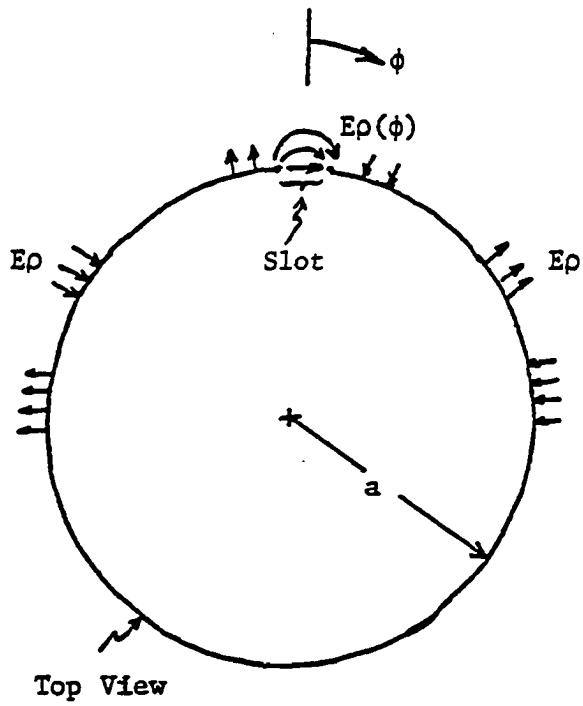

Fig. 4-2. Top view of a cylinder with an axial slot, and the electric field in the wave propagating circumferentially from the slot

A. Far-Field Radiation Pattern Due to the Slotted Cylinder Only

To find an expression for the far-field radiation pattern for the case of the slotted cylinder without any fences, the asymptotic form of the Bessel function is used as $r \to \infty$, in equations 10-6 and 10-7.

Therefore,

$$(A_z)_{r\to\infty} = \frac{e^{-jkr}}{\pi r} \sum_{n=-\infty}^{\infty} e^{jn\phi}\, j^{n+1}\, f_n(-k\,\mathrm{Cos}\theta).$$

$$(F_z)_{r\to\infty} = \frac{e^{-jkr}}{\pi r} \sum_{n=-\infty}^{\infty} e^{jn\phi}\, j^{n+1}\, g_n(-k\,\mathrm{Cos}\theta).$$

Inserting these into equation (10-9), the expression for $E_\phi(\rho,\phi,z)$ for the far-field becomes

$$E_\phi = \frac{VLe^{-jkr}}{\pi^3 ar}\left[\frac{\mathrm{Cos}\left(\frac{KL}{2}\mathrm{Cos}\theta\right)}{1-\left(\frac{KL}{\pi}\mathrm{Cos}\theta\right)^2}\right] \sum_{n=-\infty}^{\infty} \frac{j^n\, e^{jn\phi}}{H_n^{(2)'}(ka\,\mathrm{Sin}\theta)} \qquad (4\text{-}1)$$

where: L is the length of the slot

V is the excitation voltage across the slot

a is the radius of the cylinder

$H_n^{(2)'}(ka\ \mathrm{Sin}\theta)$ is the derivative of the Hankel function of the second kind.

Since the radiation pattern in the ϕ-plane is the main concern, then $\theta = 90^0$ and equation (4-1) becomes,

$$E_\phi = \frac{VLe^{-jkr}}{\pi^3 ar}\left[\sum_{n=-\infty}^{\infty} \frac{j^n e^{jn\phi}}{H_n^{(2)'}(ka)}\right], \qquad (4\text{-}2)$$

The coefficient $\frac{VLe^{-jkr}}{\pi^3 ar}$ for the relative radiation pattern is assumed to be unity. So

$$E_\phi = \sum_{n=-\infty}^{\infty} \frac{j^n e^{jn\phi}}{H_n^{(2)'}(ka)}, \qquad (4\text{-}3)$$

where: $H_n^{(2)'}(ka) = J'_n(ka) - jN'_n(ka).$ (4-4)

$J_n(ka)$ is the Bessel function of the first kind and

$N_n(ka)$ is the Bessel function of the second kind.

A routine from the I.S.U. Computation Center Library was used to determine $J_n(x)$

and $N_n(x)$. Then, using recurrence relations and a computer program,

$H_n^{(2)'}(ka)$ was found as follows:

Letting $B_n(x)$ represent $J_n(x)$, and $N_n(x)$, and

$$B'_n(x) = \frac{B_{n-1}(x) - B_{n+1}(x)}{2}, \qquad (4\text{-}5)$$

$J'_n(x)$ and $N'_n(x)$ were determined from (4-5). Then using equation (4-5), $H_n^{(2)'}(ka)$ was calculated. Another computer program has been developed to evaluate E_ϕ and find the number of terms necessary for an accuracy of better than 5%. For this accuracy, a total of 40 terms was found to be needed:

$$E_\phi = \sum_{n=-20}^{20} \frac{j^n e^{jn\phi}}{H_n^{(2)'}(ka)} \qquad (4\text{-}6)$$

Equation (4-6) is the one that was used to evaluate E_ϕ. Fig. 4-3 shows the amplitude pattern, and Fig. 4-4 shows the corresponding phase angle, for the value ka = 4.47 (which is the actual value for the object being modeled). The phase information will become important when adding this electric field to that resulting from scattering by the fences.

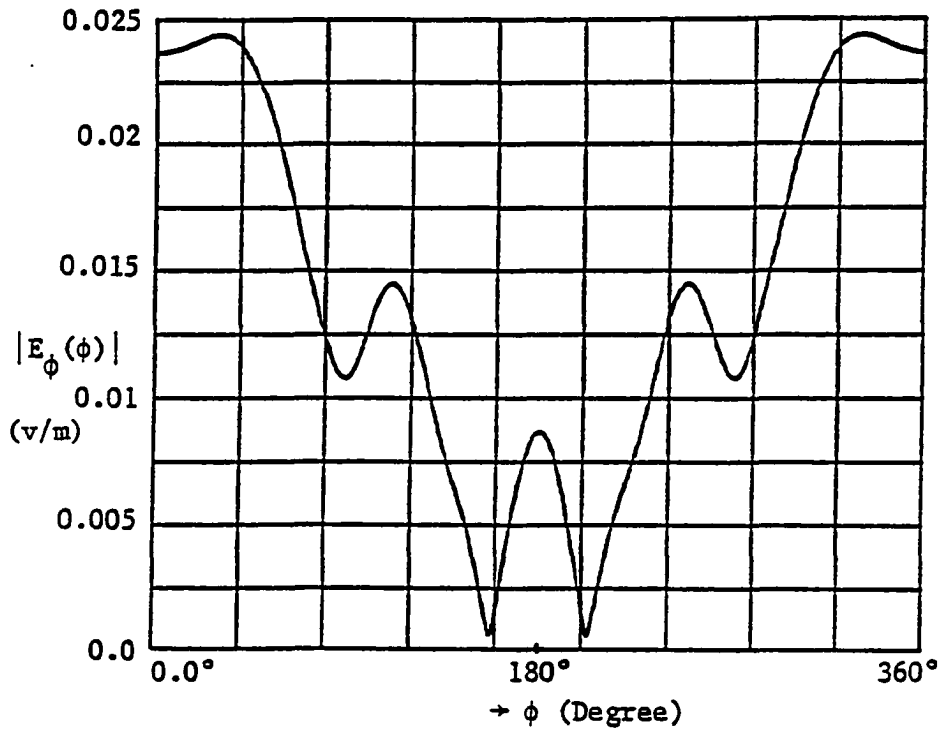

Fig. 4-3. Far field radiation pattern due to a conducting smooth cylinder with an axial slot on it (this pattern was taken at a distance of 10m, and $|k\ell| = 0.1785$ A)

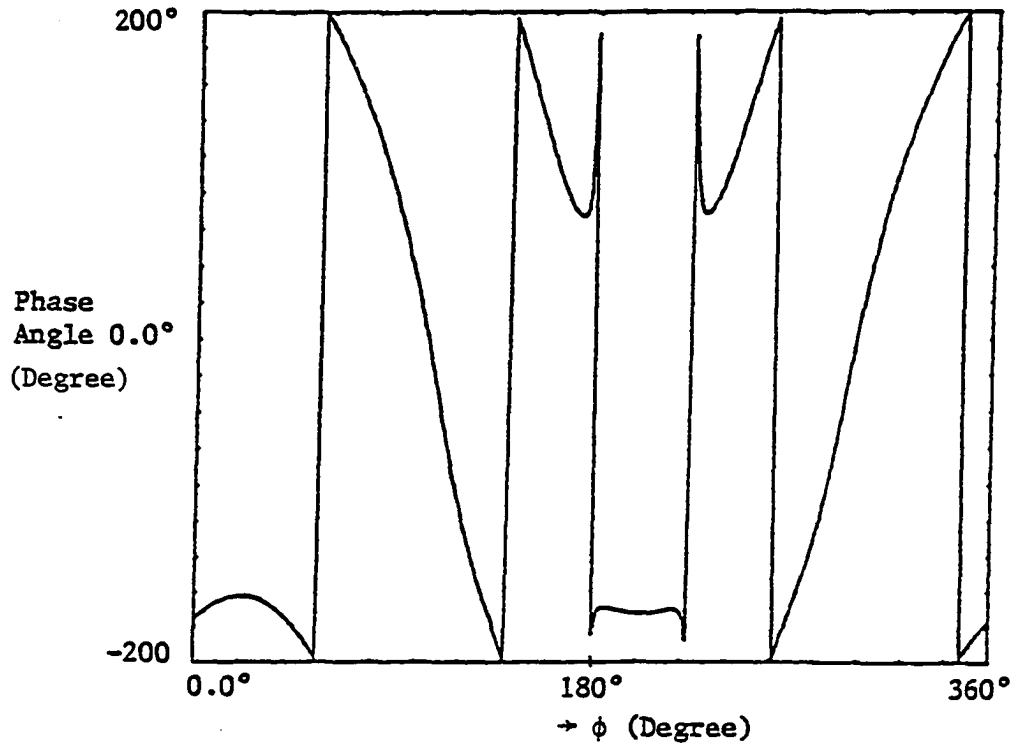

Fig. 4-4. Corresponding phase angle for radiation pattern of a conducting smooth cylinder with slot on it

B. Developing the Formula and Far-Field Radiation Pattern due to a Single Fence on a Cylinder

This pattern is due to the current induced in the fence from the radiating slot. Therefore, the current distribution induced by the source on the fence is needed.

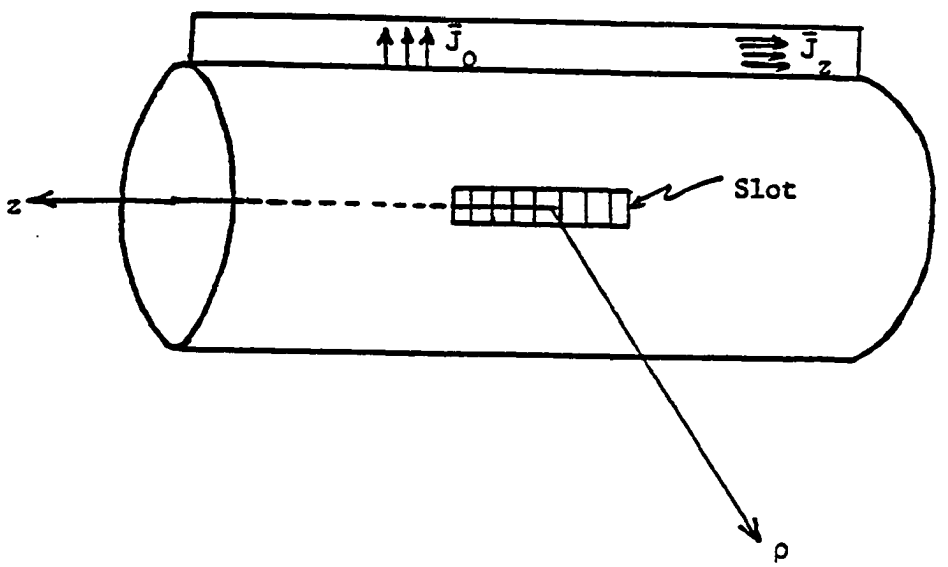

Fig. 4-5. Slotted conducting cylinder with an axial fence

Fig. 4-5 shows the location of the fence on the smooth conducting cylinder near the source (slot). The current induced on the fence from the source is related to the incident $\bar{E}$ and $\bar{H}$ components by the boundary conditions at the conducting fence surface. Since the cylinder is a

perfect conductor, and from the boundary conditions, the important component of $\overline{H}$ is H_z because it relates to the current induced to the fences. E_ρ is also of interest, because from the boundary conditions we would anticipate that scattering from the fence would be strongest when the fence is located at a point where E_ρ is maximum. So the near-field expression for H_z is required for computing J_ρ, and the E_ρ expression is of interest in analyzing qualitatively the effect of the fence position. From equations (10-10) and (10-11), the expression for $E_\rho(\rho,\phi,z)$ becomes:

$$E_\rho(\rho,\phi,z) = \frac{1}{2\pi} \sum_{n=-\infty}^{\infty} \frac{n}{j\rho} \frac{\overline{E}_\phi(n,w) H_n^{(2)}\left(\rho\sqrt{k^2-w^2}\right)}{\sqrt{k^2-w^2}\, H_n^{(2)'}\left(a\sqrt{k^2-w^2}\right)} e^{jwz} dw, \qquad (4\text{-}7)$$

where:

$$\overline{E}_\phi(n,w) = \frac{1}{2\pi} \int_0^{2\pi} d\phi \int_{-\infty}^{\infty} E_\phi(a,\phi,z) e^{-jn\phi}\, e^{-jwz} dz. \qquad (4\text{-}8)$$

The position of the slot and relative angle in the ϕ direction has been shown in Fig. 4-6. To evaluate equation (4-7), the $\overline{E}_\phi(n,w)$ must be investigated. This term can be written in the form

$$\overline{E}_\phi(n,w) = \overline{E}_\phi(n)\, \overline{E}(w). \qquad (4\text{-}9)$$

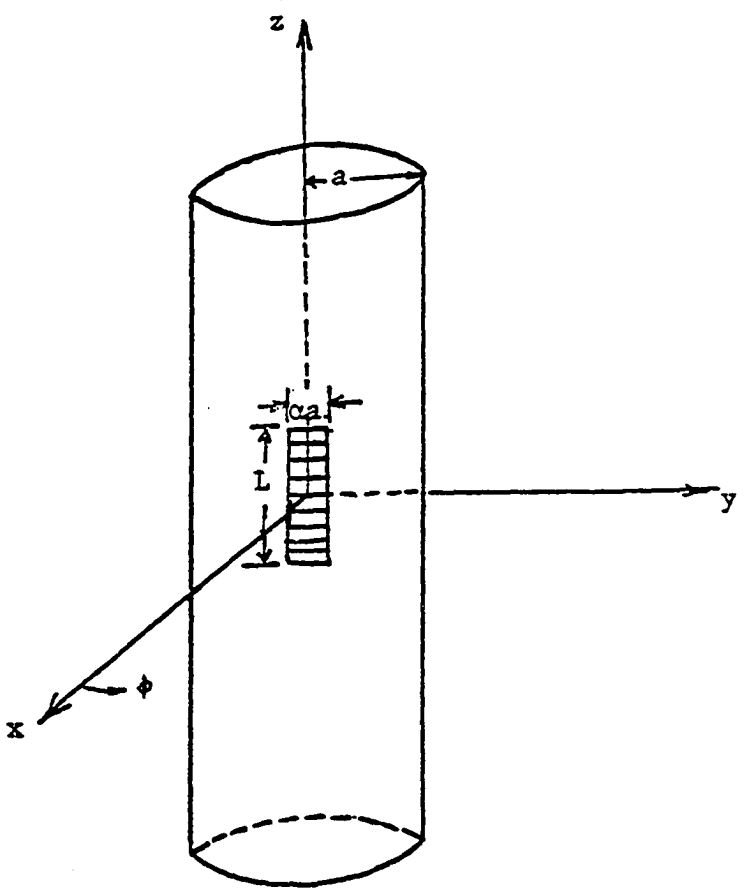

Fig. 4-6. A conducting cylinder and an axial slot with the angular width of αa

To evaluate equation (4-20) the following steps were taken:

Expression for the "n" part of $\overline{E}_\phi(n,w)$:

$$\overline{E}_\phi(n) = \frac{1}{2\pi} \int_0^{2\pi} E_\phi(\phi)\, e^{-jn\phi} d\phi, \text{ where } E_\phi(\phi) = \begin{cases} \frac{V}{\alpha a}, & -\frac{\alpha}{2} < \phi < \frac{\alpha}{2} \\ 0, & \text{elsewhere} \end{cases}$$

$$\overline{E}_\phi(n) = \frac{V}{2\pi\alpha a} \int_{\frac{-\alpha}{2}}^{\frac{\alpha}{2}} e^{-jn\phi}\, d\phi = \frac{V}{2\pi\alpha a} \left[\frac{1}{-jn} e^{-jn\phi}\right]_{\frac{-\alpha}{2}}^{\frac{\alpha}{2}},$$

$$\overline{E}_\phi(n) = \frac{jv}{2\pi\alpha an} \left[e^{-j\frac{n\alpha}{2}} - e^{+j\frac{n\alpha}{2}}\right] = \frac{2V}{2\pi\alpha an} \left[\text{Sin } \frac{n\alpha}{2}\right],$$

$$\overline{E}_\phi(n) = \left(\frac{V}{2\pi a}\right) \frac{\text{Sin}\left(\frac{n\alpha}{2}\right)}{\left(\frac{n\alpha}{2}\right)}. \qquad (4\text{-}10)$$

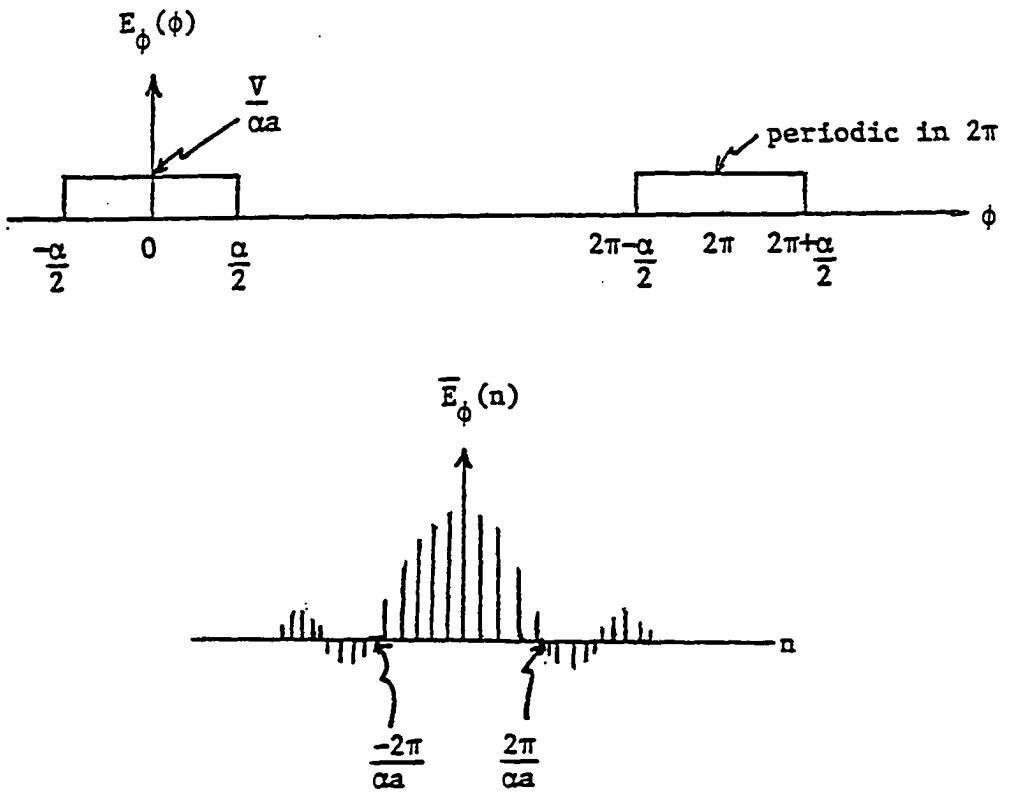

Fig. 4-7. $E_\phi(\phi)$ and its corresponding Fourier transform

Values of equation (4-10) for different n are coefficients in an exponential Fourier series for $E_\phi(\phi)$. The "average" value is for n=0: namely, $\frac{V}{2\pi a}$. This is correct, by inspection. Amplitudes of spectral components obey a $\frac{\text{Sin } x}{x}$ envelope, as we expect from a "narrow pulse" signal.

Expression for the "w" part of $\bar{E}_\phi(n,w)$:

$$\text{Since } \bar{E}_\phi(z) = \begin{cases} 1 \ , & \frac{L}{2} < z < \frac{L}{2} \\ 0 \ , & \text{elsewhere} \end{cases}$$

$$\overline{E}_\phi(w) = \int_{-\infty}^{\infty} E_\phi(z)\, e^{-jwz}\, dz = \int_{-\frac{L}{2}}^{\frac{L}{2}} e^{-jwz} dz = \left[\frac{1}{-jw}\, e^{-jw^z}\right]_{-\frac{L}{2}}^{\frac{L}{2}},$$

$$\overline{E}_\phi(w) = \frac{j}{w}\left[e^{-j\frac{wL}{2}} - e^{+j\frac{wL}{2}}\right] = L\,\frac{\mathrm{Sin}\left(\frac{wL}{2}\right)}{\left(\frac{wL}{2}\right)}. \qquad (4\text{-}11)$$

Substituting (4-21) and (4-22) into (4-20),

$$\overline{E}_\phi(n,w) = \frac{VL}{2\pi\alpha}\,\frac{\mathrm{Sin}\left(\frac{n\alpha}{2}\right)}{\left(\frac{n\alpha}{2}\right)}\;\frac{\mathrm{Sin}\left(\frac{wL}{2}\right)}{\left(\frac{wL}{2}\right)}. \qquad (4\text{-}12)$$

Substituting (4-23) into (4-8), we obtain,

$$E_\rho(\rho,\phi,z) = \frac{1}{2\pi}\,\frac{VL}{2\pi a}\,\frac{1}{j\rho}\sum_{n=-\infty}^{\infty}\mathrm{Sin}\left(\frac{n\alpha}{2}\right) e^{jn\phi}\int_{w=-\infty}^{\infty}\frac{H_n^{(2)}\left(\rho\sqrt{k^2-w^2}\right)}{H_n^{(2)'}\left(a\sqrt{k^2-w^2}\right)}$$

$$\frac{1}{\sqrt{k^2-w^2}}\left[\frac{\mathrm{Sin}\left(\frac{wL}{2}\right)}{\left(\frac{wL}{2}\right)}\right] e^{jwz}\,dw. \qquad (4\text{-}13)$$

For numerical evaluation, we must determine how far out the limits of n

and w should go. Limits on n will depend on behavior of $\frac{H_n^{(2)}(\rho\sqrt{k^2-w^2})}{H_n^{(2)'}(a\sqrt{k^2-w^2})}$, since the other n-dependent term does not drop off steadily with n but rather is periodic. A study of $H_n^{(2)}/H_n^{(2)'}$ shows $n = \pm 20$ is satisfactory for an accuracy of ± 5%. For the limits of the integral on w in the equation (4-13), to cover just the central "lobe" in the $[\frac{\text{Sin}(\frac{wL}{2})}{(\frac{wL}{2})}]$ function, we could set $\frac{wL}{2} = \pi$ and find $w = \frac{2\pi}{L}$ for limits (96% of the power is in the main lobe of a $\frac{\text{Sin } x}{x}$ function).

$$E_\rho(\rho,\phi,z) = \sum_{n=-20}^{20} e^{jn\phi} \text{Sin}\frac{n\alpha}{2} \int_{w=-\frac{2\pi}{L}}^{\frac{2\pi}{L}} \frac{H_n^{(2)}(\rho\sqrt{k^2-w^2})}{\sqrt{k^2-w^2}\, H_n^{(2)'}(a\sqrt{k^2-w^2})} \left[\frac{\text{Sin}(\frac{wL}{2})}{\frac{wL}{2}}\right] e^{jwz} dw. \qquad (4\text{-}14)$$

Equation (4-14) is a near-field expression for the ρ component of the electric field due to a slot on the conducting cylinder. To evaluate this expression, a numerical method of integration was chosen.

By inspection of the symmetry of the integrand and the summand, we may write equation (4-14) in the form of

$$E_\rho(\rho,\phi,z) = 4j \sum_{n=0}^{20} \text{Sin } n\phi \text{ Sin } \frac{n\alpha}{2} \int_0^{\frac{2\pi}{L}} \frac{H_n^{(2)}\left(\rho\sqrt{k^2-w^2}\right)}{\sqrt{k^2-w^2}\, H_n^{(2)'}\left(a\sqrt{k^2-w^2}\right)}$$

$$\left[\frac{\text{Sin}\left(\frac{wL}{2}\right)}{\left(\frac{wL}{2}\right)}\right] \text{Cosz dw.} \qquad (4\text{-}15)$$

At w=k the only singularity occurs, but it can be removed by using asymptotic forms (as w approaches k) for the Hankel functions in the numerator and denominator. For w>k the argument becomes imaginary, and the following procedure must be used instead to evaluate

$H_n^{(2)}$ and $H_n^{(2)'}$.

$$H_n^{(2)}\left(-j\rho\sqrt{w^2-k^2}\right) = + \frac{2j}{\pi} e^{jn\frac{\pi}{2}} \; k_n\left(\rho\sqrt{w^2-k^2}\right) , \qquad (4\text{-}16)$$

$$H_n^{(2)'}\left(-ja\sqrt{w^2-k^2}\right) = - \frac{2}{\pi} e^{jn\frac{\pi}{2}} \; k_n'\left(a\sqrt{w^2-k^2}\right) , \qquad (4\text{-}17)$$

where k_n is a modified Bessel function.

The arguments of H_n^2 and $H_n^{(2)'}$ in equations (4-16) and (4-17) were chosen to have coefficients of -j in order that the functions successfuly converged.

The computer evaluation was successfully used to evaluate $E_\rho(\phi)$ at any ρ and z. Fig. 4-8 shows the magnitude of this near field

pattern for $\rho=a$, $z=0$, $a = 0.5335$ meters, and $f = 400.6$MHz as a function of ϕ. The figure suggests evidence of the intuitively expected standing wave pattern, as well as a smaller-scale periodicity arising from the numerical evaluation. The important consideration here is that the near-field drops off rapidly for angles greater than 15°. We conclude, therefore, that the sensitivity of the far-field pattern to small changes in the fence position will be greatest at slot-to-fence separations of up to about 15 degrees.

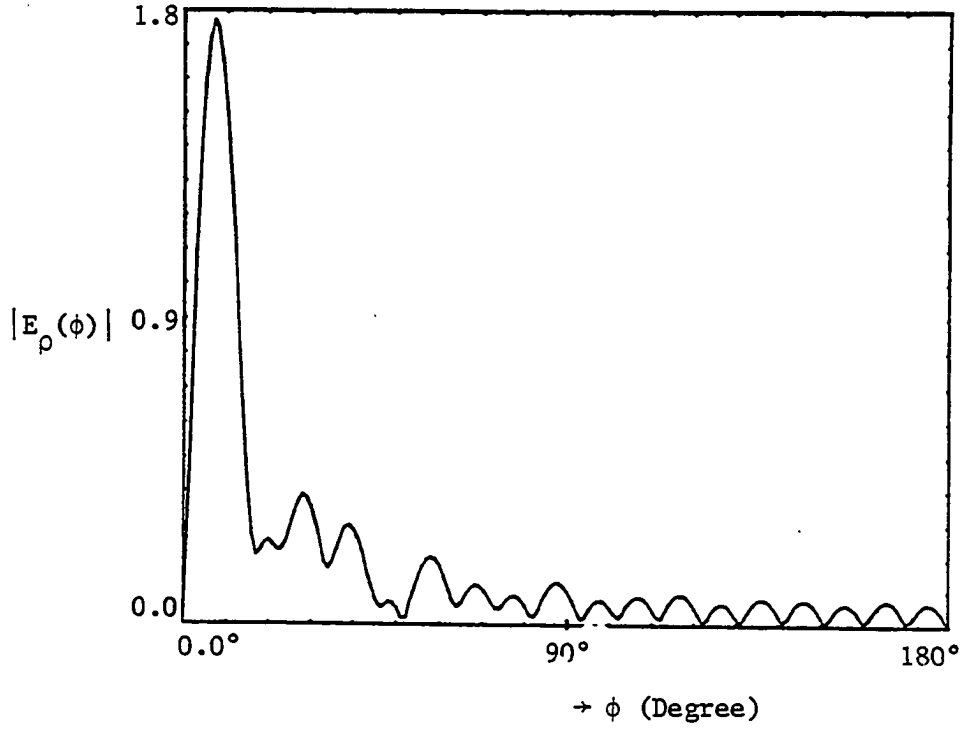

Fig. 4.8. Near field radiation pattern for $E_\rho(\phi)$, $\rho=a$, $z=0$, and $f=400.6$MHz

The current induced in the fence is directly related to the $\overline{H}$ components of the field radiating from the slot and evaluated tangential to the fence. From the boundary conditions, J_ρ is the only component that could exist on the fence. J_ρ at each position is related to H_z at that point, so the near field expression for H_z is required. Equation (10-11) in the Appendix shows this expression.

Sufficient terms for the summation and the limits of the integral in equation (4-12) for converging and adequate precision of the result are the same as equation (4-14). Therefore, the near-field expression for evaluating H_z numerically can be written as:

$$H_z(\rho,\phi,z) = -\frac{VL}{\pi^2 a} \sum_{n=0}^{19} \text{Cos}(n\phi) \left[\frac{\text{Sin}\left(\frac{n\alpha}{2}\right)}{\left(\frac{n\alpha}{2}\right)}\right] \int_0^{25.2} \frac{\left[\frac{\text{Sin}\left(\frac{wL}{2}\right)}{\left(\frac{wL}{2}\right)}\right] H_n^{(2)}\left(\rho\sqrt{k^2-w^2}\right)}{\sqrt{k^2-w^2}\, H_n^{(2)'}\left(a\sqrt{k^2-w^2}\right)}$$

$$\left(j\omega\varepsilon + \frac{w^2}{j\omega\mu}\right) e^{jwz} dw. \qquad (4\text{-}18)$$

The computer program which has been used for evaluating equation (4-14) was modified to evaluate equation (4-18) numerically. Fig. 4-9 shows the magnitude of H_z as a function of z for a fixed $\phi=25^0$ with respect to the slot. Knowing H_z, and using the assumption of $J_\rho=2(H_z)$, we can determine J_ρ at each point. $J_\rho(z)$ is the surface current density, in amperes per meter, along the fence.

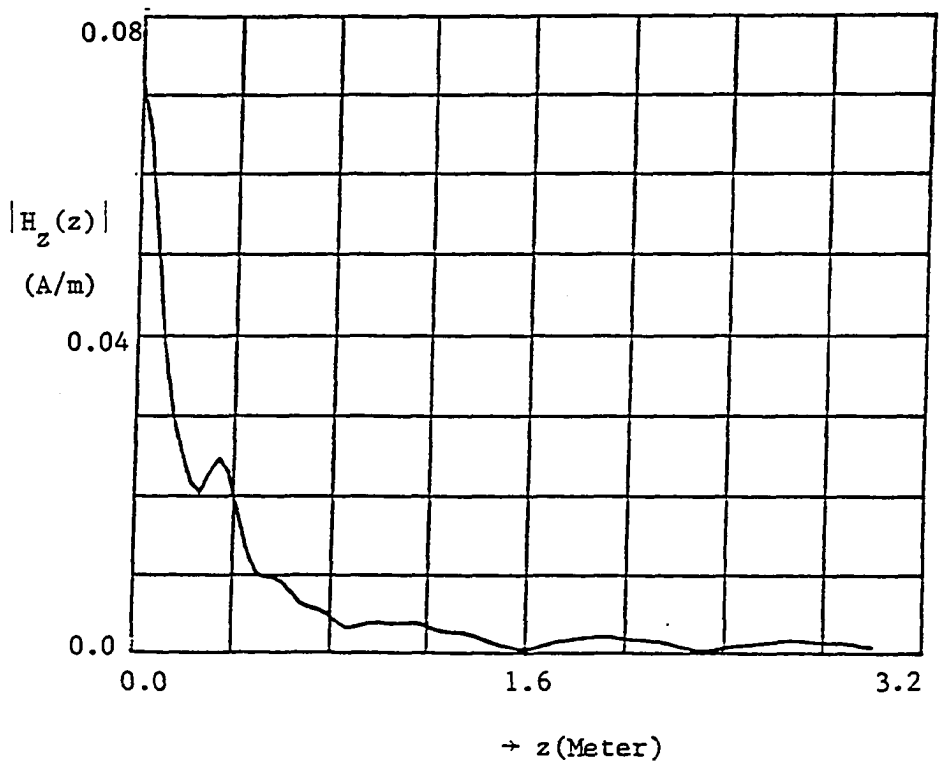

Fig. 4-9. Magnitude of $H_z(z)$ as a function of z with $\phi_s = 25°$

Now, in order to find the radiation pattern due to the fence, we can sum the radiation patterns due to a continuous distribution of radial electric monopoles perpendicular to the surface of a conducting cylinder. Considering Fig. 4-10, the far-field expression of the pattern (as a function of ϕ in the z=0 plane) for a single monopole is (10):

$$E_\phi = -\frac{2(I\ell)e^{-jk\rho}}{4\pi^2 ka\rho} \sum_{n=1}^{\infty} \frac{n(j)^n \sin n\phi}{H_n^{(2)'}(ka)}, \qquad (4\text{-}19)$$

where: $I\ell$ is a radial electric monopole, and ℓ is the monopole height measured in a direction perpendicular to the cylindrical surface. In the present application, the length of the fence will be divided into sections Δz in width, and each section will carry a current $I = J_\rho \Delta z$ amperes.

To evaluate equation (4-19) numerically, the first 28 terms of summation were enough for an accuracy of better than 2%.

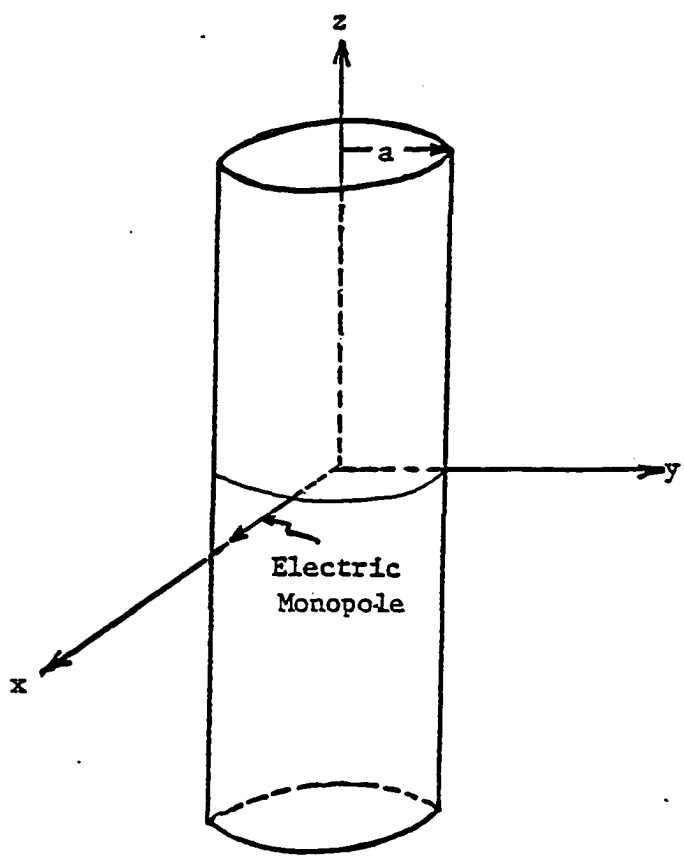

Fig. 4-10. A radially pointing electric monopole on a conducting cylinder

A number of sections of Δz, each having a current $I\ell$, thus represent the elements necessary for modeling the fence. The electric field E_ϕ can then be calculated for each $I\ell$ individually and these values summed to provide the field at that point due to the group of $I\ell$ elements. In order to find the far-field pattern due to the four fences (at $\phi = 25°$, $115°$, $205°$, $295°$ as shown in Fig. 4-11) the following steps are taken:

1. The H_z values are calculated along each of the fences using the above procedure. These values are computed at equally-spaced positions along the fence, with a spacing of $\Delta z = 0.01\text{m}$.

2. The electric monopole ($I\ell$) is computed at each fence position by using the above values of H_z and the assumption that $J_\rho = 2\ H_z$.

   Then

   $$I\ell = J_\rho \Delta z = 2(H_z)\Delta z \ .$$

3. Knowing the $I\ell$ element values along each of the fences, we can find the complex far-field radiation pattern for each fence. Then the total far-field pattern due to the fences is the phasor sum of the four individual patterns just obtained.

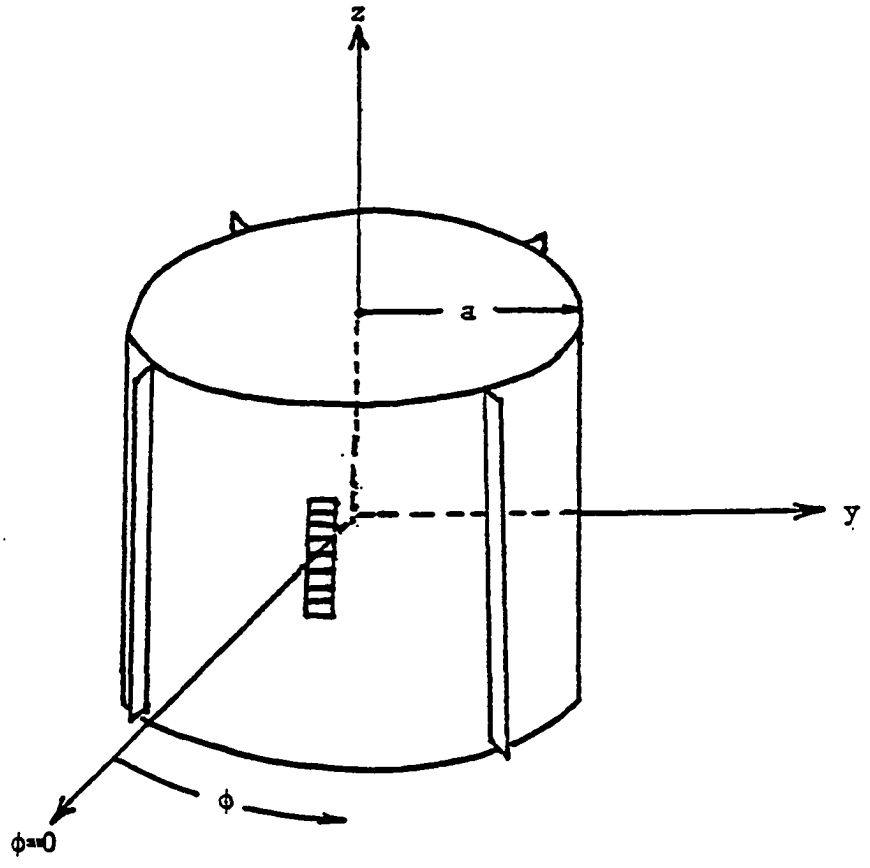

Fig. 4-11. A Conducting Cylinder with a slot and four fences

C. Total Far-Field Radiation Pattern

To find the total far-field radiation pattern, five different patterns must be added together, four patterns from the fences and one from the cylinder with slot only. In order to sum these patterns properly, the coordinates in Fig. 4-11 were rotated so that ϕ=0 is positioned midway between two fences (see Fig. 4-12 (21)).

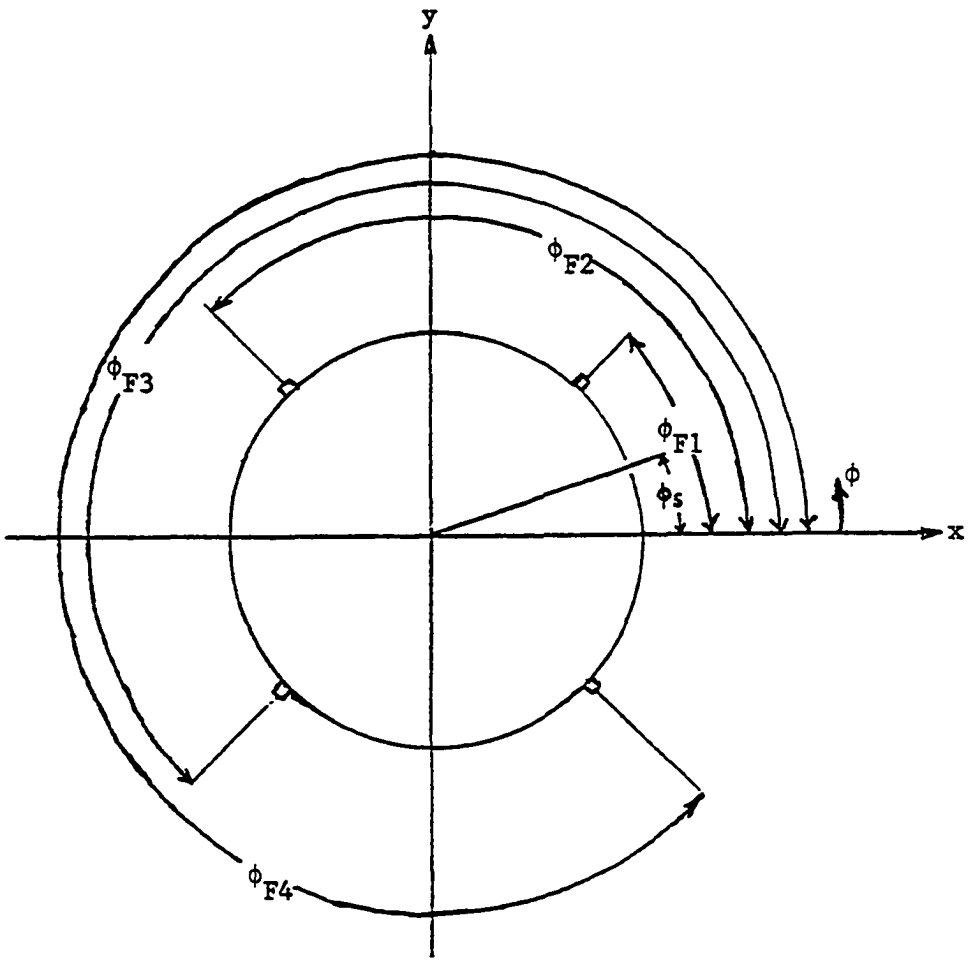

Fig. 4-12. Cross section in the plane of z = 0.0

Let us define the following terms:

$E_T(\phi)$ = The total far-field radiation pattern due to the sum of five patterns, as a function of position ϕ

$E_{\phi s}(\phi)$ = Far-field radiation pattern due to the slot on the conducting cylinder. The corresponding position of the slot is given by ϕ_s.

$E_{\phi F1}(\phi)$ = Far-field radiation pattern due to fence 1 only, positioned at an angle ϕ_{F1}.

$E_{\phi F2}(\phi)$ = Far-field radiation pattern due to fence 2, where ϕ_{F2} is the angle between ϕ=0 and this second fence.

$E_{\phi F3}(\phi)$ = Far-field radiation pattern due to fence 3, where ϕ_{F3} is the angle between ϕ=0 and this third fence.

$E_{\phi F4}(\phi)$ = Far-field radiation pattern due to fence 4, where ϕ_{F4} is the angle between ϕ=0 and the fourth fence.

Assuming that the slot is 25° from ϕ=0, then in order to sum the five patterns the shift shown in Table 4-1 has to be done to add these five patterns correctly. For a certain ϕ position in the far-field, the respective ϕ values listed must be used in each individual pattern to obtain the correct sum.

Table 4-1. Corresponding angular values of slot and fences with respect to ϕ

Far-field position	Angular values of ϕ to use in computing the field pattern				
	Slot	Fence 1	Fence 2	Fence 3	Fence 4
ϕ	ϕ_s	ϕ_{F1}	ϕ_{F2}	ϕ_{F3}	ϕ_{F4}
0°	-25°	-45°	-135°	-225°	-315°
10°	-15°	-35°	-125°	-215°	-305°
20°	- 5°	-25°	-115°	-205°	-295°
"	"	"	"	"	"
"	"	"	"	"	"
"	"	"	"	"	"
"	"	"	"	"	"
"	"	"	"	"	"
"	"	"	"	"	"
360°	-25°	-45°	-135°	-225°	-135°

Therefore, the total pattern of a slotted cylinder with four fences on its surface is:

$$E_T(\phi) = E_{\phi s}(\phi s) + E_{\phi F1}(\phi_{F1}) + E_{\phi F2}(\phi_{F2}) + E_{\phi F3}(\phi_{F3}) + E_{\phi F4}(\phi_{F4}). \quad (4\text{-}20)$$

It is understood that all terms in the equation (4-20) are complex. Figs. 4-13 and 4-14 show the magnitude and corresponding phase angle of total radiation pattern for the values of Table 4-1.

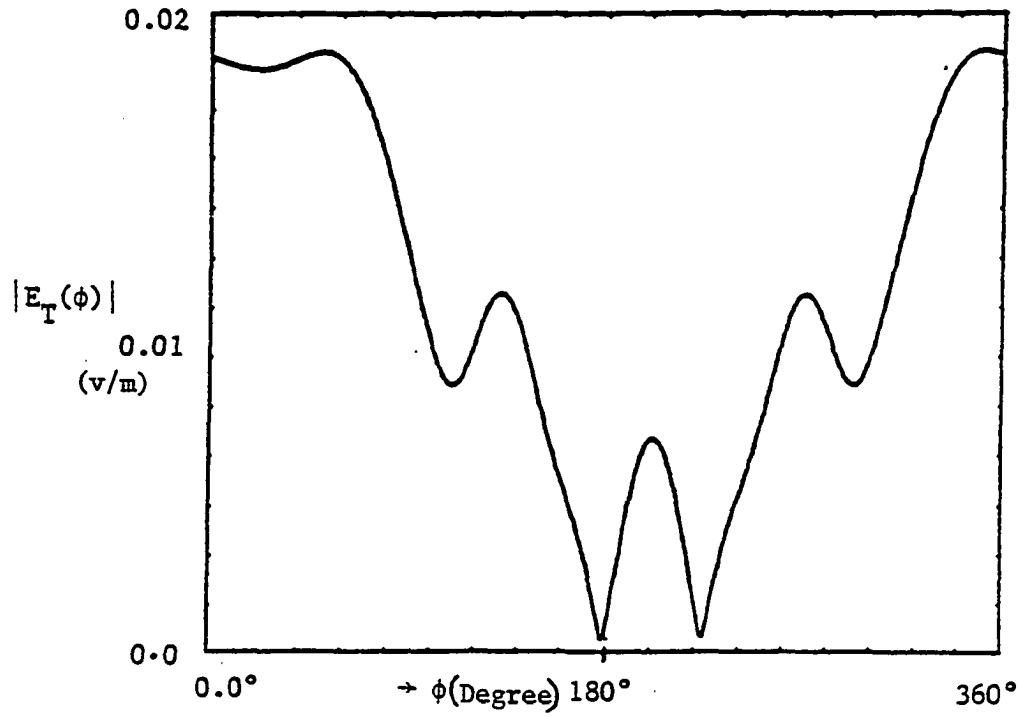

Fig. 4-13. The total radiation pattern due to the sum of five patterns with $\phi_s \approx 25^\circ$

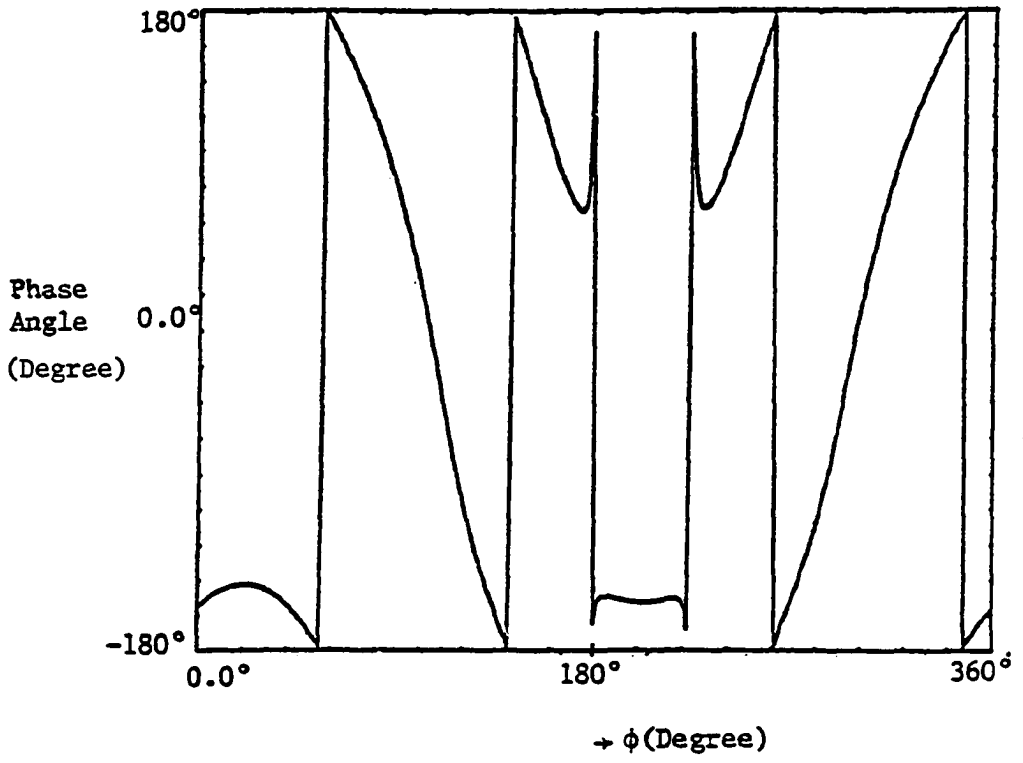

Fig. 4-14. Corresponding phase angle for E_T (ϕ)

Comparing $|E_T(\phi)|$ with the radiation pattern due to the slot only (Fig. 4-3), we see no effect of the columns on the radiation pattern. The only difference between these two patterns is a shift in Fig. 4-13 due to a shift in the slot position (Fig. 4-3 is for $\phi_s = 0^0$, whereas Fig. 4-13 is for $\phi_s = 25^0$).

The next computer run was for $\phi_s = 0^0$, and columns positioned the same as before (equally-spaced with respect to $\phi = 0^0$). $E_T(\phi)$ again was calculated following the procedure of Table 4-1. Figs. 4-15 and 4-16 shows the $|E_T(\phi)|$ and corresponding phase angle. Comparing $|E_T(\phi)|$ for this case with radiation pattern due to the slot only (Fig. 4-3) we find again that the effect of the columns is not visible at all; in fact, the two patterns are almost identical.

These results are in agreement with predictions based on the near-field patterns obtained in the previous sections. Considering Fig. 4-8, the near-field radiation pattern of $E_\rho(\phi)$, the columns positions of the last two runs were not in locations corresponding to large values of $|E_\rho(\phi)|$. Therefore, the far-field patterns are least affected by the presence of the columns. For example for this specific model and frequency, one can see that the most sensitive location on the cylinder should be at about $\phi = \pm 8^0$. To see and verify this effect, another run was made with a column located at $\phi = 8^0$. Figs. 4-17 and 4-18 show the $|E_T(\phi)|$ and the corresponding phase angle. Comparison of Fig. 4-17 with Fig. 4-3 shows that the symmetry of $|E_T(\phi)|$ has been affected somewhat.

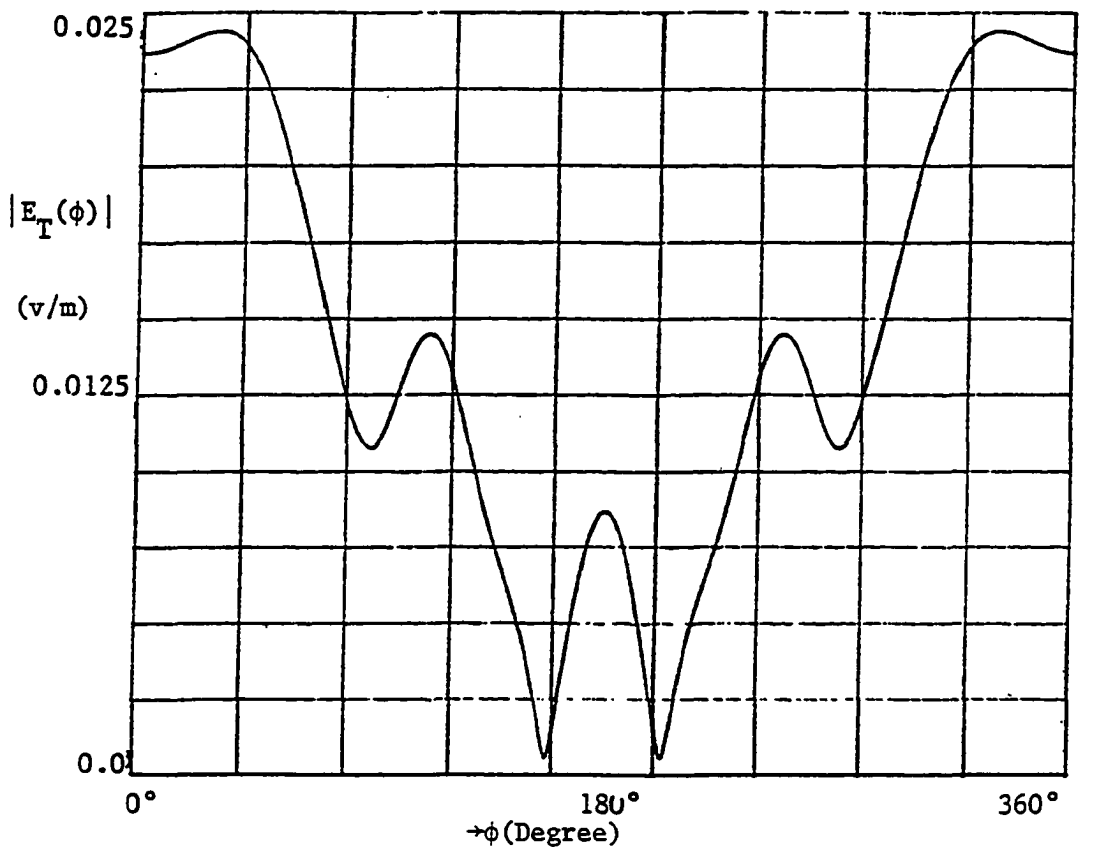

Fig. 4-15. Radiation pattern due to the slot at $\phi = 0^0$ with four equally-spaced columns

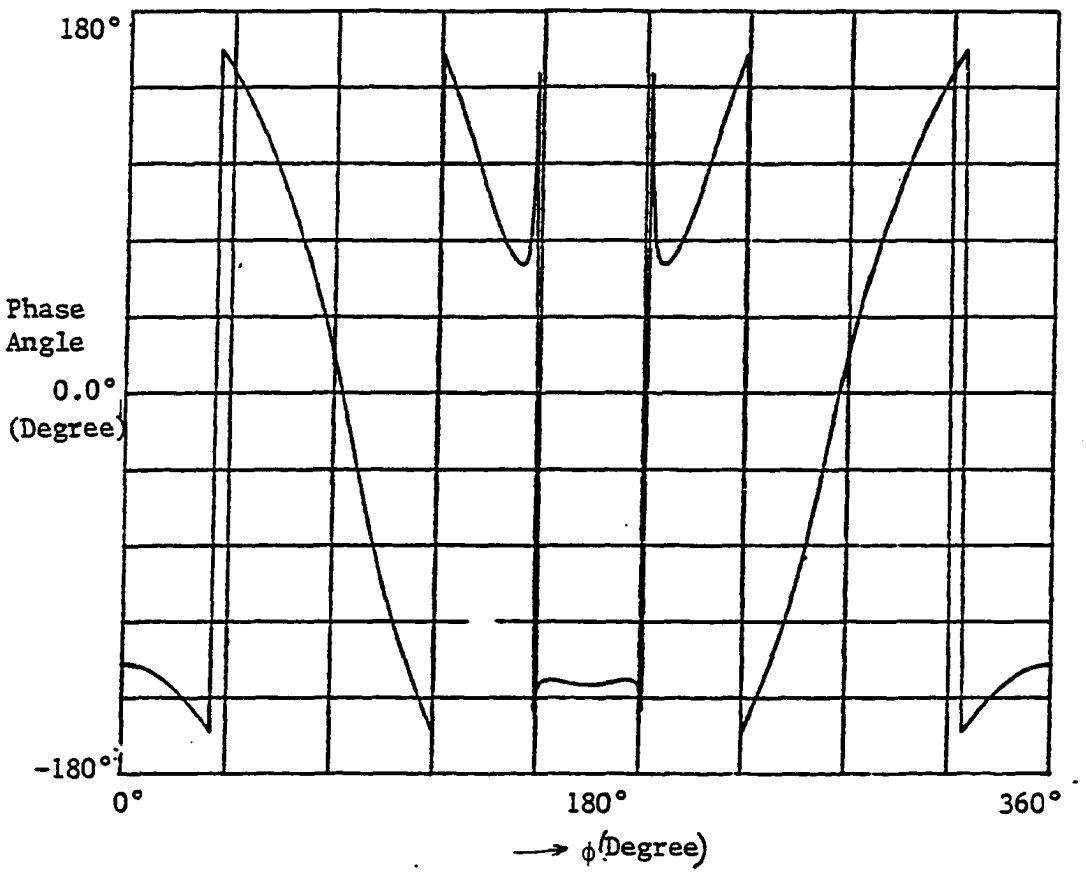

Fig. 4-16. Corresponding phase angle for slot at $\phi = 0^0$ with four equally-spaced columns

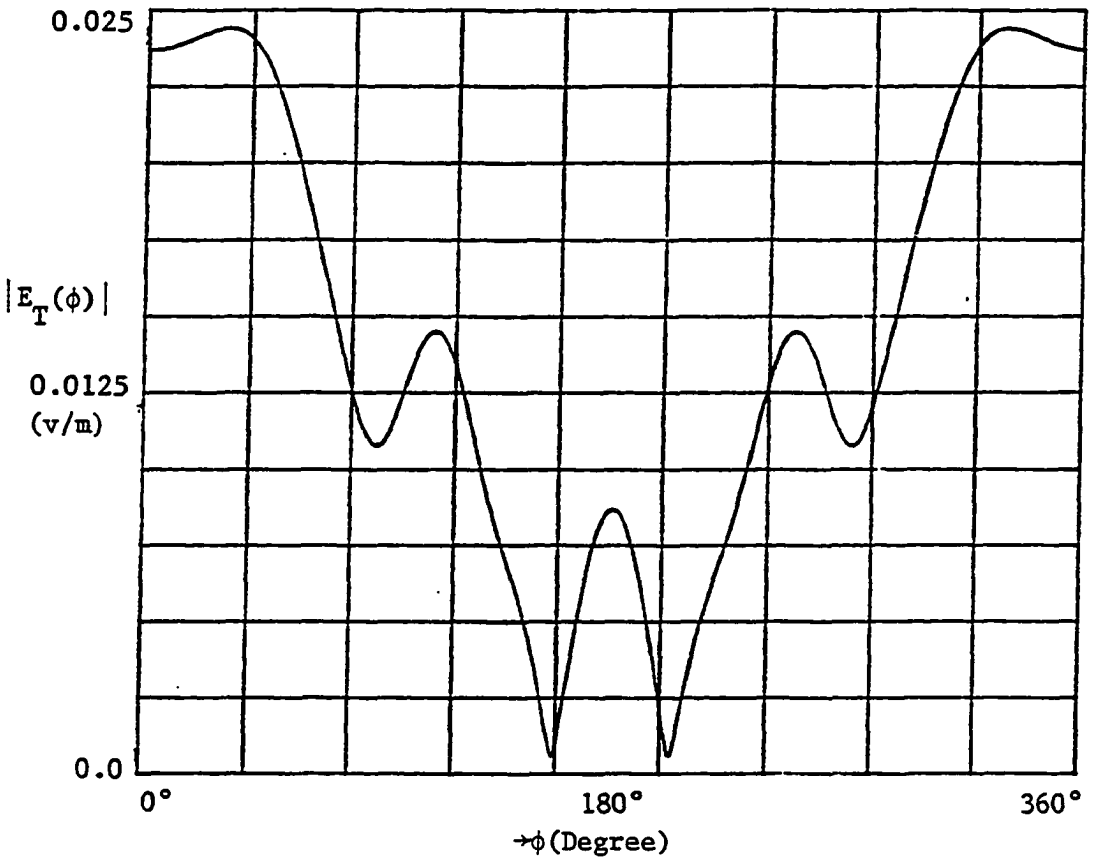

Fig. 4-17. Far-field radiation pattern of a slotted cylinder with a column at $\phi = 8^0$. The slot is at $\phi = 0^0$.

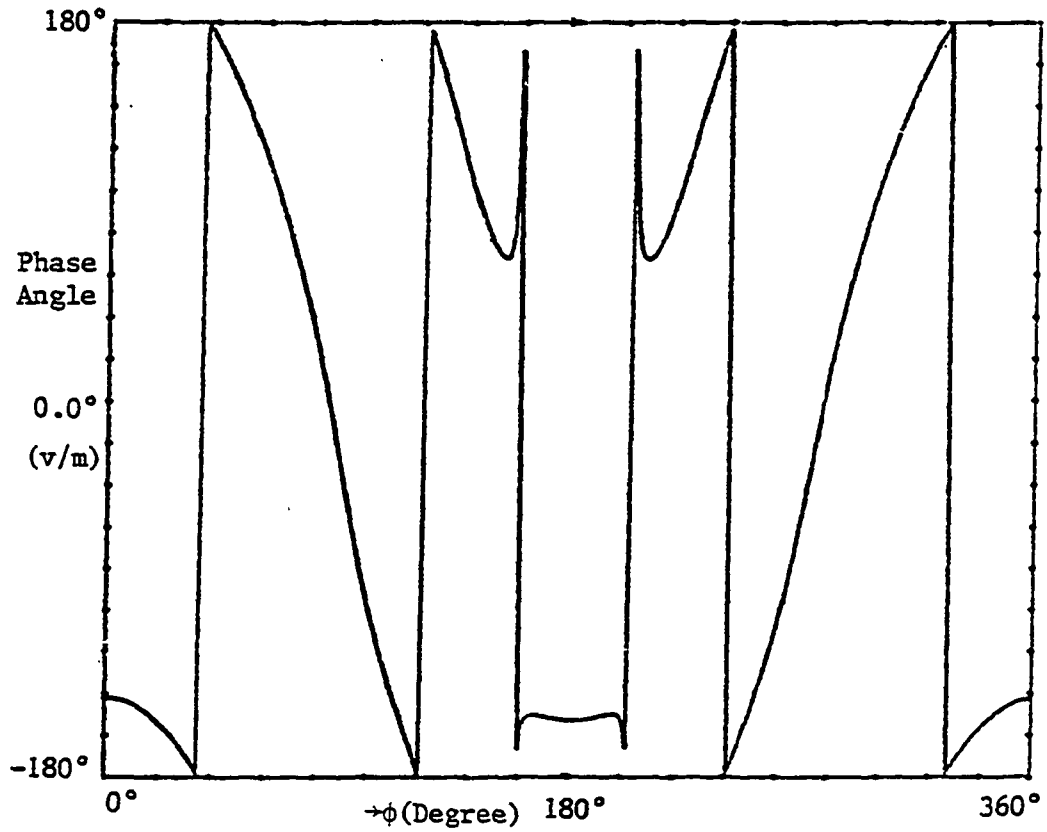

Fig. 4-18. Corresponding phase angle for a slotted cylinder with a columns at $\phi = 8^0$

This indicates that the effect of column position can be seen in the far-field pattern, as predicted by the theoretical analysis of this chapter, although this effect is small for this particular model. The planar analysis of Chapter 3 yields a similar conclusion: namely, that the effect of the fences on the far-field is not very great.

At this point, the experimental investigation became very important. We desired to repeat some radiation pattern measurements on the PDP model, using a half-scale model rather than the seventh-scale model on which many of the measurements in the original PDP study were made. This work is discussed in the next chapter.

V. LABORATORY WORK AND COMPARISON WITH THE ANALYTICAL MODEL

The analytical work of the preceding chapter suggested that the effect of the columns on the radiation pattern was less than had earlier been assumed. We sought to repeat some earlier pattern measurements, with special attention to making the parameters of the model as nearly identical to those of the analytical work as possible.

The experimental work has been based on the PDP specifications, but since a cylinder with PDP size is too large for the laboratory in this department, the physical dimensions were reduced by a factor two and the frequency was doubled. To verify earlier experimental patterns of the PDP (21), the microstrip panel which was used in those experiments was also chosen for use as the radiating element for the first part of this experiment.

Because the effect of the columns was the main concern, the patterns of this model with and without columns were desired. The physical model of Fig. 5-1 was used to obtain the radiation pattern of the PDP without columns, shown in Fig. 5-2. (All measured patterns in this chapter are relative field intensity).

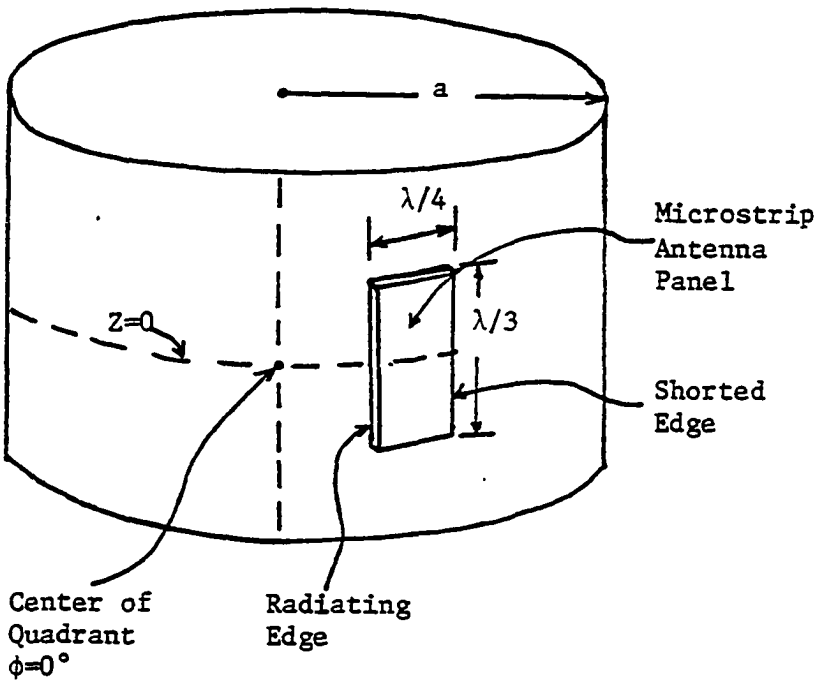

Fig. 5-1. PDP with one microstrip antenna panel which has its radiating edge at $\phi = 25^0$

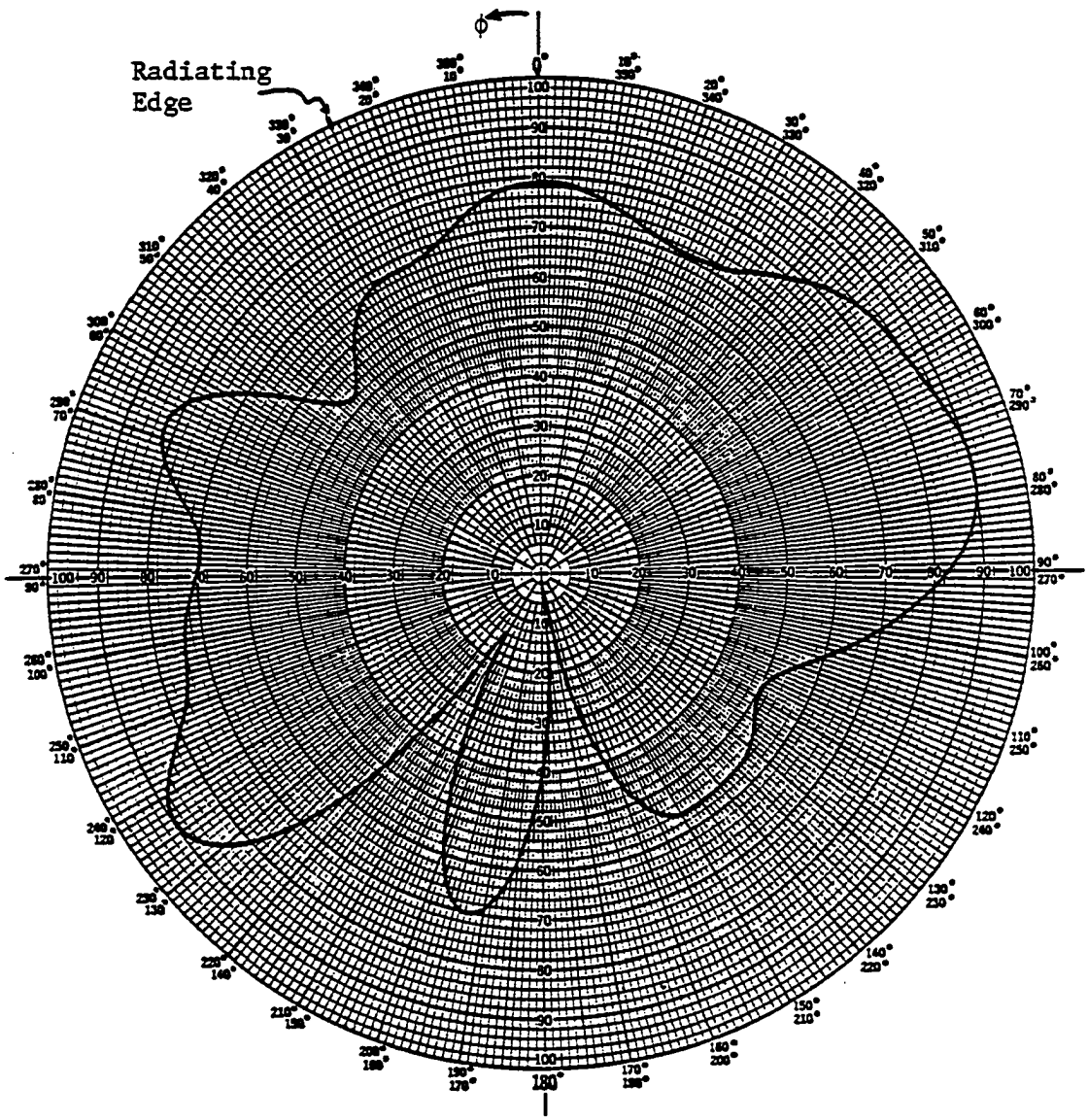

Fig. 5-2. Experimental far-field radiation pattern of a smooth conducting cylinder with one microstrip panel with radiating edge at $\phi = 25^0$

Then, four columns of 2.5 x 2.5 Cm. Cross-section, equal spacing, and symmetry with respect to $\phi = 0^0$ were mounted on the cylinder (Fig. 5-3).

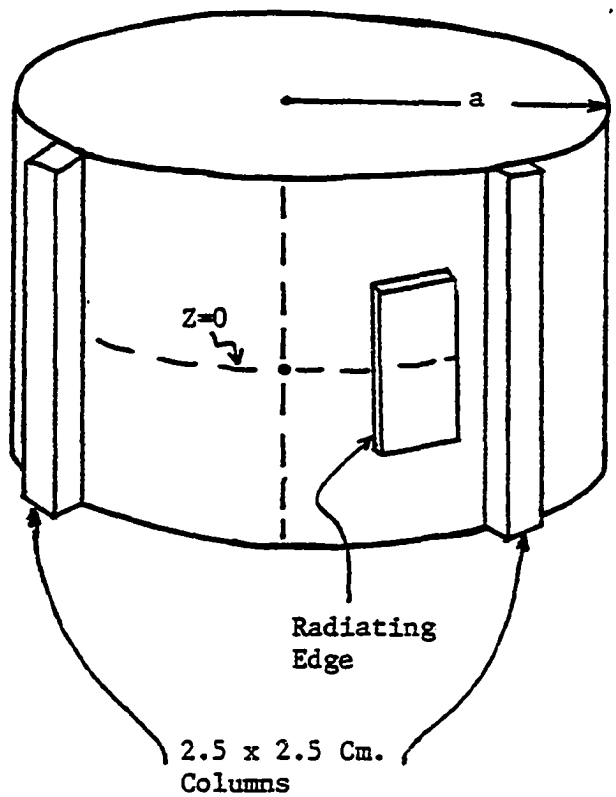

Fig. 5-3. PDP with one microstrip panel with radiating edge located at $\phi = 25^0$ and four 2.5 x 2.5 Cm. cross-section columns

The far-field radiation pattern for this model is shown in Fig. 5-4.

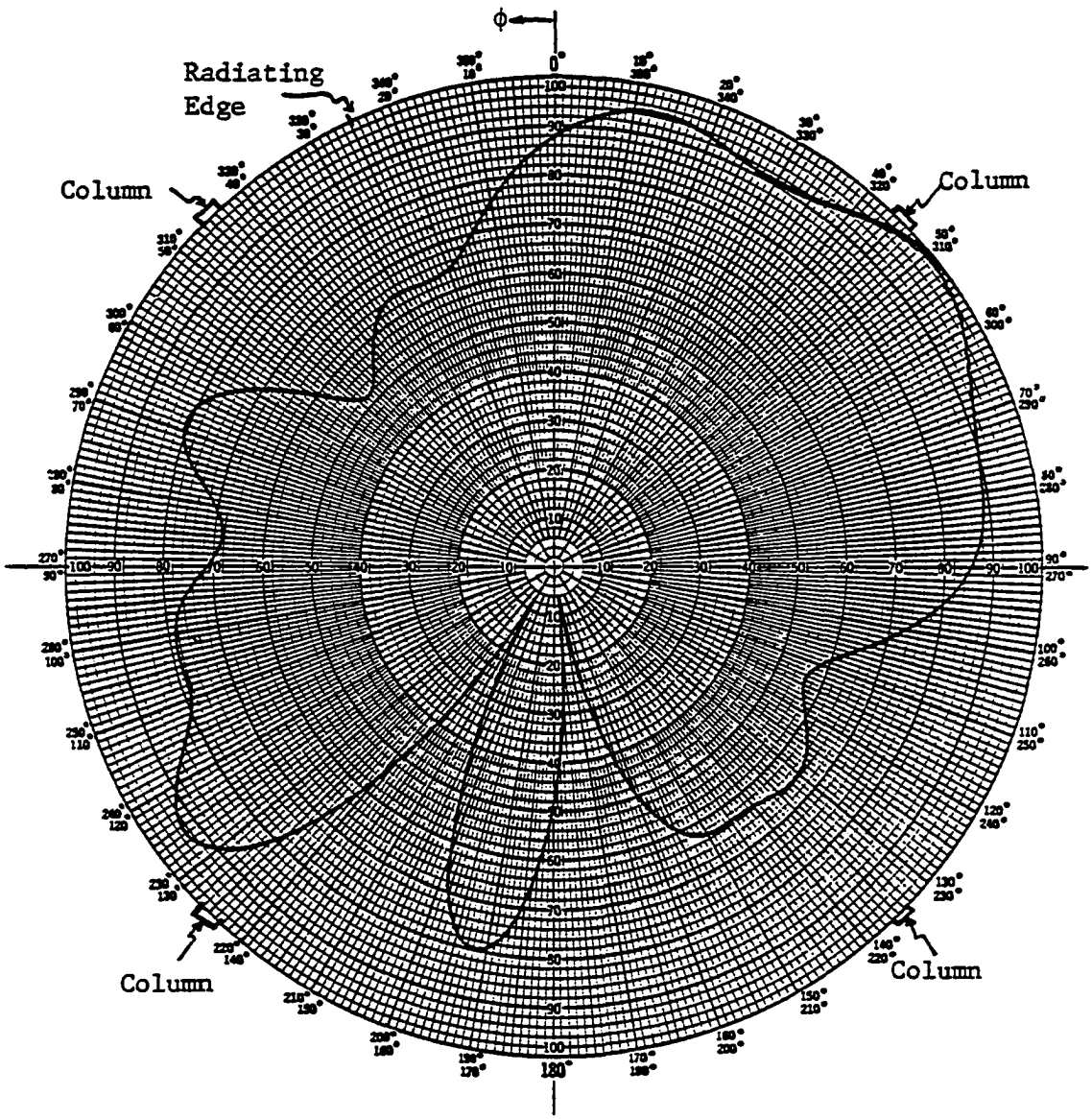

Fig. 5-4. Experimental far-field radiation pattern of a smooth conducting cylinder with one microstrip antenna panel with radiating edge at $\phi = 25^0$ and four equally-spaced columns

Comparing these two patterns (Figs. 5-2 and 5-4) shows that there is not much difference between the patterns, which agrees very well with the theoretical results. The asymmetry of the patterns is attributed partially to the set-up and partially to the shape of the microstrip panel; it has nothing to do with the presence of the columns.

To study the effect of microstrip panel structure external to the cylinder and very close to the radiating aperture, the microstrip panel was replaced by a slot antenna mounted directly on the cylindrical surface with no structure external to the cylinder. Figs. 5-5 and 5-6 show this model, with and without columns.

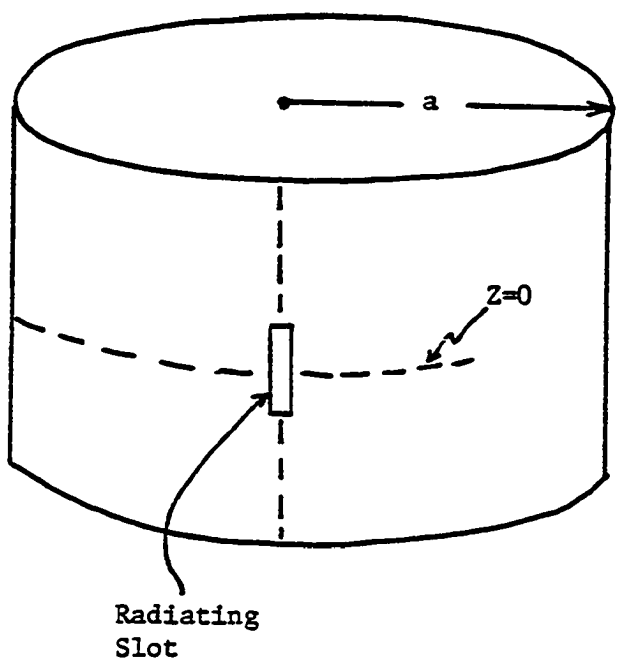

Fig. 5-5. Smooth conducting cylinder with a radiating slot at $\phi = 0^0$

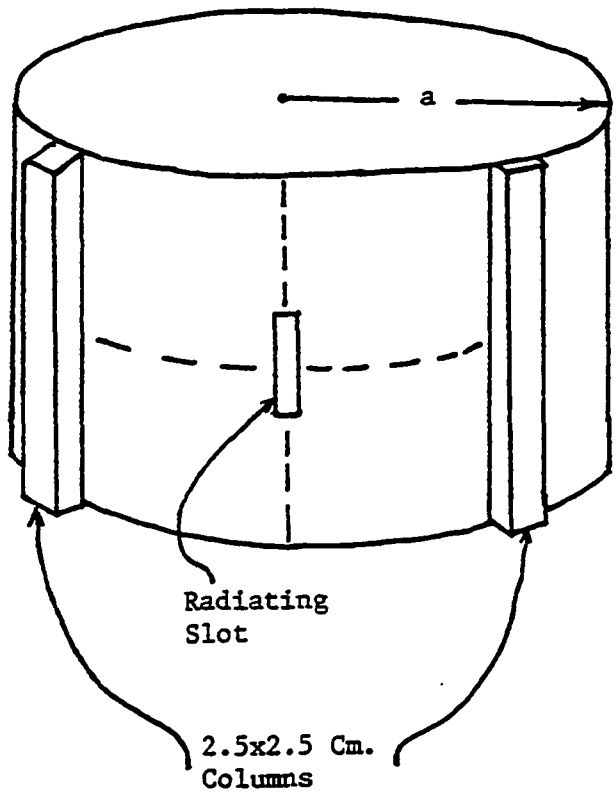

Fig. 5-6. Slotted cylinder with four columns of 2.5 x 2.5 Cm. equally-spaced and symmetrical with respect with the slot at $\phi = 0^0$

Figs. 5-7 and 5-8 show the corresponding far-field radiation patterns of these two set-ups. Comparing these two patterns again shows that the effect of the columns is almost negligible, also in agreement with the theoretical results. Both patterns exhibit some non-symmetry, even though both models are physically symmetrical. The reason for this is not clear, but it is attributed to details of the model construction and scattering in the anechoic chamber. The important point, however, is

evident from a comparison of Fig. 5-7 with Fig. 5-2: namely, the structure of the microstrip panel itself on the outside of the cylinder appears to have a much larger effect on the pattern than had been realized earlier. The analytical model, of course, could not predict this effect.

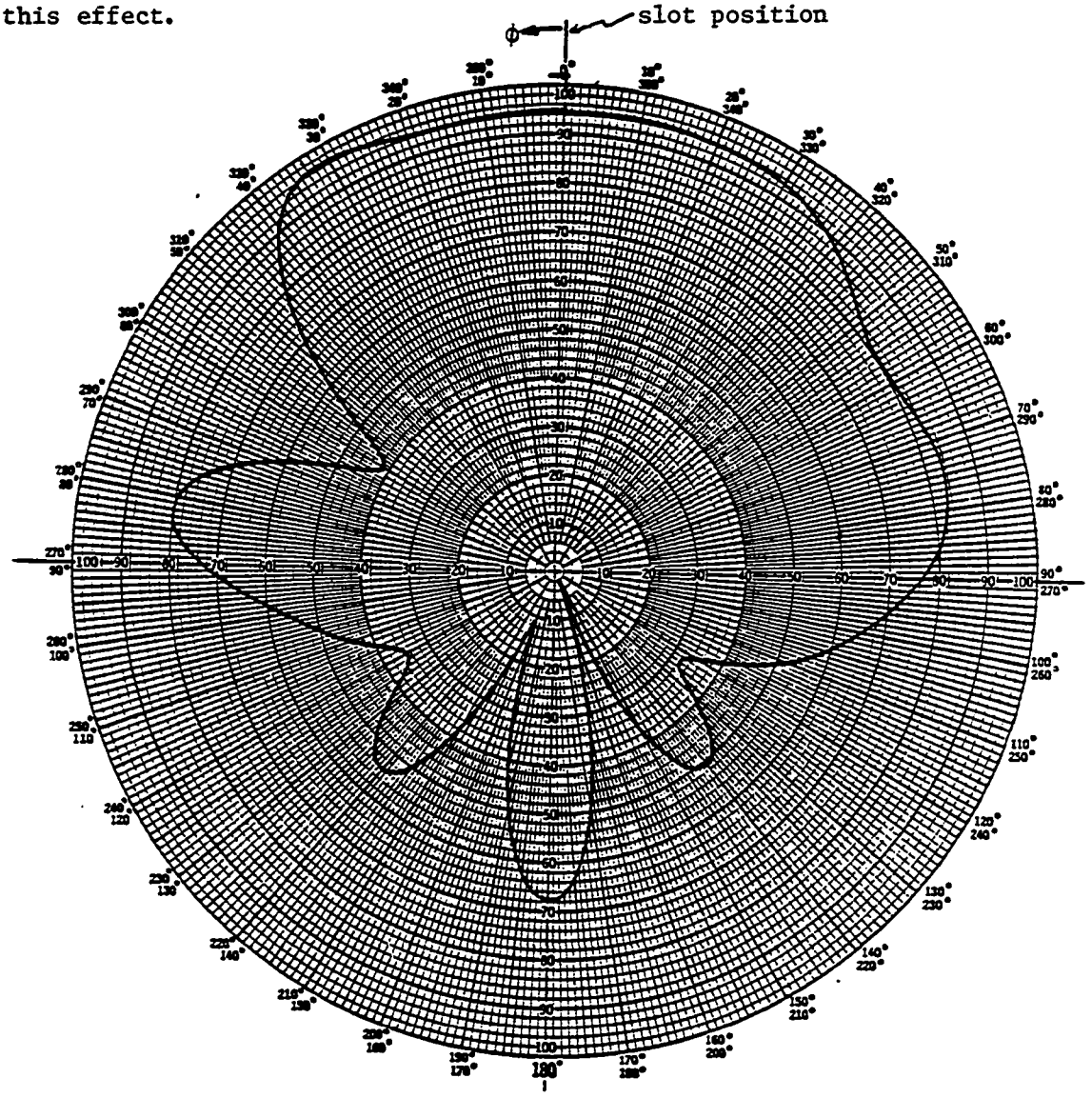

Fig. 5-7. Experimental far-field radiation pattern of a slotted cylinder

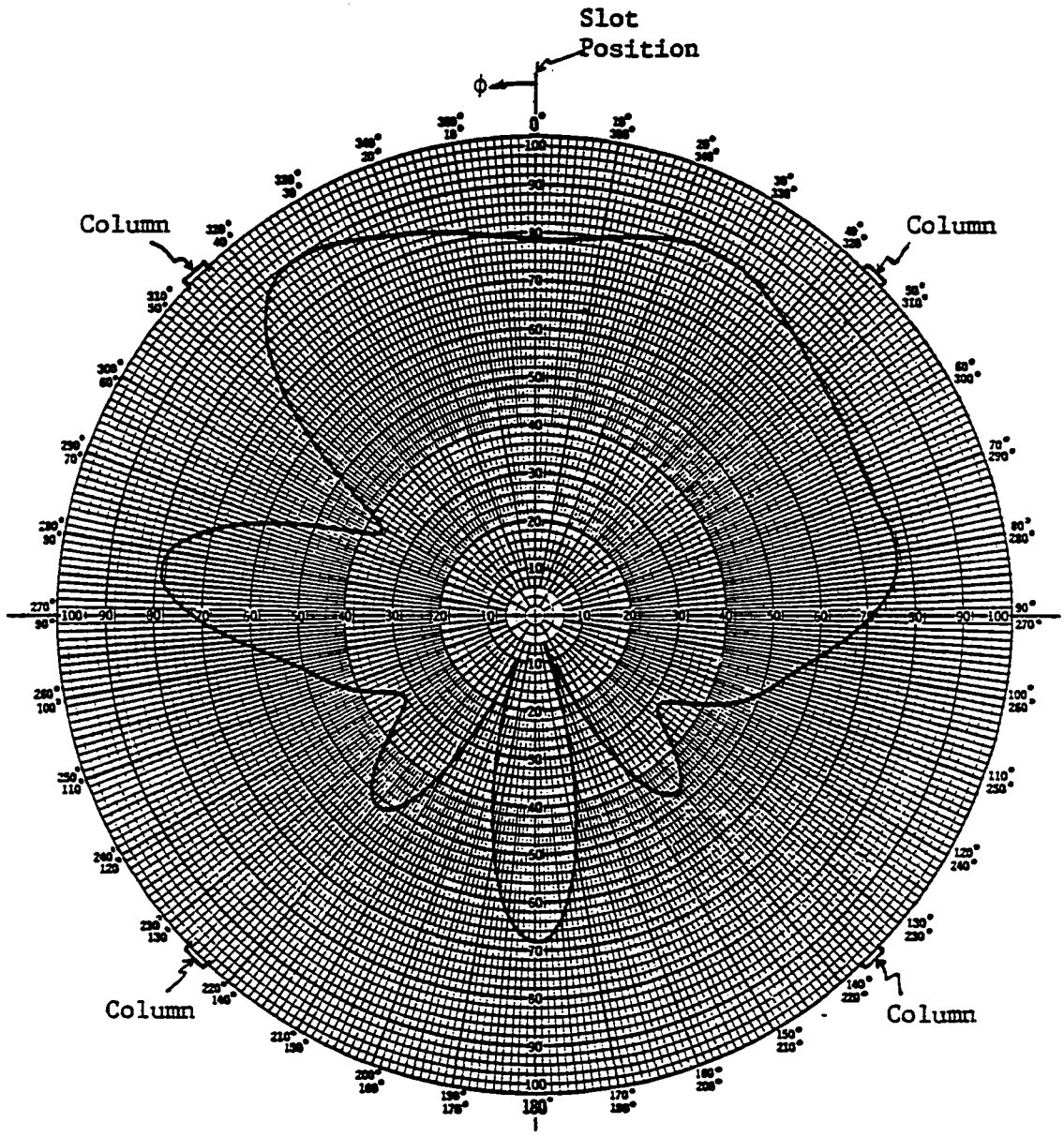

Fig. 5-8. Experimental far-field radiation pattern of a slotted cylinder with four equally-spaced columns

Finally, the last laboratory measurement was devoted to the slotted cylinder with a column positioned at about $\phi = 8^0$. This specific position was chosen from the near-field pattern of Fig. 4-8 as mentioned in the previous section (positioning a column at the location of a maximum of $|E_\rho(\phi)|$ will have the most effect on the far-field pattern). Fig. 5-9 shows the far-field radiation pattern of this last configuration. Comparing Fig. 5-9 with 5-7, the effect of the columns is visible and can be measured. Absolute amplitude differences in these patterns are not significant; they are relative field intensity patterns only. The presence of the column at $\phi = 8^0$ alters the symmetry of the pattern, as predicted by the analysis, and shifts the angle of the back lobe by about 5°. Once again, the experimental and theoretical results agree very well.

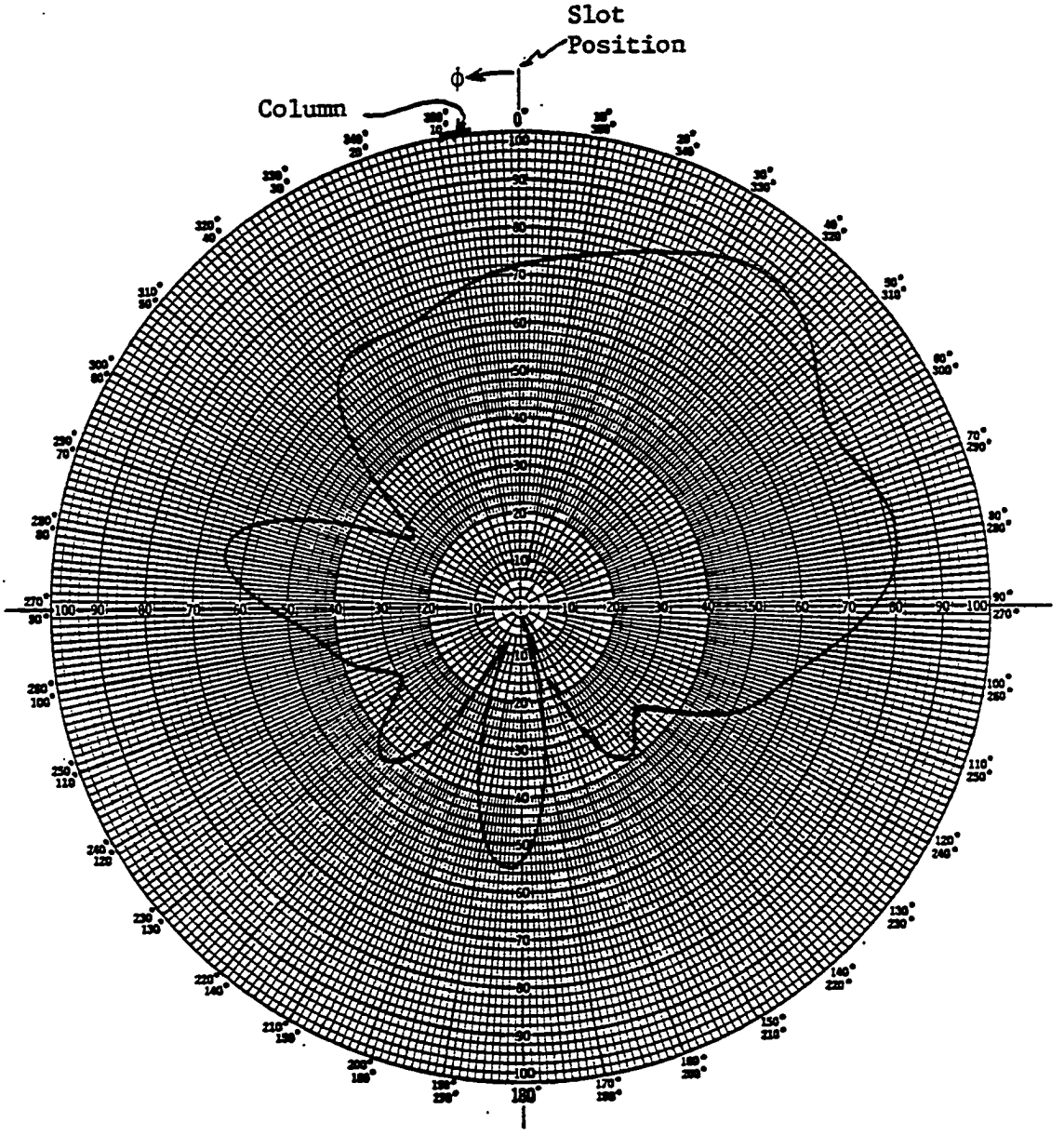

Fig. 5-9. Experimental far-field radiation pattern of a slotted cylinder with a column at $\phi = 8.6^0$

VI. USING THE MODIFIED NEC FOR THE PDP PROBLEM

The NEC program uses both an electrical-field, integral equation (EFIE) and a magnetic-field integral equation (MFIE) to model the electromagnetic response of general structures. The EFIE is well suited for thin-wire (wire grid model) structures which are defined as open bodies, while the MFIE must be used for voluminous structures which have smooth surfaces (surface patch model). The EFIE (wire grid model), however, can be used on open and/or closed bodies. For a structure containing both wires and surfaces, a combination of EFIE and MFIE can be applied using the principle of superposition (4).

Both models were investigated for the PDP and the details of each examination are given in the following sections.

A. Investigation of Wire Grid Model on the PDP

Modeling a structure with wire grid segments involves both geometrical and electrical factors. Geometrically, the segments should follow the paths of conductors as closely as possible. Electrically, the main consideration is segment length relative to the wavelength. For reasonable accuracy, the maximum length of a segment should be less than about 0.1λ at the desired frequency.

The frequency used for the PDP is 400.6 MHz, with a corresponding wavelength of about 0.75m. Therefore, the maximum length of each segment cannot exceed 0.075m or 7.5cm.

Considering Fig. 1-1 (PDP dimensions), to model this with limitation

of the wire grid model, a minimum of at least 1200 segments would be needed.

The NEC can handle a maximum of 300 segments or patches. A considerable amount of time and work were devoted to expand the capacity of modified NEC from 300 to at least 900, but the attempts were not successful.

As a result, costs prohibited the use of this modeling approach, and the wire-grid method was discontinued.

B. Investigation on the PDP of Surface Patch Model

A conducting surface is modeled by means of multiple, small flat surface patches. The patches are chosen to completely cover the surface to be modeled.

The program computes the surface current on each patch along the orthogonal unit vectors $\overline{t_1}$ and $\overline{t_2}$, which are tangent to the surface as seen in Fig. 6-1.

In general $\bar{t}_1$ and $\bar{t}_2$ can be determined as follows:

$$\bar{t}_1 = (\bar{z}\bar{x}\bar{n})/|\bar{z}\bar{x}\bar{n}|$$

$$\bar{t}_2 = \bar{n}\bar{x}\bar{t}_1$$

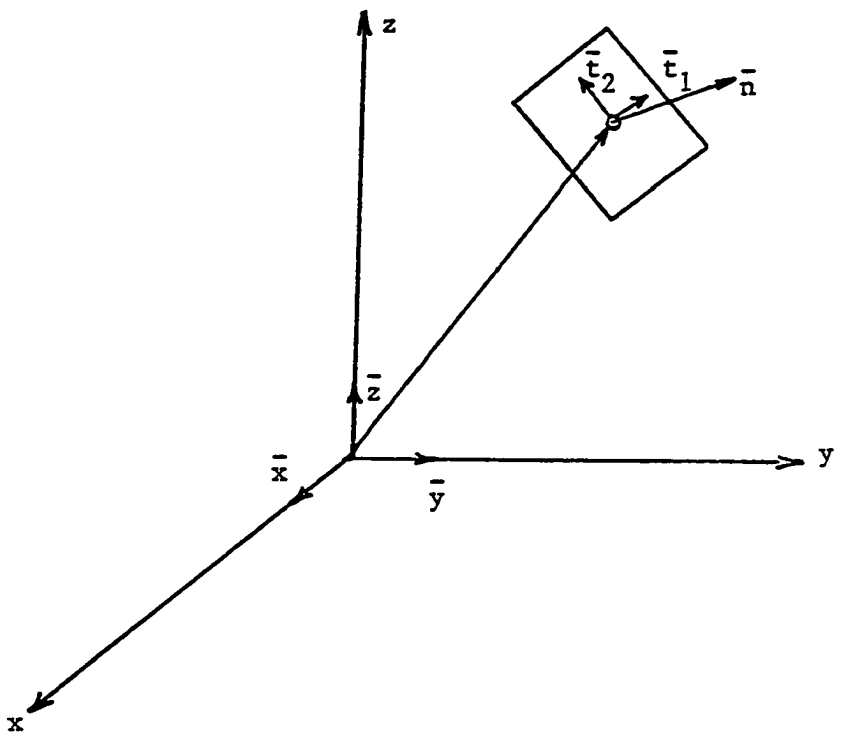

Fig. 6-1. Patch position and orientation

As with wire modeling, patch size measured in wavelengths is very important for accurate results. A minimum of about 25 patches should be used per square wavelength of surface area, with the maximum size for an individual patch about 0.04 square wavelengths. However, smaller patches are recommended for use on curved surfaces, both for geometrical modeling accuracy and for accuracy of the integral equation solution.

Again considering Fig. 1-1 (PDP dimension), to model this with the above restrictions, the number of the patches for a good model were about 300 for the smooth cylinder without columns. But to model the complete body of the PDP, columns must somehow be modeled. No matter which modeling is used for the columns, the total number of patches or patches and segments will again exceed 300. Using a combination of patches and segments, and accepting a small loss in accuracy, it was possible to use the modified NEC with some patch areas slightly larger than the above limits, to investigate the effect of the columns on the PDP radiation pattern.

C. Resultant Modeling of the PDP

Surface patch modeling is the only choice to model the body of the PDP in order to use the modified NEC to analyze the effect of the columns. But the columns must also be modeled as either patches or segments. Since the cross-section of the columns is only 5x5cm and the NEC recommends that long narrow structures be avoided, surface patch modeling for the columns is not attractive. Therefore, the columns were modeled as a number of short monopoles, each one connected to the center of one of the patches.

1. Modeling the smooth cyclinder

One of the structure generation capabilities of NEC is to produce a structure while rotating about the z-axis to form a complete cylindrical array and set up the program so that symmetry is utilized in the solution. Therefore, to produce the body of the PDP by this method,

coordinates of the center of patches for a small section of the cylinder must be given to the program, and then the program will rotate this section as many times as necessary to complete the cylinder. It was then discovered that the program required cylindrical segments at least 18° in width, so that 16 segments at most are used.

Two other structure generation capabilities utilized are: a) translation or rotation of a structure to generate new structures from the original, and b) to form structures having planes of symmetry by reflecting part of the structure in the coordinate planes, and to set up the program so that symmetry is utilized in the solution.

A combination of these capabilities were then used to model the PDP body and fences as follows:

1. A section of 11.25° of cylinder covered by 7 patches was chosen, as in Fig. 6-2.
2. The coordinate center of these patches were given to the program.
3. This section was rotated first 11.25°, then 22.5° and finally 45° to complete a quadrant of the cylinder.
4. This first quadrant was reflected along the x-axis (reflection in yz-plane) and then the whole structure was reflected along the y-axis to complete the body of the PDP.

Note: When reflection is used to generate a structure, the vectors $\overline{t}_1$, $\overline{t}_2$ and $\overline{n}$ (see Fig. 6-1) are also reflected so that the new patches will have $\overline{t}_2 = -\overline{n} \times \overline{t}_1$. This point was critical in achieving the correct field patterns, and is accounted for in NEC.

2. Modeling the columns

As mentioned before, the best way to model the columns without violating the area requirement and exceeding the number limitation is to put a set of monopoles on the center of the patches at the desired angles. The desired angles must be chosen from the center of the side patches. Fig. 6-2 shows that a maximum of 5 monopoles could be connected to the 5 patches at the angle that connects the center of these patches to the origin. Fig. 6-3 demonstrates this configuration.

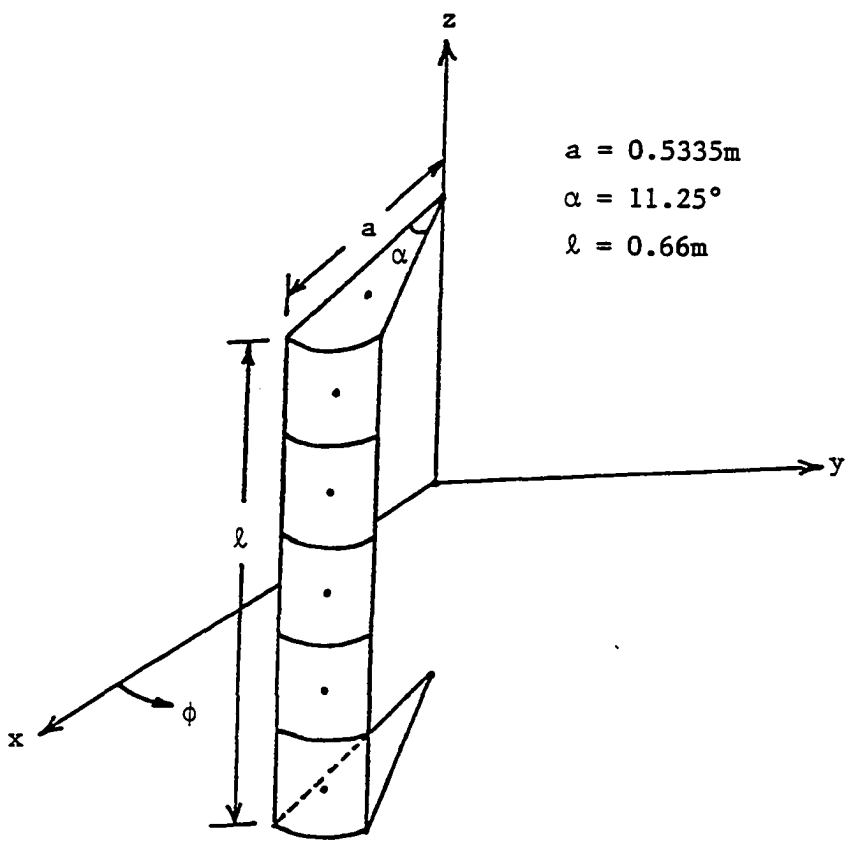

Fig. 6-2. Development of surface model for PDP

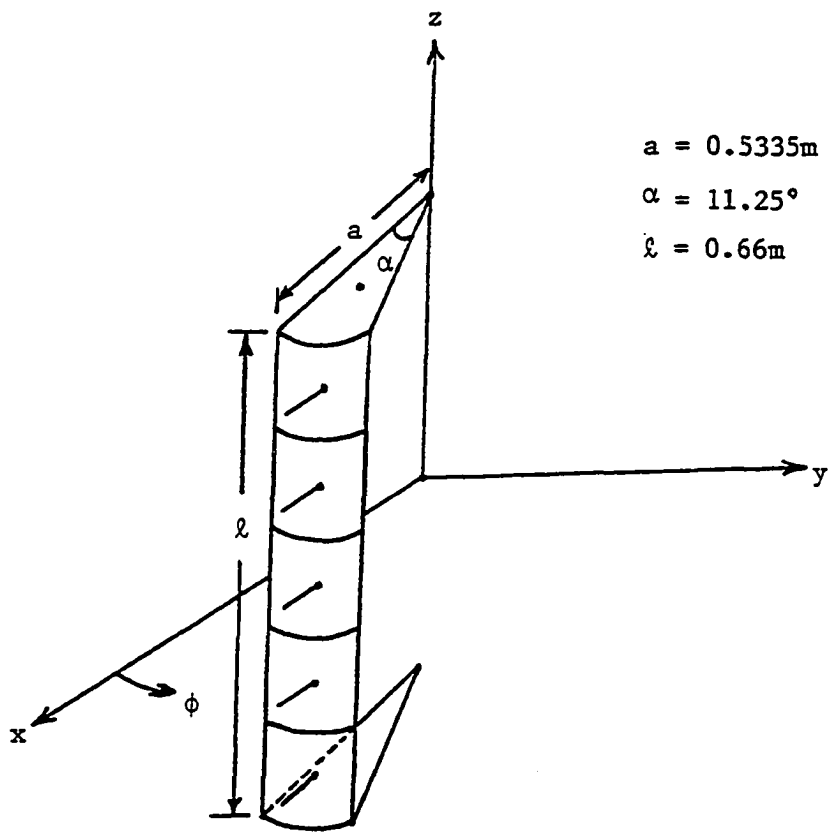

Fig. 6-3. Positioning of the monopoles on the center of patches at $\phi = 5.625^0$

D. Far-Field Pattern of the PDP

The modified NEC was used to find the radiation pattern of the PDP without columns and also with columns.

1. Radiation pattern of PDP without columns

The radiation pattern of the PDP without columns using the modified NEC was determined by using the complete model of Fig. 6-2. The position of the extended magnetic source (dual of slot) for this sum was at $\phi = 0^0$. Fig. 6-4 shows this pattern.

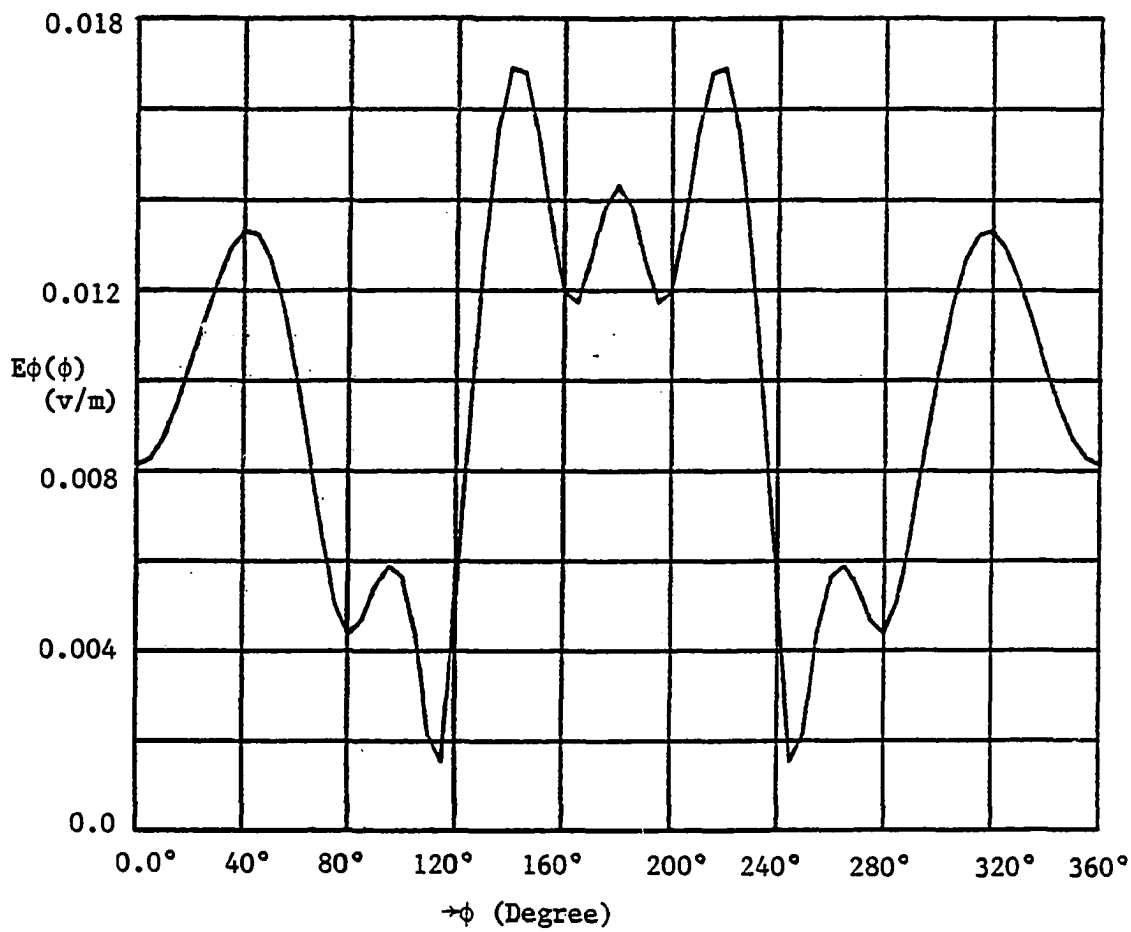

Fig. 6-4. Radiation pattern of the PDP with source at $\phi = 0.0^0$, and without fences

Comparing the pattern in Fig. 6-4 with analytical and experimental patterns (Figs. 4-3 and 5-7), differences can be seen. The most significant differences are nulls at about 180° which are not as deep as they are in the patterns of the earlier chapter, and the magnitudes at 140° and 220° are greater than those at 40° and 320°. These differences could be because of the following reasons: a) The NEC originally was written for a CDC 7600 computer where calculations used up to 16 digits. The IBM computer uses only up to 7 digits (single precision) due to complexity. This could have a big effect on the numerical results. For example in order to get a deep null, amplitudes at that specific point must be exactly the same with 180° phase difference. Slight numerical errors which cause these two magnitudes to be unequal will cause the filling of the corresponding null. b) As mentioned earlier in the chapter, to use modified NEC for PDP size, the area of some of the patches (top and bottom) exceeded the $0.04\lambda^2$ limitations. This could result in numerical errors as well, but this effect probably isn't large since the components of the far-field due to these patches are small.

In summary, the shape of the overall pattern follows the analytical and experimental patterns.

Another pattern was taken from the same model geometry, but with source located at $\phi = 33.75^0$. This pattern is shown in Fig. 6-5. It is quite symmetrical, and differs from Fig. 6-4 primarily in a shift of 33.75° in ϕ.

2. Far-field radiation pattern with columns

The same model was used, with the addition of a fence at $\phi = 39.375^0$ which will result in a total of four fences. The position of the other three fences dictated by NEC symmetry requirements, are at $\phi = 129.3751$, $\phi = 230.625^0$, and at $\phi = 320.625^0$. Two runs were made, with one for the source at $\phi = 0.0$ corresponding to a separation angle between fence and source of about 39.375°. The resulting pattern is shown in Fig. 6-6.

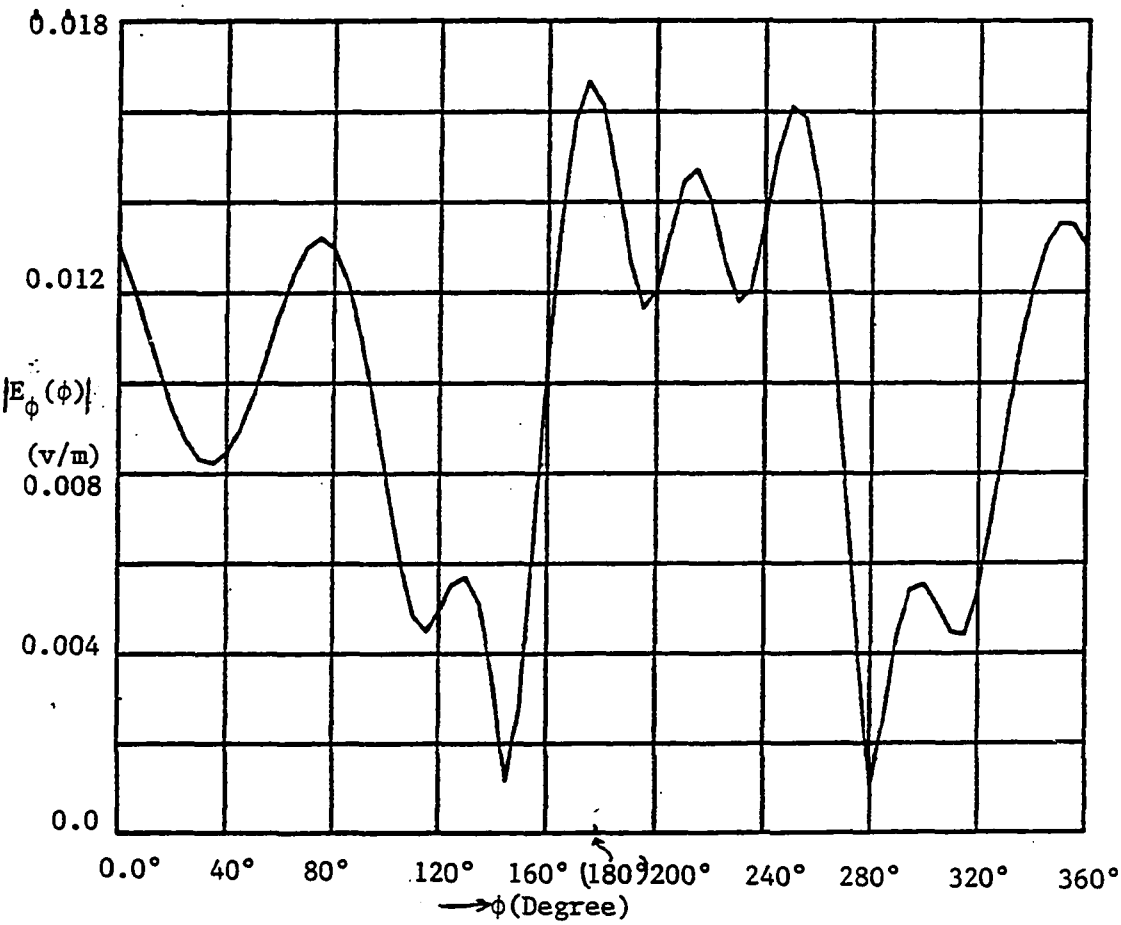

Fig. 6-5. Radiation pattern of the PDP with souce at $\phi = 33.75^0$, and without fences

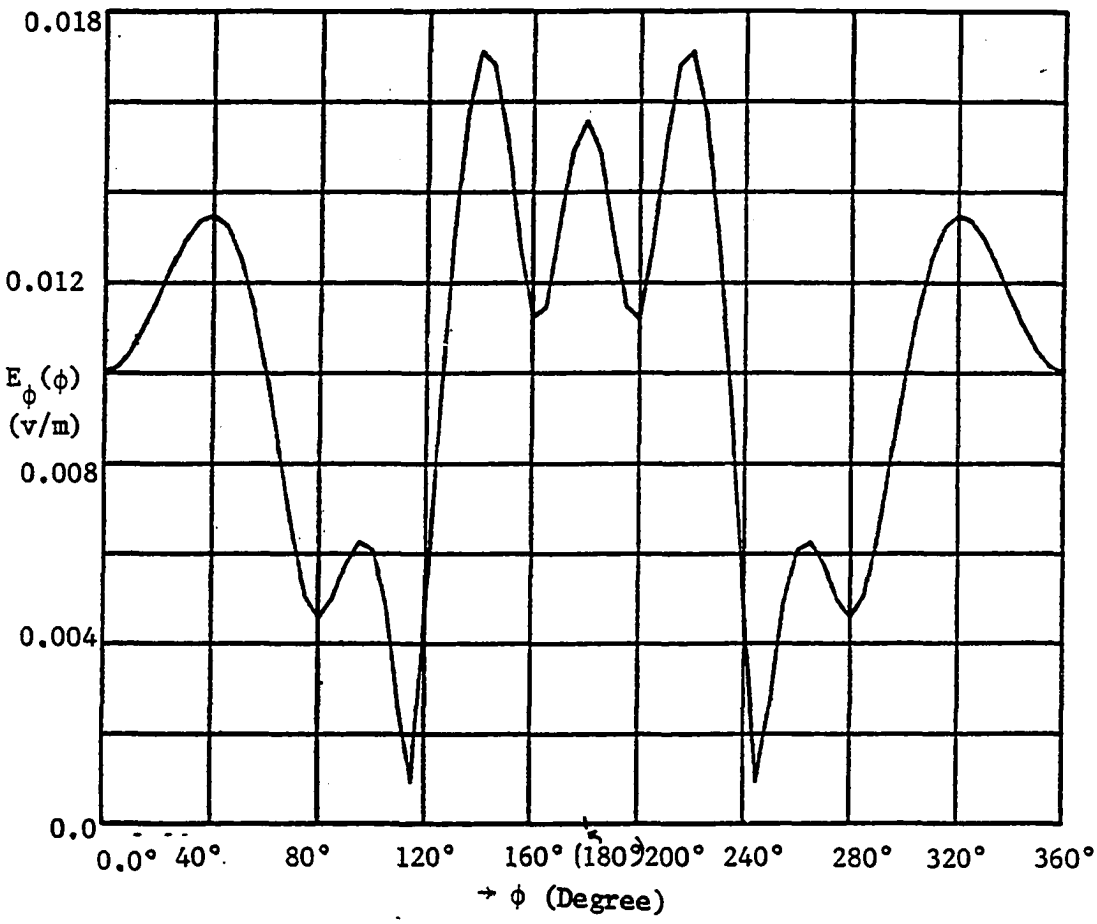

Fig. 6-6. Radiation pattern of the pDP with fences located at $\phi = 39.375^0$, 129.375^0, 230.625^0, 320.625^0, and source located at $\phi = 0.0^0$

Comparing Fig. 6-6 with Fig. 6-4, there is not a significant difference, as expected, showing the NEC agreement with both theoretical and experimental results. Another run was for the same fence positions but with the source located at ϕ = 33.75 (which makes a separation angle between source and fence of about 5.625°). The pattern of this run is shown in Fig. 6-7. Comparing this pattern with Fig. 6-5, we find as expected, a significant difference between these two patterns. The presence of the fences is visible - the symmetry of the pattern is destroyed around 180°. This agrees again with analytical and experimental results. In conclusion, therefore, we find that despite the numerical approximations made in setting up this model it is still capable of displaying small differences caused by the columns.

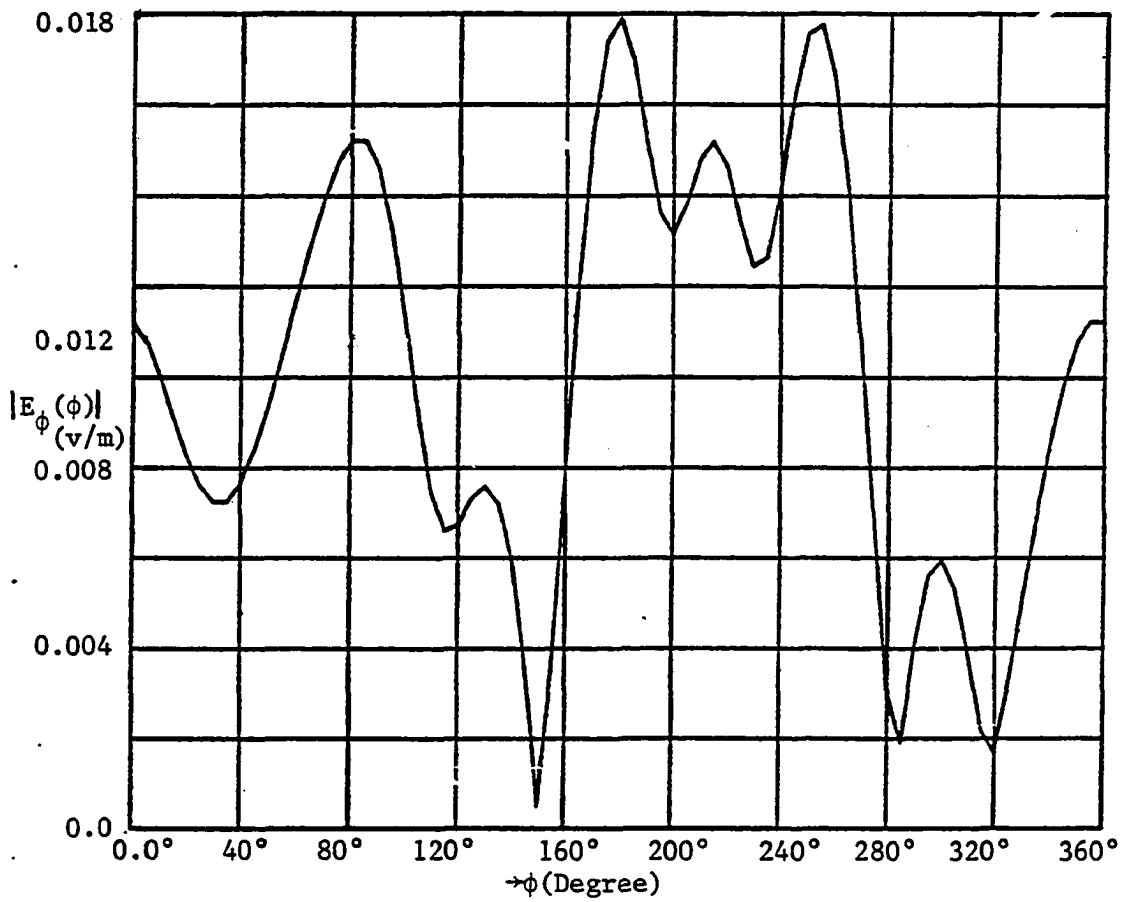

Fig. 6-7. Radiation pattern of the PDP with fences located at ϕ - 39.375^0, 129.375^0, 230.625^0, 320.625^0, and source located at $\phi = 33.75^0$

VII. CONCLUSION AND RECOMMENDATIONS

This work is a study of microstrip antennas on a conducting cylinder with the presence of columns on the surface of the cylinder. Three different methods have been used to study the effect of these columns on the far-field radiation pattern. The first method was an analytical approach. Studying the near and far-fields of this structure enabled us to determine the sensitivity of the far-field radiation pattern with respect to the positioning of these axial columns around the cylinder.

The near-field analysis of the slotted conducting cylinder provided the following:

1. The near-field pattern was obtained for an infinitely long cylinder of any radius. The computer program for this analysis is on file with the Department of Electrical and Computer Engineering at Iowa State University.

2. Computation of the near-field pattern permits us to study the sensitivity of the far-field pattern with respect to the positions of the columns mounted on the cylinder, and to predict the currents induced on the columns. This has been verified by positioning of the columns at different locations on the cylinder.

3. The total radiation pattern due to a slot antenna in the presence of arbitrarily positioned columns can be easily determined.

The analysis outlined above has provided an interesting observation of the effect of column positioning on the total radiation pattern. The near-field study shows that some standing waves are set up around the conducting cylinder, with nulls occurring at the various locations as a function of wavelength, cylinder radius, and the number of radiating slots. The far-field pattern calculations indicate the effects of axial columns mounted on the cylinder. It has been found that if the columns are placed at the ϕ-positions corresponding to low values of $|E_\rho(\rho,\phi,z)|$ the far-field pattern is least affected. Conversely, it was found that if the columns are placed at the ϕ-positions corresponding to the highest magnitude of $E_\rho(a,\phi,z)$, the far-field pattern is most affected. In this method, the cylinder was assumed to be infinitely long. Therefore, the results could be slightly different if a cylinder with finite length was used. This should be considered when the results are applied to the PDP configuration.

The second method was an experimental analysis. The PDP was scaled to half-size for practical purposes, and the operating frequency was correspondingly doubled. Here also, some approximations were necessary. The pattern measurements included two probable sources of error: the anechoic chamber was not ideal, and there was some aluminum tapes on the conducting cylinder which were not perfectly conducting.

The overall measured patterns followed the analytical results, and

they confirmed the prediction of fence positioning from the near-field information.

The third method was numerical, using a modified NEC method of moments. The PDP with columns was modeled in a way that could be handled by the modified NEC program. Here again there were some adjustments in order to meet the NEC requirements and limitations. These adjustments should be kept in mind when evaluating the NEC output.

Nevertheless, the NEC patterns were basically found to be in agreement with the analytical and experimental results.

The above summary brings us to the following conclusion. Although there were some inaccuracies in each of these methods, all three methods were correlated, and all together provide the same conclusion about the effect of the fences on the far-field radiation pattern. All three methods qualitatively verified the sensitivity of the pattern to the positions of the columns according to the near-field information. A specific conclusion is that effects on the far-field patterns which were previously attributed to the columns are now found to be caused by other factors; e.g., the presence of the microstrip antenna structure external to the cylinder and very close to the radiating aperture.

Therefore, this work has provided us with the ability to predict the radiation pattern of a slotted conducting cylinder with axial columns, and further, to design suitable configurations of this structure to meet various design specifications.

Further study could be done by slightly modifying these methods to find the effect of any obstacle on the cylinder, even with a

circumferential slot on the cylinder. As a result, this study could be the basis for a large amount of research work in this area, and also in other related areas (e.g., slotted arrays on cylindrical surfaces). The author hopes that this study will be of great benefit in this regard.

VIII. BIBLIOGRAPHY

1. Bacg, H., P. J. B. Clarricoats, J. B. Davies, A. T. de Hoop, L. B. Felsen, R. Mittra, H. G. Unger, and J. Van Bladel. 1976. Modern topics in electromagnetics and antennas. PPL conference publication 13.

2. Bailin, L. L. 1955. The radiation field produced by a slot in a large circular cylinder. IRE Transactions on Antennas Propagation AP-3: 129-137.

3. Balanis, C. A. 1969. Analysis of aparture radiation from an axially slotted circular conducting cylinder using geometrical theory of diffraction. IEEE Transactions Antennas Propagation AP-17: 93-96.

4. Burke, G. J., and A. J. Pogio. 1981. Numerical electromagnetics code (NEC) - method of moments. Lawrence Livermore Laboratory, Livermore, CA.

5. Burnside, W. D., C. L. Yu, and R. J. Marhefka. 1975. A technique to combine the geometrical theory of diffraction and method of moment. IEEE Transactions Antennas Propagation AP-23: 551-558.

6. Chen, Kun-Mu, D. E. Liversay, and B. S. Guru. 1976. Induced current in and scattered field from a finite cylinder with arbitrary conductivity and permitivity. IEEE Transactions Antennas Propagation AP-24: 330-336.

7. Davis, W. A. 1977. A new approach to the thin scatterer problem using the hybrid equations. IEEE Transactions Antennas Propagation AP-25: 402-406.

8. Derneryd, A. G. 1976. Linearly polarized microstrip antennas. IEEE Transactions Antennas Propagation AP-24: 847-851.

9. Harrington, R. F. 1968. Field Computation by moment methods. Macmillan, New York.

10. Harrington, R. F. 1961. Time-Harmonic electromagnetic fields. McGraw-Hill, Inc., New York.

11. James, G. L. 1977. Geometrical theory of diffraction for electromagnetic waves. Research Scientist Division of Radiophysics, CSIRO, Sydney, Australia, 1976.

12. Jedlicka, R. P., and K. R. Carver. ca. 1978. Mutual coupling between microstrip antennas. Physical Science Laboratory, New Mexico State University, Las Cruces, New Mexico.

13. Jedlicka, R. P., M. T. Poe, and K. R. Carver. 1981. Measured mutual coupling between microstrip antenna. IEEE Transactions Antennas Propagation AP-29: 147-149.

14. Jordan, C. Edward, and Keith G. Balmain. 1968. Electromagnetic waves and radiating systems. Prentice-Hall, Inc., Englewood Cliffs, New Jersey.

15. Keller, J. B. 1962. Geometrical theory of diffraction. Journal of the Optical Society of America 52: 116-130.

16. Lopez, A. R. 1966. The geometrical theory of diffraction applied to antenna and impedance calculations. IEEE Transactions Antennas Propagation AP-14: 40-45.

17. Newman, E. H., and D. M. Pozar. 1978. Electromagnetic modeling of composite wire and surface geometries. IEEE Transactions Antennas Propagation AP-26: 784-789.

18. Newman, E. H., and P. Tulyathan. 1981. Analysis of microstrip antennas using moment methods. IEEE Transactions Antennas Propagation AP-29: 47-53.

19. Newman, E. H., and P. Tulyathan. ca. 1978. Microstrip analysis technique. The Ohio State University, Electroscience Laboratory, Columbus, Ohio.

20. Pathak, P. H. 1974. An analysis of the radiation from apertures in curved surfaces by the geometrical theory of diffraction. Proc. IEEE 62: 1438-1447.

21. Post, R. E., and D. T. Stephenson. 1981. The design of a microstrip antenna array for a UHF space telemetry link. IEEE Transactions Antennas Propagation AP-29: 129-134.

22. Pozar, D. M. 1982. Input impedance and mutual coupling of rectangular mcrostrip antennas. IEEE Transactions Antennas Propagation AP-30: 1191-1196.

23. Richards, W. F., Y. T. Lo, and Harrison. 1981. An improved theory for microstrip antennas and applications. IEEE Transactions Antennas and Propagation AP-29: 38-46.

24. Richmond, J. H. 1966. A wire-grid model for scattering by conducting bodies. IEEE Transactions Antennas Propagation AP-14: 782-786.

25. Silver, S., and W. K. Saunders. 1950. The external field produced by a slot in an infinite circular cylinder. J. Appl. Phys. 21: 153-158.

26. Silver, S., and W. K. Saunders. 1950. The radiation from a stransverse rectangular slot in a circular cylinder. J. Appl. Phys. 21: 745-749.

27. Thiele, G. A., and T. H. Newhouse. 1975. A hybrid technique for combining method of moment with GTD. IEEE Transactions Antennas Propagation AP-23: 62-69.

28. Vogler, L. E. 1982. An attenuation function for multiple knife-edge diffraction. Radio Science 17: 1541-1546.

29. Wang, J. J. H. 1978. Numerical analysis of three-dimensional arbitrary-shaped conducting scatterers by trilateral surface cell modeling. Radio Science 13: 947-952.

30. Wilton D. R., S. S. M. Rao, and A. W. Glisson. 1979. Electromagnetic scattering by surfaces of arbitrary shape. Department of Electrical Engineering, University of Mississippi, University, Miss.

IX. ACKNOWLEDGEMENTS

I am indebted to Dr. D. T. Stephenson and Dr. R. E. Post, my major professors, for their guidance, technical assistances, many valuable suggestions, and their patience during the preparation of this manuscript. A very special thanks is due to Dr. Marvin S. Beck, for his wonderful guidance and his many valuable suggestions. Finally, I would especially like to thank my friend John F. Aurand, for his technical help and his willingness to help in the interpretation of references.

X. APPENDIX: CYLINDRICAL NEAR-FIELD DEVELOPMENT

This appendix contains the development of the near-field expressions for the cylindrical configuration considered in Chapter IV. Fig. 4-1 illustrates the physical arrangement of the model, and Fig. 4-2 shows the behavior of the electric field around the cylinder. Formulas for the near-field components of E(E_z, E_ϕ, and E_ρ) and for the magnetic field (H_z) are derived using Maxwell's equations and Fourier integrals.

Since the slot is intended to model a microstrip antenna with radiating edge parallel to the z direction, the excitations in the z and ϕ directions are:

$$E_z(a,\phi,z) = 0 \ ,$$

and $E_\phi(a,\phi,z)$ constant over the aperture.

The cylindrical transform of the aperture excitation

$$\bar{E}_\phi\ (n,w) = \frac{1}{2\pi} \int_0^{2\pi} d\phi \int_{-\infty}^{\infty} E_\phi\ (a,\phi,z)\ e^{-jn\phi}\ e^{jwz} dz, \qquad (10\text{-}1)$$

with a corresponding inverse transform of

$$E_\phi(a,\phi,z) = \frac{1}{2\pi} \sum_{n=-\infty}^{\infty} e^{jn\phi} \int_{-\infty}^{\infty} \bar{E}_\phi\ (n,w)\ e^{jwz} dw. \qquad (10\text{-}2)$$

Equation (10-2) is a Fourier series on ϕ and a Fourier integral on z.

The field external to the cylinder can be expressed as the sum of a TE component and a TM component. From Maxwell's equations,

$$\overline{E} = - \overline{\nabla} \times \overline{F} - j\omega\mu\overline{A} - \frac{1}{j\omega\varepsilon} \overline{\nabla} (\overline{\nabla} \cdot \overline{A}), \tag{10-3}$$

$$\overline{H} = \overline{\nabla} \times \overline{A} - j\omega\varepsilon\overline{F} + \frac{1}{j\omega\mu} \overline{\nabla} (\overline{\nabla} \cdot \overline{F}), \tag{10-4}$$

where:

$\overline{A} = \overline{i}_z A_z$ magnetic vector potential

$\overline{F} = \overline{i}_z F_z$ electric vector potential (10-5)

$\overline{i}_z$ is a unit vector in the z direction.

Constructing the wave functions A_z and F_z:

$$A_z = \frac{1}{2\pi} \sum_{n=-\infty}^{\infty} e^{jn\phi} \int_{-\infty}^{\infty} f_n(w) H_n^{(2)}\left(\rho \sqrt{k^2-w^2}\right) e^{jwz} dw, \tag{10-6}$$

$$F_z = \frac{1}{2\pi} \sum_{n=-\infty}^{\infty} e^{jn\phi} \int_{-\infty}^{\infty} g_n(w) H_n^{(2)}\left(\rho \sqrt{k^2-w^2}\right) e^{jwz} dw, \tag{10-7}$$

where $H_n^{(2)}$ is the Hankel function of the second kind.

The following procedure is uded to calculate the $\overline{E}$ and $\overline{H}$ fields. For $\overline{E}(\rho, \phi, z)$, we begin with equation (10-3).

$$\overline{E} = - \overline{\nabla} \times \overline{F} - j\omega\mu\overline{A} + \frac{1}{j\omega\varepsilon} \overline{\nabla}\,\overline{\nabla}\,\overline{A} ,$$

$$\overline{\nabla} \times \overline{F} = \frac{1}{\rho} \left(\frac{\partial F_z}{\partial \phi}\right) \hat{a}_\rho - \left(\frac{\partial F_z}{\partial \rho}\right) \hat{a}\phi ,$$

$$\overline{\nabla} \cdot \overline{A} = \frac{\partial A_z}{\partial z}, \text{ and } \overline{\nabla}S = \frac{\partial S}{\partial \rho} \hat{a}_\rho + \frac{1}{\rho} \frac{\partial S}{\partial \phi} \hat{a}_\phi + \frac{\partial S}{\partial z} \hat{a}_z ,$$

$$\overline{\nabla}(\overline{\nabla}\cdot\overline{A}) = \frac{\partial}{\partial \rho} \left(\frac{\partial A_z}{\partial z}\right) \hat{a}_\rho + \frac{1}{\rho} \frac{\partial}{\partial \phi} \left(\frac{\partial A_z}{\partial z}\right) \hat{a}_\phi + \frac{\partial}{\partial z} \left(\frac{\partial A_z}{\partial z}\right) \hat{a}_z$$

$$= \frac{\partial^2 A_z}{\partial \rho \partial z} \hat{a}\rho + \frac{1}{\rho} \frac{\partial^2 A_z}{\partial \phi \partial z} \hat{a}_\phi + \frac{\partial^2 A_z}{\partial z^2} \hat{a}_z .$$

Substituting the preceding quantities into (10-3), we obtain

$$\bar{E} = -\frac{1}{\rho}\left(\frac{\partial F_z}{\partial \phi}\right)\hat{a}_\rho + \left(\frac{\partial F_z}{\partial \rho}\right)\hat{a}_\phi - j\omega\mu A_z\,\hat{a}_z +$$

$$\frac{1}{j\omega\varepsilon}\left(\frac{\partial^2 A_z}{\partial\rho\partial z}\right)\hat{a}_\rho + \frac{1}{\rho}\frac{\partial^2 A_z}{\partial\phi\partial z}\hat{a}_\phi + \frac{\partial^2 A_z}{\partial z^2}\hat{a}_z\Big) .$$

The following expressions are needed to complete the derivation.

$$\frac{\partial A_z}{\partial z} = \frac{1}{2\pi}\sum_{n=-\infty}^{\infty} e^{jn\phi}\int_{-\infty}^{\infty} f_n(w)\, H_n^{(2)}\left(\rho\sqrt{k^2-w^2}\right) jwe^{jwz}dw ,$$

$$\frac{\partial^2 A_z}{\partial z^2} = \frac{1}{2\pi}\sum_{n=-\infty}^{\infty} e^{jn\phi}\int_{-\infty}^{\infty} f_n(w)\, H_n^{(2)}\left(\rho\sqrt{k^2-w^2}\right)\left(-w^2 e^{jwz}\right)dw .$$

$$\frac{\partial^2 A_z}{\partial\phi\partial z} = \frac{1}{2\pi}\sum_{n=-\infty}^{\infty} -ne^{jn\phi}\int_{-\infty}^{\infty} f_n(w)\, H_n^{(2)}\left(\rho\sqrt{k^2-w^2}\right) we^{jwz}dw.$$

$$\frac{\partial^2 A_z}{\partial\rho\partial z} = \frac{1}{2\pi}\sum_{n=-\infty}^{\infty} e^{jn\phi}\int_{-\infty}^{\infty} f_n(w)\sqrt{k^2-w^2}\; H_n^{(2)'}\left(\rho\sqrt{k^2-w^2}\right)jwe^{jwz}dw.$$

$$\frac{\partial F_z}{\partial \phi} = \frac{1}{2\pi} \sum_{n=-\infty}^{\infty} jne^{jn\phi} \int_{-\infty}^{\infty} g_n(w)\, H_n^{(2)}\left(\rho\sqrt{k^2-w^2}\right)e^{jwz}dw.$$

$$\frac{\partial F_z}{\partial \rho} = \frac{1}{2\pi} \sum_{n=-\infty}^{\infty} e^{jn\phi} \int_{-\infty}^{\infty} g_n(w)\sqrt{k^2-w^2}\, H_n^{(2)'}\left(\rho\sqrt{k^2-w^2}\right)e^{jwz}dw.$$

Therefore the components of $\bar{E}$ are:

$$E_z(\rho,\phi,z) = \frac{1}{2\pi j\omega\varepsilon} \sum_{n=-\infty}^{\infty} e^{jn\phi} \int_{-\infty}^{\infty} (k^2-w^2)\, f_n(w) H_n^{(2)}\left(\rho\sqrt{k^2-w^2}\right)e^{jwz}dw. \tag{10-8}$$

$$E_\phi(\rho,\phi,z) = \frac{1}{2\pi} \sum_{n=-\infty}^{\infty} e^{jn\phi} \int_{-\infty}^{\infty} \left[\frac{-nw}{j\omega\varepsilon\rho} f_n(w) H_n^{(2)}\left(\rho\sqrt{k^2-w^2}\right)\right.$$

$$\left. + g_n(w)\sqrt{k^2-w^2}\, H_n^{(2)'}\left(\rho\sqrt{k^2-w^2}\right)\right] e^{jwz}\, dw. \tag{10-9}$$

and

$$E_\rho = -\frac{1}{\rho}\frac{\partial F_z}{\partial \phi} + \frac{1}{j\omega\varepsilon}\frac{\partial^2 A_z}{\partial \rho \partial z}$$

$$= \frac{1}{2\pi\rho}\sum_{n=-\infty}^{\infty} jne^{jn\phi}\int_{-\infty}^{\infty} g_n(w)H_n^{(2)}\left(\rho\sqrt{k^2-w^2}\right)e^{jwz}dw$$

$$+ \frac{1}{2\pi j\omega\varepsilon}\sum_{n=-\infty}^{\infty} e^{jn\phi}\int_{-\infty}^{\infty} f_n(w)\sqrt{k^2-w^2}\,H_n^{(2)'}\left(\rho\sqrt{k^2-w^2}\right)jwe^{jwz}dw,$$

$$= -\frac{1}{2\pi\rho}\sum_{n=-\infty}^{\infty} jne^{jn\phi}\int_{-\infty}^{\infty} g_n(w)\,H_n^{(2)}\left(\rho\sqrt{k^2-w^2}\right)e^{jwz}dw$$

$$+ \frac{1}{2\pi j\omega\varepsilon}\sum_{n=-\infty}^{\infty} je^{jn\phi}\int_{-\infty}^{\infty} f_n(w)\,\sqrt{k^2-w^2}\,H_n^{(2)'}\left(\rho\sqrt{k^2-w^2}\right)w\,e^{jwz}dw,$$

Finally:

$$E\rho(\rho,\phi,z) = \frac{1}{2\pi}\left[\sum_{n=-\infty}^{\infty} -\frac{jn}{\rho} e^{jn\phi} \int_{-\infty}^{\infty} g_n(w) H_n^{(2)}\left(\rho\sqrt{k^2-w^2}\right) e^{jwz} dw\right.$$

$$\left. + \sum_{n=-\infty}^{\infty} \frac{1}{\omega\varepsilon} e^{jn\phi} \int_{-\infty}^{\infty} f_n(w) \sqrt{k^2-w^2}\, H_n^{(2)'}\left(\rho\sqrt{k^2-w^2}\right) w\, e^{jwz} dw\right] . \qquad (10\text{-}10)$$

A similar method is applied to find the near-field expression for H_z. The complete expression is:

$$H_z(\rho,\phi,z) = -\frac{VL}{4\pi^2 a} \sum_{n=-\infty}^{\infty} e^{jn\phi} \left[\frac{\mathrm{Sin}\left(\frac{n\alpha}{2}\right)}{\left(\frac{n\alpha}{2}\right)}\right] \int_{-\infty}^{\infty} \frac{\left[\frac{\mathrm{Sin}\left(\frac{wL}{2}\right)}{\left(\frac{wL}{2}\right)}\right] H_n^{(2)}\left(\rho\sqrt{k^2-w^2}\right)}{\sqrt{k^2-w^2}\, H_n^{(2)'}\left(a\sqrt{k^2-w^2}\right)}$$

$$\left(j\omega\varepsilon + \frac{w^2}{j\omega\mu}\right) e^{jwz} dw . \qquad (10\text{-}11)$$

Applying the boundary condition for $\rho=a$,

$$f_n(w) = \frac{j\omega\epsilon\, E_z(n,w)}{(k^2-w^2)H_n^{(2)}\left(a\sqrt{k^2-w^2}\right)}$$

$$g_n(w) = \frac{1}{\sqrt{k^2-w^2}\, H_n^{(2)'}\left(a\sqrt{k^2-w^2}\right)}\left[E_\phi(n,w) + \frac{nw}{a\sqrt{k^2-w^2}} E_z(n,w)\right]$$

But due to the fact that the aperture excitation is only in the ϕ-direction, the E_z component is zero. Then $f_n(w) = 0$ and $g_n(w)$ becomes

$$g_n(w) = \frac{\overline{E}_\phi(n,w)}{\sqrt{k^2-w^2}\, H_n^{(2)'}\left(a\sqrt{k^2-w^2}\right)}, \qquad (10\text{-}12)$$

which completes the solution.